



POLITECNICO DI MILANO

Department Of Mechanical Engineering
Doctoral Programme In Mechanical Engineering

MECHANICAL BEHAVIOUR OF HIGH TOUGHNESS STEELS IN EXTREME ENVIRONMENTS: INFLUENCE OF HYDROGEN AND LOW TEMPERATURE

Doctoral Dissertation of:
Augusto SCIUCCATI
Mat. 738591

Supervisor:
Prof. Laura VERGANI

Tutor:
Prof. Mario GUAGLIANO

The Chair of the Doctoral Program:
Prof. Giampiero MASTINU

Year 2011 – Cycle XXIV

Contents

INTRODUCTION.....	2
1 HYDROGEN EMBRITTLEMENT OF PIPELINE STEELS.....	5
1.1 General aspects of oil extraction.....	5
1.2 Corrosion in sour environments.....	6
1.3 Typical mechanical failures in sour environments.....	7
1.3.1 Sulphide Stress Cracking (SSC).....	8
1.3.2 Stepwise Cracking (SWC).....	9
1.3.3 Stress Oriented Hydrogen Induced Cracking (SOHIC).....	11
1.4 Hydrogen embrittlement, a possible definition.....	13
1.5 Hydrogen embrittlement effects on mechanical properties.....	14
1.5.1 Effect of hydrogen on ductile-brittle transition temperature DBTT.....	16
1.5.2 Hydrogen effect on fracture toughness and yielding.....	16
1.5.3 Hydrogen effect on fatigue crack propagation.....	17
2 MICROMECHANICS OF HYDROGEN EMBRITTLEMENT.....	19
2.1 Diffusion and trapping of hydrogen in iron lattice.....	19
2.1.1 Simplified model for hydrogen diffusion in steel.....	20
2.1.2 Hydrogen trapping in steels.....	22
2.1.3 Crack tip enriching due to hydrostatic stresses and plastic strain.....	24
2.1.4 Modified hydrogen diffusion model.....	25
2.2 Micromechanical theories of HE.....	25
2.2.1 HEDE, Hydrogen Enhanced DEcohesion.....	25
2.2.2 Hydrogen Affected Localized Plasticity, HELP and AIDE.....	27
3 EXPERIMENTAL PROCEDURES AND RESULTS.....	30
3.1 Materials characterization.....	31
3.1.1 SA-182 F22 steel.....	32
3.1.2 API 5L X65 steel.....	35
3.2 Electrochemical hydrogen charging.....	38
3.3 Cooling and transportation technique.....	40
3.3.1 Environmental chamber.....	40
3.3.2 Ethanol-liquid nitrogen conditioning bath.....	41

3.4	Charpy impact test	42
3.4.1	Charpy impact test results: F22 steel	43
3.4.2	Charpy impact test results: X65 steel	44
3.4.3	Remarks on results	45
3.5	Toughness test	46
3.5.1	Fracture toughness test results	51
3.6	Fatigue crack growth test	57
3.6.1	Fatigue test results: F22 steel	58
3.6.2	Fatigue test results: X65 steel	66
3.6.3	Remarks on results	75
4	FATIGUE CRACK GROWTH PREDICTING MODEL	76
4.1	Theory of the model	76
4.1.1	Frequency and temperature dependence	77
4.2	Analytical procedure	78
4.3	Results	81
4.3.1	Model for F22	81
4.3.2	Model for X65.....	82
4.4	Application of the model to a real crack-like pipelines defect	84
4.4.1	Application of the model to a real case (F22 pipeline).....	84
4.4.2	Application of the model to a real case (X65 pipeline)	93
4.5	Remarks on models and its application	99
5	FRACTOGRAPHIC ANALYSIS	100
5.1	Charpy impact test (fractographic analysis)	100
5.1.1	Macro and micrographic examination: F22 steel	100
5.1.2	Macro and micrographic examination: X65 steel.....	103
5.2	Toughness test (fractographic analysis)	106
5.2.1	Macro and micrographic examination: F22 steel	106
5.2.2	Macro and micrographic examination: X65 steel.....	109
5.3	Fatigue crack growth test (fractographic analysis)	110
5.3.1	Macro and micrographic examination: F22 steel	110
5.3.2	Macro and micrographic examination: X65 steel.....	115
5.4	Considerations on fracture surfaces and predicting model	120
	CONCLUSIONS	123

Ringraziamenti

Grazie alla mia famiglia che ancora una volta è riuscita a farmi vivere serenamente questi anni. A mia madre che mi ha dato tanta fiducia e mi ha fatto compagnia, a mio padre che ha dato tanta importanza alla nostra famiglia e a mio fratellino con cui ho trascorso tanto tempo piacevole.

Grazie Leli che mi sei stata ancora vicina.

Grazie alla Prof. che mi ha insegnato molte cose, mi ha assecondato e sostenuto nelle mie scelte lasciandomi libertà mentale che mi ha fatto coltivare la mia creatività. Grazie per avermi fatto intraprendere un cammino così importante e unico che sarà il mio vanto e mi accompagnerà per il resto della mia vita.

Ringrazio tanto il Prof. Sangirardi senza il quale non avrei intrapreso tale strada; per aver creduto in me dandomi la possibilità di insegnare in un ambiente così virtuoso. Per avermi insegnato tante cose. Peccato non aver registrato ogni discorso per non perdere parole importanti.

Un ringraziamento particolare all'Ing. Re. Grazie per i preziosi consigli, per avermi dedicato tanto tempo e spiegato tante cose; per essere stato così preciso. Peccato non aver passato più tempo insieme. Per me resterà sempre tra i più bravi Professori avuti.

A Chiara che ho sempre ritenuto un modello da seguire per lavorare bene in università. È stato bello fare ricerca insieme e un peccato non aver continuato.

A Edo e alla pazienza che ha avuto per spiegarmi la cinematica “quella difficile e contorta”.

A Elisa che ha allietato le giornate con vivaci sorrisi.

Ai Prof. Bolzoni, Lazzari e Fumagalli del dipartimento di Chimica. Grazie per aver condiviso con me le vostre idee. È stato bello e un privilegio lavorare con voi.

Grazie al Prof. Guagliano, per i suoi consigli fin dal tempo della tesi di Laurea Magistrale.

A Mik che mi ha insegnato i controlli non distruttivi e con cui ho passato divertenti e interessanti ore in laboratorio.

A Licia per avermi sopportato anche quando dimenticavo le procedure amministrative.

A Davide, Gabri, Ramin, Sara, Ermes, Andrea, Mauro, Stefano, Luca, Silvio, Flavia, Giorgio, Max, Claudio, Daniele, Lorenzo e tutti i ragazzi del dipartimento per avermi dato il loro sostegno e avermi tenuto compagnia in questi anni.

Ai Prof. Casolo, Salerno e tutti i Professori del Dipartimento che mi hanno sempre ascoltato quando chiedevo loro consigli.

A Luca, Ale, Piero, Gigi, Luciano, Cacciatore, Beppe, Marco, Mauro, il Motta, Richi, Sergio, Barbara e tutti i tecnici che mi hanno aiutato durante le prove e hanno sopportato le strane richieste dandomi fiducia.

Un sincero ringraziamento alla Dottoressa Fassina e a Eni per aver consentito la ricerca che ha permesso di portare avanti i miei studi e di svolgere questa tesi.

Grazie a tutti per essere stati in questi anni la mia famiglia.

Abstract

In presence of H₂S and CO₂, metallic materials, such as carbon and low alloy steels often used in pipelines, may be subjected to hydrogen damage and embrittlement. The most recent Oil and Gas plants often work in extreme conditions (sour condition and very low temperature).

In this work hydrogen and low temperature effects, on mechanical behaviour of two pipeline steels, X65 microalloyed and F22 low alloy steels, are examined. In particular, it has been investigated how mechanical properties of these two steels depend and are affected by a combined effect induced by hydrogen and low temperature presence.

A large number of mechanical tests have been performed in laboratory simulating real conditions in which these steels work. The specimens were cut from pipes and a part of them was hydrogen charged by a new electrochemical method.

This new non-hazardous charging technique, was developed at the Chemistry, Material and Chemical Engineering Department CMIC “Giulio Natta” of the Politecnico di Milano, in order to introduce, in the material lattice, atomic hydrogen. Diffusible hydrogen content in specimens at about 180°C is in the range 0.6 to 2ppm.

Impact, toughness and fatigue crack propagation tests were carried out on charged and uncharged specimens, by varying the test temperature and, for fatigue crack growth tests, also the load frequency. The experimental results show evident effects due to the hydrogen presence especially in slow load tests.

The hydrogen diffusion rate in the steels structure seems to be the most important parameter in order to explain the temperature influence on the embrittlement process.

Fracture surface examinations provide interesting details to study the phenomenon and confirms the mechanical testing results.

A superposition model, able to predict the crack growth rate versus test parameters such as: temperature, frequency, presence of hydrogen and ΔK has been developed. By means of few tests, performed by fixing temperature and frequency, it is possible to estimate the material behaviour for different test conditions. The model is used for the evaluation of critical situations in different conditions.

Keywords: Hydrogen embrittlement, High toughness steels, Fracture mechanics, Frequency, Low temperature, Superposition model, Fractography, Intergranular fracture, Cellular fracture.

INTRODUCTION

Carbon steel and low alloy steel are commonly used in Oil&Gas industry when general corrosion, due to the presence of H_2S and CO_2 , is considered acceptable to stand the design life. However, when sour condition occurs, the onset of Sulphide Stress Cracking (SSC) in the presence of H_2S on susceptible materials must be investigated [1]. Once metallic materials are exposed to these conditions, in fact, hydrogen embrittlement (HE) is likely to take place, causing unexpected failures and considerable maintenance problems. Hydrogen embrittlement mainly involves, on material behaviour, loss in mechanical ductility, toughness reduction, degradation of fatigue properties and changes in the metallic bonding [2]. Furthermore, when very low temperatures, even below $T=-30^\circ C$, are also present, as in most recent Oil&Gas plants, synergistic effects may occur, from the combination of sour conditions and low temperatures, on the mechanical behaviour of the used materials.

This work is a part of an extensive research project carried out at Politecnico di Milano, sponsored by Eni S.p.A., that aims to investigate the mechanical behaviour of materials used in the above described conditions, in particular in an offshore Oil Field located in Kazakhstan, where low temperatures and sour environments are present.

Extraction and refining oil plants built in Kazakhstan to exploit oil reservoirs, have to deal with extreme environmental conditions: temperature can vary from $T=-30^\circ C$ in winter to $T=30^\circ C$ in summer. Besides, the environment in which the structures and piping must work is sour, that is an aqueous environment with remarkable amounts of H_2S , CO_2 , chlorates, haloids and organic sulphur compounds. Around 40% of worldwide petroleum and gas reservoirs contain such high amounts of dangerous compounds that constrains on design and material choices. Usually, thanks to their compatibility with the transported fluid and their relatively low cost, materials suitable in these conditions are carbon steels.

In order to investigate the change in mechanical behaviour, several tests were carried out on hydrogen charged and uncharged specimens. Some problems and challenges were encountered during tests design; firstly it was difficult to effectively charge specimens with hydrogen. In this regard, a non-hazardous electrochemical charging method has been set up at the Chemistry, Material and Chemical Engineering Department CMIC "Giulio Natta" of the Politecnico di Milano in order to hydrogen charge the specimens. The mechanical characterization of the two steels is carried out through tensile, impact, toughness and fatigue crack growth tests, all of them designed and carried out in accordance with international regulations ASTM and ISO.

Tests are carried out between a temperature range of $T=-128^\circ C$ and $T=23^\circ C$ both for hydrogen charged and uncharged specimens; in fatigue crack growth tests, also load frequency has been varied in order to investigate the effects on the materials.

Tests and simulation of real operative conditions represent an innovative approach in hydrogen embrittlement studies because, at the state of art, there are no similar testing.

Numerical models, implemented through finite element software, have been developed with the purpose to support and optimize specimens and tests design, to evaluate and predict results and to assess the accuracy of the standards. For toughness tests, stress distribution at the crack front, has been studied in case of flat and side-grooved specimens. The optimal dimensions and the shape of the side-grooves were evaluated by several elastic-plastic numerical analyses, carried out by means of three-dimensional finite element models of the CT specimens. In addition, thermal exchange process has been studied to evaluate cooling and conditioning processes useful to bring specimens at the desired test temperature.

A model, for the prediction of crack growth rate in materials subjected to hydrogen embrittlement, is utilized for the estimation of mechanical behaviour degradations and service life of pipelines under aggressive conditions. The model is based on a superposition of two effects: the mechanical component and that provided by the hydrogen presence.

The model estimates the change of the material properties as a function of experimental parameters such as test temperature and load frequency. In particular, once it is known the material behaviour without hydrogen and, with a test on a charged specimen at fixed temperature and frequency, how hydrogen enhances embrittlement, it is possible to predict the crack growth rate and, therefore, the crack length after a certain number of cycles, for different temperatures and load frequencies.

The thesis is structured of five chapters.

In the first chapter, an overview of Oil&Gas industry processes is provided. Main damages, occurring on pipeline steels in sour environments, are shown, with particular regard to its effect on pipeline steels. Embrittlement due to hydrogen presence is introduced and the influence on the mechanical properties of pipeline steels is analyzed.

In the second chapter hydrogen embrittlement for the investigated steels is discussed. The chapter deals the latest theories and models of hydrogen embrittlement from bibliography (HELP, HEDE, AIDE) and the hydrogen kinetics in steel; this chapter also provides powerful tools for further considerations.

In the third chapter some details of the experimental procedures are discussed. Materials properties, microstructure and chemical composition are exhibited. The results of tensile, Charpy impact, toughness and crack growth tests are presented and analyzed.

In fourth chapter, a prediction model, for the estimation of fatigue crack growth in materials with hydrogen presence, is proposed; the model takes into account load frequency and temperature; the estimated trends propagations are verified with the collected data during crack growth tests. Model results are applied to real cases: a crack-like defect is supposed inside the pipeline and its propagation, due to internal pressure variation, is estimated; in this way, it is possible to know the number of cycles and the service life of a structure with a defect, operating in corrosive environments.

In chapter five, macro and micrographic observations are shown. For every tests, specimen fracture surface is analyzed by stereoscopic or optical microscope and by SEM; assessments and considerations on the fracture features are given.

In the last chapter, conclusions and directions for further developments and improvements are given.

1 Hydrogen Embrittlement of Pipeline Steels

1.1 General aspects of oil extraction

The oil extraction from the ground is a complex operation due to the fact that natural oil reservoirs can be hundreds of meters below the surface, trapped in hard rocky pockets containing very aggressive chemical compounds.

Oil extraction, from underground reservoirs, that takes millions of years to form, is performed by drilling the earth crust for a depth that can vary from few hundred meters until some kilometres. An oil well consists of a hole in the substratum, with a diameter around 15-80 centimetres that gradually decreases while depth increases; in this way it is possible to establish a physical link between the surface and the layers where petroleum is stored. Oil is then extracted through small diameter pipelines which can vary from 7 to 12 centimetres in proximity of lower layers.

What is extracted, is not pure crude oil but a mixture of different compounds [3]:

- liquid hydrocarbons;
- water, where it is possible to find dissolved salts, sulphates and carbonates;
- a solid suspension of rocks;
- a mixture of gasses made mainly of light hydrocarbons, CO₂, H₂S, sulphur organic compounds (Carbonyl sulphide and Dimethyl sulphide) and small amounts of inert gasses.

Appropriate gathering lines, consisting of small and medium-size pipelines, channel the oil into vessels, where the first processing unit is performed, at almost the same pressure and temperature conditions present in the well. Inside the vessel there is a first refining step; crude oil is separated into different parts: water phase goes on the bottom together with the solid phase, petroleum occupies the central part, while gas phase fills the upper part of the vessel.

Subsequently, oil is transported to the refineries or to a stocking terminal through pipelines. At this stage, corrosion effects are less remarkable since crude oil, deprived of the gas phase, is less corrosive. Uninteresting gas and liquid phases can be reinjected into the well or refined and commercialized.

Figure 1.1 shows a typical onshore oil field: gas phase, water phase and oil in the rocks can be noted; as mentioned, the most critical conditions for structures are in the first stage where high pressures, high temperatures and aggressive environments are present. In order to safely extract oil in these conditions, materials standards and regulations for design in sour environment are used [4].

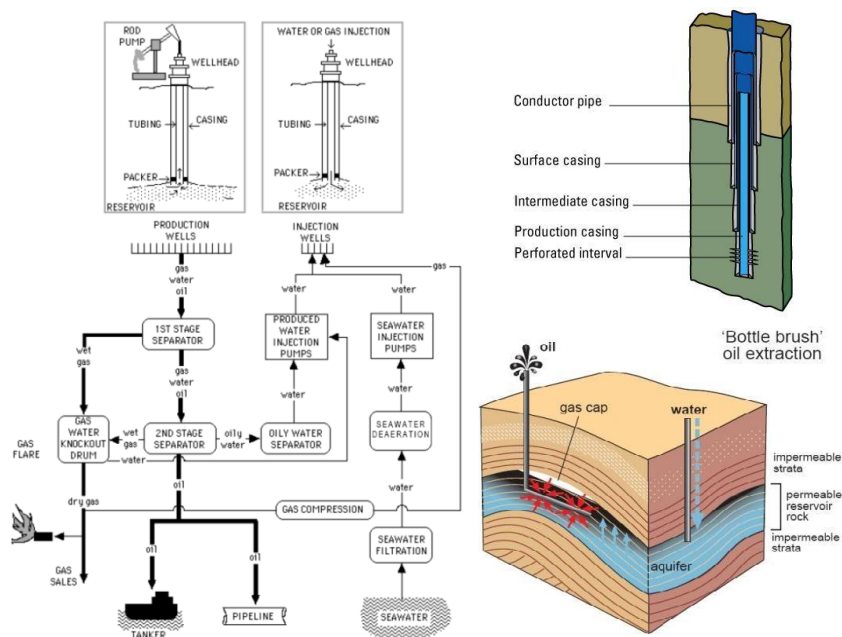


Figure 1.1. Schematic of an oil field and well-tubing.

1.2 Corrosion in sour environments

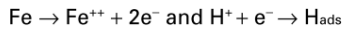
In Oil&Gas industry one of the most challenging issues to deal in designing is due to corrosion and hydrogen embrittlement for metallic materials, which can lead to disastrous consequences for the environment, the economic and also for the personnel health.

In the last decades, energy demand has increased exponentially; this has led to research and exploitation of oil and gas reservoirs in hard regions, increasing the difficulty of the extracting process in terms of location, environments and corrosion conditions. For these reasons, unusual temperatures and environments require the designing of new materials for better performances.

Usually, materials suitable in sour conditions are carbon steels because of their compatibility with the transported fluid and their relatively low cost. Nevertheless, carbon steels, are particularly susceptible in these conditions; if CO_2 is present, general corrosion occurs and if CO_2 and H_2S are present at same time, hydrogen embrittlement takes place. Carbon dioxide increases the acidity of the water phase, causing a general faster corrosion rate. Hydrogen sulphide, instead, modifies the cathodic production reaction of hydrogen and can lead to hydrogen embrittlement of the pipelines since it prevents the hydrogen recombination reaction at the metal surfaces.

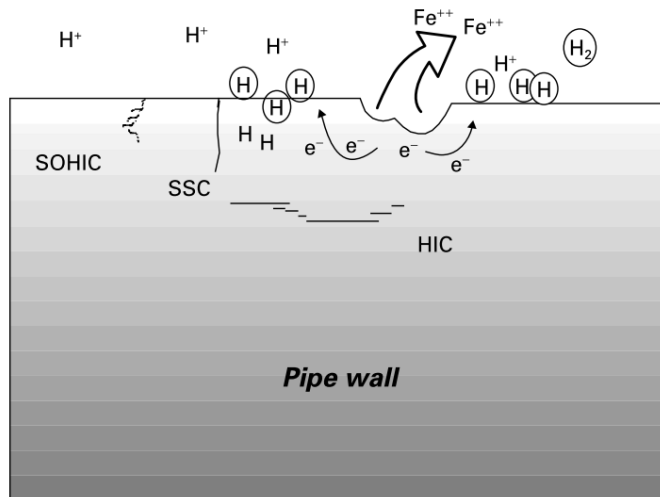
Figure 1.2 shows chemical reaction at pipeline surface in sour environment. Also temperature has a relevant role in corrosion rates; hydrogen embrittlement, as it will be shown later, is deeply affected by temperature and presents a maximum effect at room temperature, while at higher and lower temperature its effect is reduced.

Simplified electrochemical reactions:



The H_{ads} either combines to form H_2 (gas) or becomes absorbed into the steel substrate.

Presence of H_2S increases the absorption of H_{ads} , which may lead to cracking and blistering



Types of corrosion related hydrogen damage

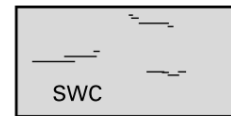
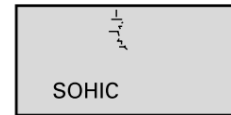
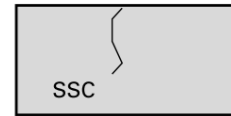


Figure 1.2. Chemical reaction at the steel surface in aggressive environment and possible types of damage [5]

If the pipelines, that are working at very high temperature, are suddenly cooled to a temperature close to $T = -30^\circ\text{C}$, due to a shutdown of the plant or routine maintenance operations, critical conditions can arise, due to the contemporary presence of hydrogen and low temperature, and the changes in mechanical characteristics must be taken into account and investigated. As mentioned before, hydrogen embrittlement can modify the ductile-brittle transition temperature, the toughness and the crack growth resistance in different manner and in relation to how the various effects interact together.

1.3 Typical mechanical failures in sour environments

Carbon steels, that have to operate in sour environment, are susceptible to hydrogen damages since hydrogen production reaction can occur due to the aggressive environment and atomic hydrogen can migrate inside the metal lattice as shown in Figure 1.2. There are many damages, macro and micro phenomena, that hydrogen, dissolved in the metal, can cause and they can mainly divided whether they involve a second phase product (hydrogen compounds and/or molecular hydrogen) or they involve atomic hydrogen as responsible of the failure (hydrogen embrittlement). Figure 1.3 shows typical hydrogen damages that can occur on pipelines. It is characteristic of corrosion in moisture and H_2S environments that atomic hydrogen, owing to an electrochemical reaction between the metals and the H_2S -containing medium, enters the steel at the corroding surface. The presence of hydrogen in the steel may, depending upon the type of steel, the microstructure, inclusion distribution and the stress field (applied and residual), cause different damages and cracking. A brief description of the main types of cracking is given in [6][7].

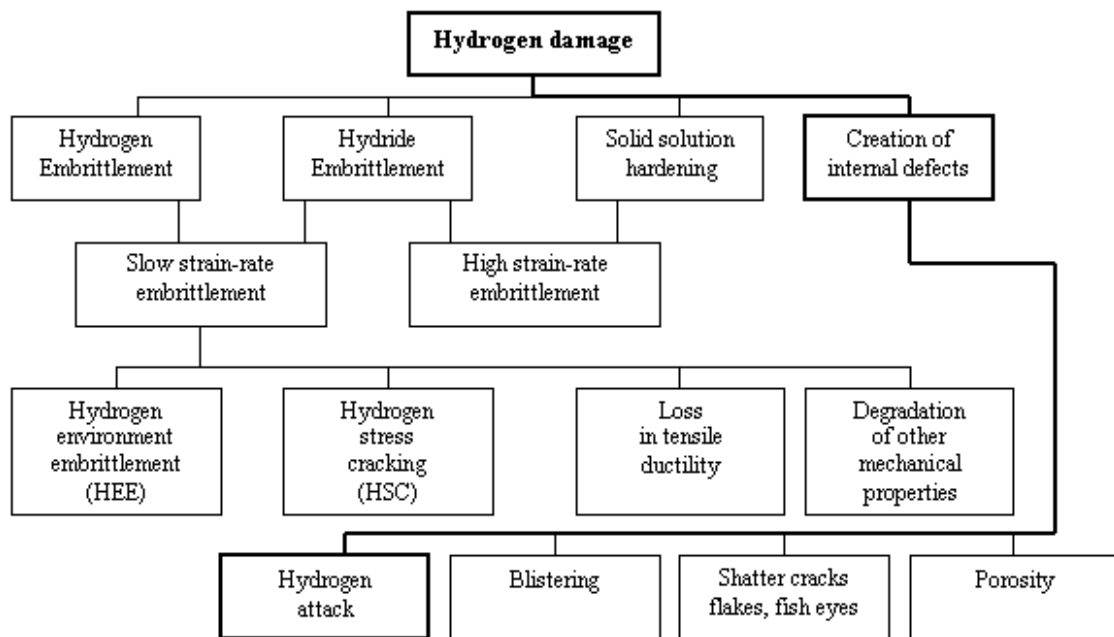


Figure 1.3. Classification of hydrogen damage [7]

1.3.1 Sulphide Stress Cracking (SSC)

Sulphide stress cracking is due to the contemporary action of stress and an amount of atomic hydrogen absorbed into steel during corrosion in sour environments. High strength steels and hard weld zones are particularly susceptible to SSC. The cracking process is very fast and, in few time, can cause catastrophic failures. In particular, three conditions must be present for the occurrence of SSC:

- applied or residual stress;
- material susceptibility;
- embrittling agent, in this case hydrogen sulphide.

SSC is enhanced by the presence of hard microstructures (martensite and bainite). These microstructures may be present in high strength low alloy steels (HSLA) or may come from incorrect heat treatments. Control of hardness is necessary in order to prevent SSC in sour environments. For a given strength level, tempered martensitic steels have better sulphide stress cracking resistance than normalized-and-tempered steels, which in turn are more resistant than normalized steels. Untempered martensite demonstrates poor resistance to sulphide stress cracking. It is generally agreed that a uniform microstructure of fully tempered martensite is desirable for sulphide stress cracking resistance. The presence of hydrogen sulphide in the environment promotes hydrogen absorption into steel. SSC effect increases with increasing hydrogen sulphide concentration or partial pressure and decreases with increasing pH.

The ability of the environment to cause sulphide stress cracking decreases conspicuously above pH 8 and below a partial pressure of hydrogen sulphide of about $p=100\text{Pa}$. The cracking tendency is most pronounced at ambient temperature and decreases with increasing temperature [8]. Typical fracture appearance due to SSC is reported in Figure 1.4.

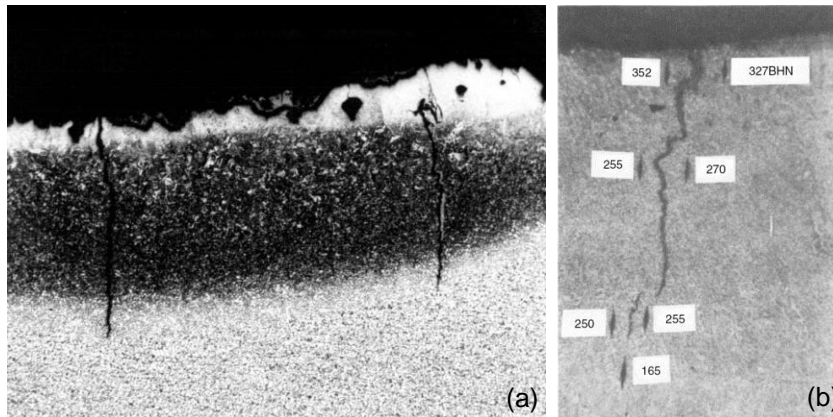


Figure 1.4. SSC in (a) hard weld in ASTM A516-70 plate steel [9] and (b) hard heat-affected zone next to weld in A516-70 pressure vessel steel [10]

Unlike stress corrosion cracking (SCC), that is an anodic process, SSC is considered to be a cathodic process. It is important a good evaluation of the failure behaviour, in order to don't enhance one or the other failure process. In fact, if SCC effects are reduced by applying cathodic protection, more hydrogen is introduced in the lattice, increasing SSC damages.

1.3.2 Stepwise Cracking (SWC)

The name “stepwise cracking” is given to surface blistering and cracking parallel to the rolling plane of the steel plate which may arise without any externally applied or residual stress. The terms, used to define such cracking, include:

- blistering;
- internal cracking;
- Stepwise Cracking (SWC);
- Hydrogen-Induced Cracking (HIC);
- Hydrogen Pressure Induced Cracking (HPIC).

Such cracks occur when atomic hydrogen diffuses in the metal and then recombines as hydrogen molecules at trap sites in the steel matrix. Favourable trap sites are typically found in rolled products along elongated inclusions or segregated bands of microstructure. The molecular hydrogen is trapped within the metal at interfaces between the inclusions and the matrix and in microscopic voids.

As more hydrogen enters the voids, the pressure rises, deforming the surrounding steel so that blisters may become visible at the surface. The steel around the crack becomes highly strained and this can cause linking of adjacent cracks to form SWC. The arrays of cracks have a characteristic stepped appearance. While individual small blisters or hydrogen induced cracks do not affect the load bearing capacity of equipment they are an indication of a cracking problem which may continue to develop unless the corrosion is stopped. At the stage when cracks link up to form SWC damage, these may seriously affect the integrity of equipment. Control of the microstructure and particularly the cleanliness of steels, reduce the availability of crack initiation sites and is therefore critical to the control of SWC [6]. Figure 1.5 shows typical blisters.

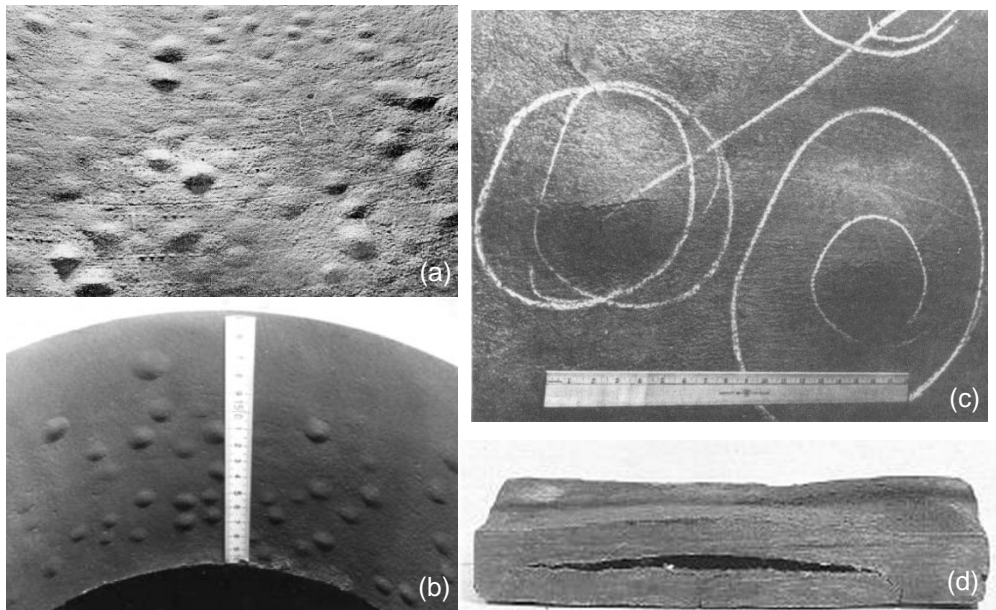


Figure 1.5. Typical aspect of hydrogen blisters on (a) a vessel, (b) on C-0.5Mo nozzle flange used in Platformer unit [11], (c) on a carbon steel shell of an absorber/stripper tower in the vapour recovery section of a catalytic cracking unit [10] and (d) in wall plate of a CO₂ scrubbing tower [12]

High pressures may be built up at such locations due to continued absorption of hydrogen leading to blister formation, growth and eventual bursting of the blister. Such hydrogen induced blister cracks have been observed in steels, aluminium alloys, titanium alloys and nuclear structural materials [13]. The principal method used in order to prevent these damaging phenomena is to select a high quality clean material and, in some cases, to reduce stresses by heat treatment [14].

Flakes and shatter cracks are internal defects seen in large forgings. Hydrogen picked up during melting and casting, segregates at internal voids and discontinuities and produces these defects during forging. Fish-eyes are bright patches resembling eyes of fish, generally present on weldments fracture surfaces (see Figure 1.6) [13].

Hydrogen enters the metal during welding process and produces this defect during operative phase, when stresses are present.

Steel containment vessels, exposed to extremely high hydrogen pressures, develop small crevices or micro perforations through which can cause leakage [6][7].

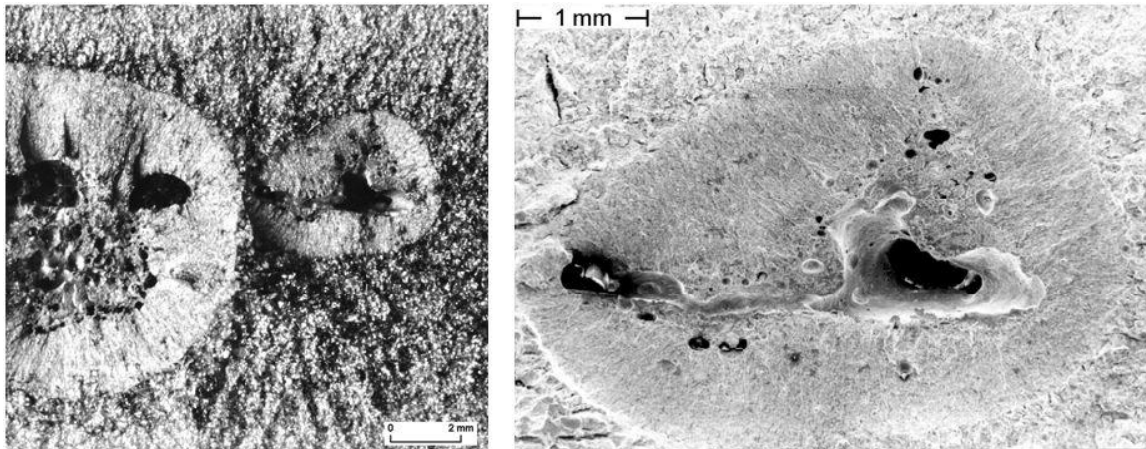


Figure 1.6. Macro fisheyes and a magnification showing a slang hole as a fisheye centre in a high strength steel

1.3.3 Stress Oriented Hydrogen Induced Cracking (SOHIC)

SOHIC is related to both SSC and SWC. In SOHIC staggered small cracks are formed approximately perpendicular to the principal stresses (applied or residual) resulting in a “ladder-like” crack array [5]. The mode of cracking can be classified as SSC caused by a combination of external stress and the local straining around hydrogen induced cracks. SOHIC has been observed in parent material of longitudinally welded pipe. Soft Zone Cracking is the name given to a similar phenomenon when it occurs specifically in softened heat affected zones of welds in rolled plate steels. The susceptibility of such welded regions to this type of crack types, is provided by a combination of microstructural effects, caused by the temperature cycling during welding and local softening in the intercritical temperature heat affected zone. This results in strains, within a narrow zone, which may approach, or even exceed, the yield strength. In the past, SOHIC has caused service failures of pipelines, but there are no reported service failures due to SOHIC in modern sour service steels [6]. In Figure 1.7 an example of HIC and SOHIC are shown.

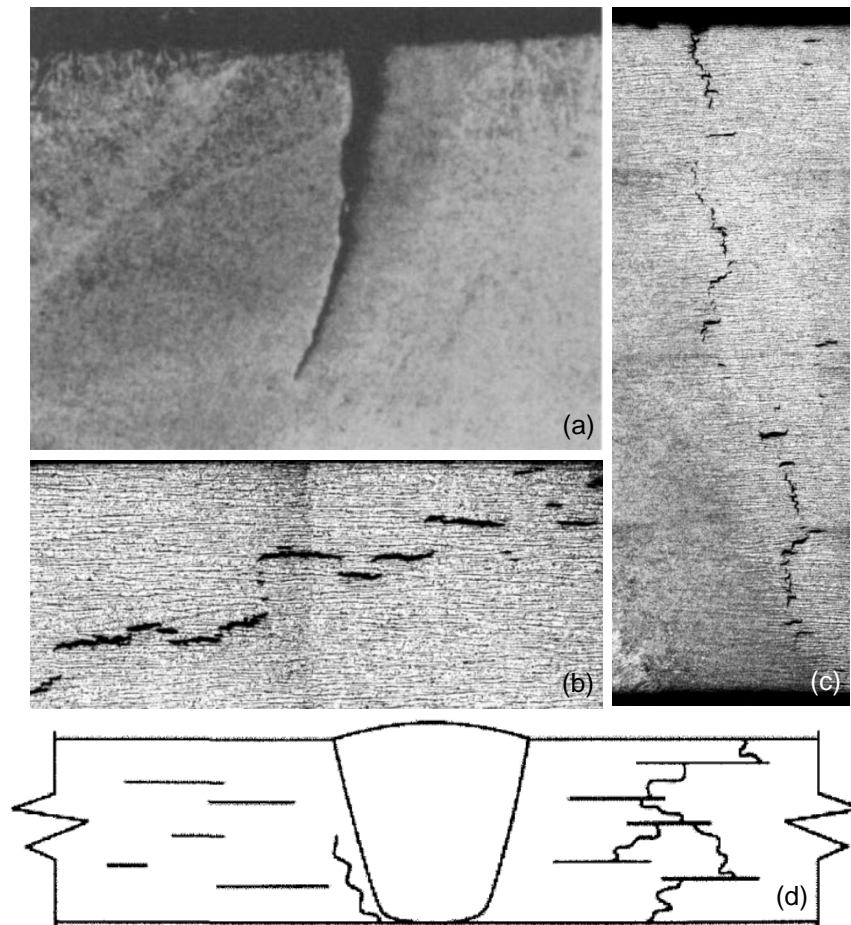


Figure 1.7. (a) SSC in an hardened heat-affected zone on a weld (API, 1990) [15], (b) HIC in an ASTM A516-70 plate steel (note crack parallel to plate surface and ferrite/pearlite bands) [9], (c) SOHIC in the base metal adjacent to a weld heat-affected zone on an A516-70 plate steel [9] and (d) a general overview of the damage phenomena [16]

In Figure 1.8 a pressure vessel, failed during its hydraulic test, is shown. The heat treating was not completed, so the presence of hydrogen, due to an aggressive environment cause a catastrophic failure.

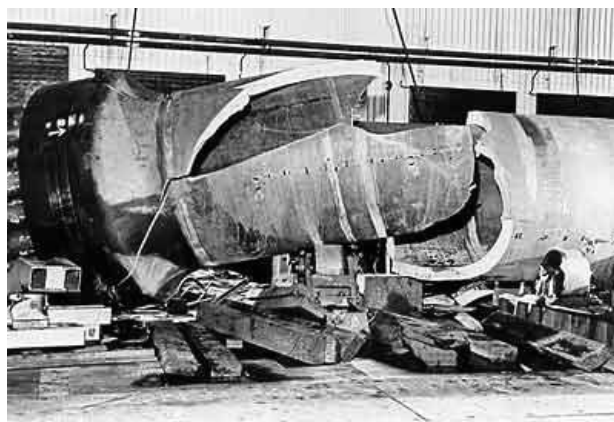


Figure 1.8. Failure of a pressure vessel, during a pressure test, due to an inadequate PWHT process

1.4 Hydrogen embrittlement, a possible definition

A definition of hydrogen embrittlement is complex to be given, since it involves many branches of science; nevertheless, it can be understood as a general fracture-mechanical worsening of steel properties such as ductility, toughness, impact energy and crack growth resistance due to hydrogen dissolved in the lattice and segregated at crack tip, reducing the cohesion between iron atoms (Hydrogen-Enhanced DEcohesion, HEDE), increasing local plasticity (Hydrogen Enhanced Local Plasticity, HELP) and enhancing dislocation emission at crack surface (Adsorption-Induced Dislocation Emission, AIDE). According to this definition, the problem needs to be tackled in a methodical approach to divide and analyse all the aspects as it follows:

- a solid mechanics analysis that models the behaviour of the material at high stresses and strain also in the plastic regime;
- a fracture mechanics analysis that allows to model the stress distribution and plastic strains at crack tip;
- a physical-chemical and kinetics analysis that takes into account reaction at surface and hydrogen penetration in the lattice;
- a diffusion analysis that couples the diffusion of hydrogen, trapping and diffusion driven by stresses and plastic flow;
- a micromechanical model that takes into account all previous problems and consider hydrogen concentration, critical stresses and strains and materials properties in order to give a quantified degradation in terms of mechanical properties [2].

The mechanism is well depicted in Figure 1.9, where all the mechanisms taking part (diffusion, plasticity, stress distribution, trapping) are shown.

It is important to point out that, in this research, internal hydrogen assisted cracking (IHAC) conditions are simulated, in fact, specimens were precharged, so that hydrogen is distributed uniformly in the lattice, but hydrogen is not introduced during mechanical tests. For this reason, and since this work is concentrated on mechanical aspects, reactions on the surface and the diffusion kinetics through surface will not be discussed.

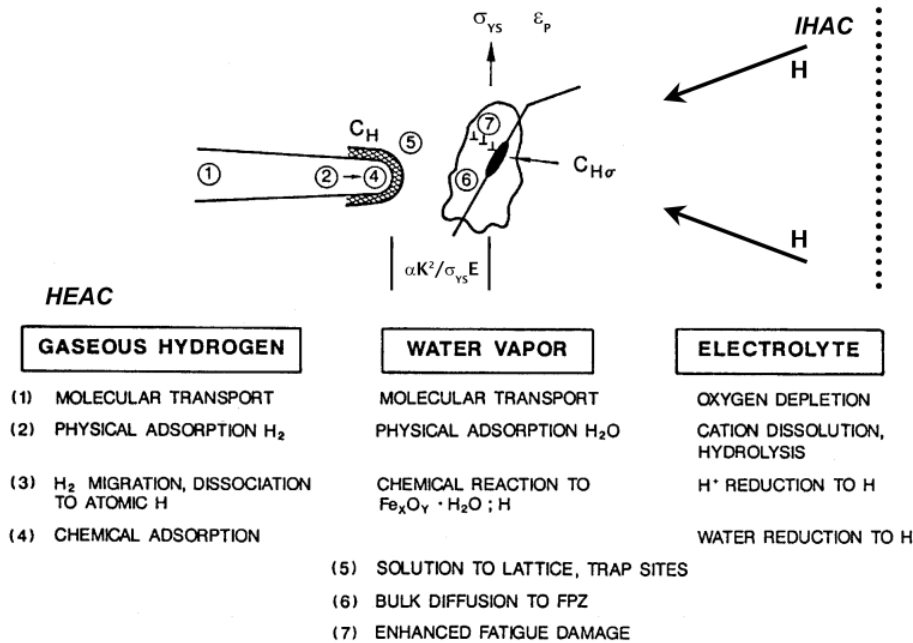


Figure 1.9. The sequence of elemental processes that supply damaging H to the crack tip fracture process zone during either HEAC for gaseous hydrogen, water vapour or an electrolyte, or IHAC for a H precharged microstructure. The dotted line indicates the outer boundary of the plastic zone.

Crack tip tensile stresses are maximized at some distance ahead of the tip, proportional to $K^2/\sigma_{ys}E$ [2]. Hydrogen attracted at the crack tip, by hydrostatic stress and plastic strains, leads to a properties worsening and increased micro-ductility.

1.5 Hydrogen embrittlement effects on mechanical properties

In order to get a clear understanding of hydrogen embrittlement effects on materials, it is useful to start with understanding how it affects mechanical properties of materials that can be measured with classical tests such as, rising load tensile tests on specimens. The first important aspect, that was observed for hydrogen charged high strength steels, was “hydrogen-induced delayed failure” [17], since fracture was observed to occur after a certain time and in circumstances where tensile or bending tests on uncharged specimens showed no evidence of brittleness, as shown in Figure 1.10 and Figure 1.11. It can be seen that crack starts to growth after an incubation time; this feature is peculiar of HE and will be related, later, to diffusion of hydrogen driven by hydrostatic stresses and large strains ahead of the crack tip. These first accomplishments from Troiano [17], even though they lead to some misinterpretations of the micro mechanisms governing it, shown that hydrogen embrittles the material and that it requires an incubation time before it occurs, due to hydrogen diffusion and enrichment at crack tip.

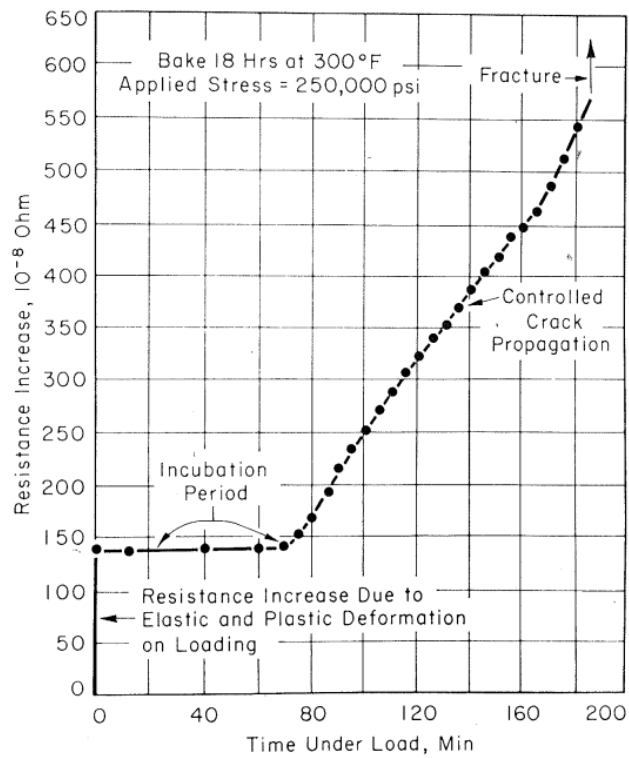


Figure 1.10. Typical resistance-time curve for sharply notched specimen (resistance is proportional to crack extension)

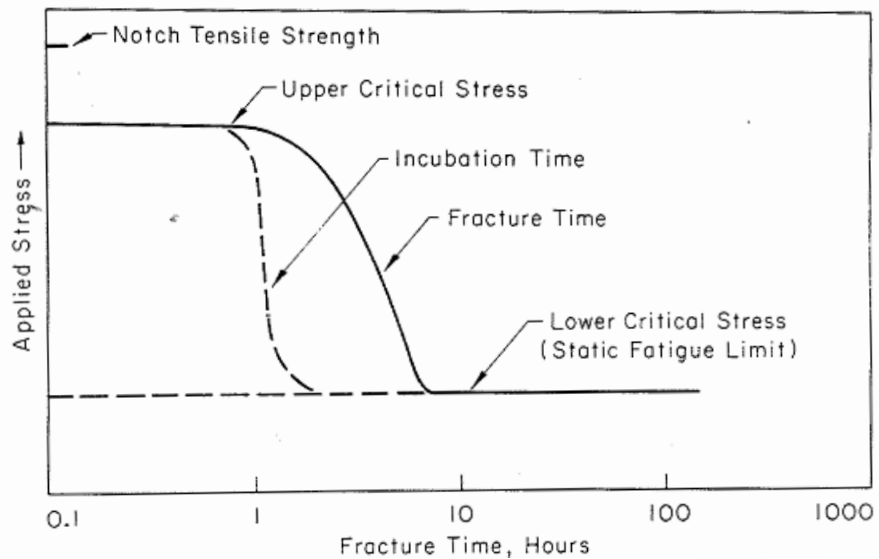


Figure 1.11. Schematic representation of delayed failure characteristics of a hydrogenated high strength steel

1.5.1 Effect of hydrogen on ductile-brittle transition temperature DBTT

Hydrogen is supposed to increase DBTT, nevertheless the amount is strictly related to microstructure and hydrogen content. This part will be discussed and commented largely in paragraph 3.4, since Charpy impact tests have been performed on CV specimens in a wide temperature range for charged and uncharged specimens.

1.5.2 Hydrogen effect on fracture toughness and yielding

There have been many researches and tests to assess hydrogen effect on toughness of steels, especially in pipeline steels. They all show a reduction in toughness but this reduction depends on charging and testing conditions since there are many ways to conduct these tests: hydrogen can be distributed uniformly inside the lattice, it can also be provided by a cathodic reaction at crack surfaces and the amount of hydrogen can vary largely. In Figure 1.12, K_{Ic} vs. yield stress for different pipeline steels at room temperature is shown. It can be seen that the reduction is greater for old steels, while, for new steels, such as X100, there is no variation. In this research [18], CT specimens were charged in an electrolytic solution. The difference in fracture toughness, between charged and uncharged specimens, for the investigated materials is anyway very low also thinking that the entire experimentation is subjected to statistic variability; this can depend by different factors like amount of hydrogen charged and how the specimens were stored before testing.

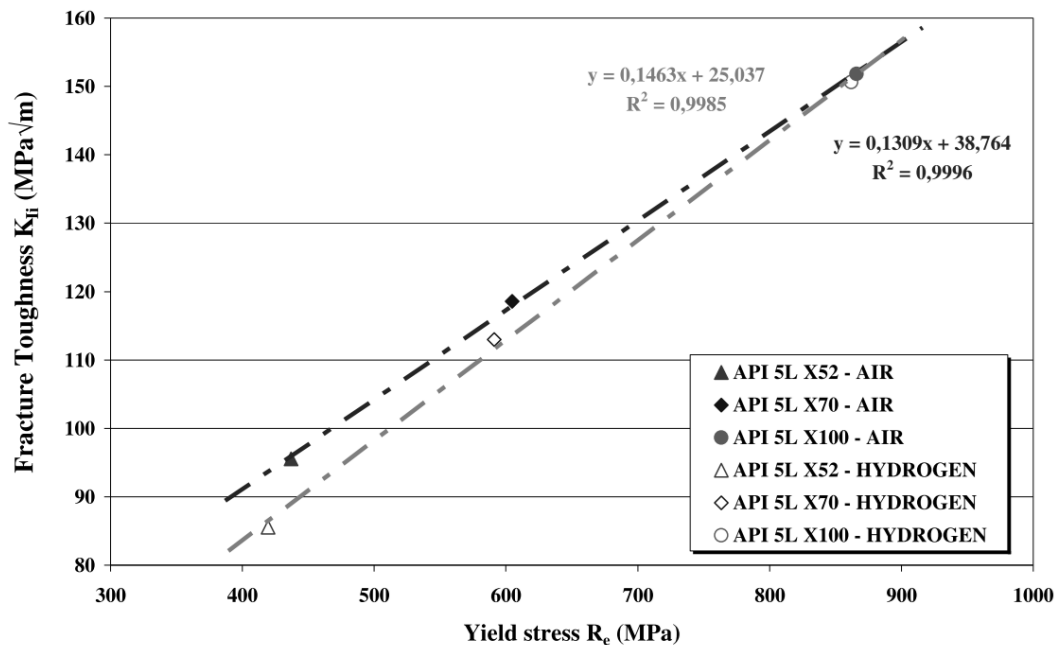


Figure 1.12. Fracture toughness of three steels K_{Ic} vs. yield stress in air and hydrogen environment

Hydrogen also reduces the ductility of the material that can be assessed through stress-strain behaviour.

From many investigations [19], it was observed a drastic reduction on the plastic stress-strain curve strongly dependent on the amount of hydrogen and also on the strain rate (this dependence will be clarified later on). It was shown that hydrogen-charging will enhance the susceptibility of the steel to HIC. The cracks initiate prematurely in the proximity of inclusions, such as aluminium oxides, titanium oxides and ferric carbides. This macro-behaviour will be explained by HELP theory with the hypothesis that hydrogen increases micro-ductility and the macroscopic result is a brittle rupture.

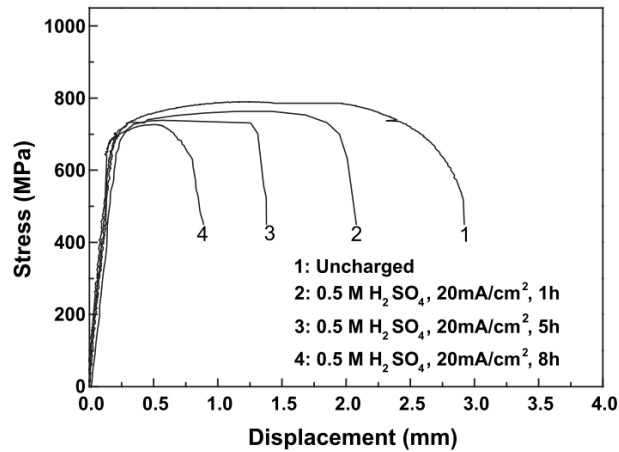


Figure 1.13. Stress-strain curve for X100 under various charging times [19]

1.5.3 Hydrogen effect on fatigue crack propagation

Hydrogen deeply affects the behaviour of steels and metals in general, under variable loads below the critical values (yield stress), since, as already mentioned, hydrogen embrittlement is largely dependent on diffusive phenomena occurring inside the material. In particular, hydrogen drastically increases the crack growth rate up to 40 times and reduces the number of cycles to failure [19][20], as reported in Figure 1.14 and Figure 1.15. Fatigue crack propagation is very sensible to environment and test conditions; variation in test temperature and load frequency, in particular, can severely affect the crack propagation rate also of some order of magnitude as it will be shown in chapter 3. For this reason, particular attention has been focused on “da/dN vs. ΔK ” plots; in this way, Paris relation can be estimated, where it is possible, and predicting models can be used in presence of corrosion.

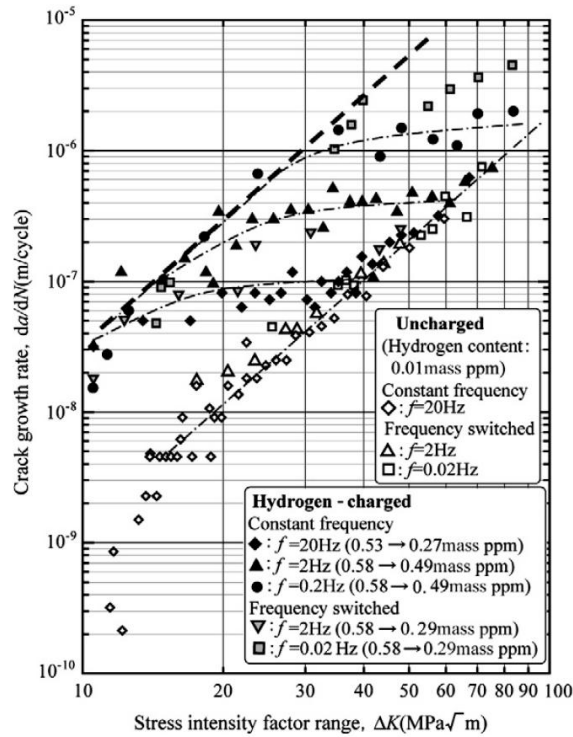


Figure 1.14. Relationship between da/dN and ΔK . Material: SCM435. Hydrogen content indicated by ***→** means that hydrogen content decreased from *** to ** during fatigue test. “Frequency switched” means that the test frequency was switched between $f=2\text{Hz}$ and $f=0.02\text{Hz}$ [20]

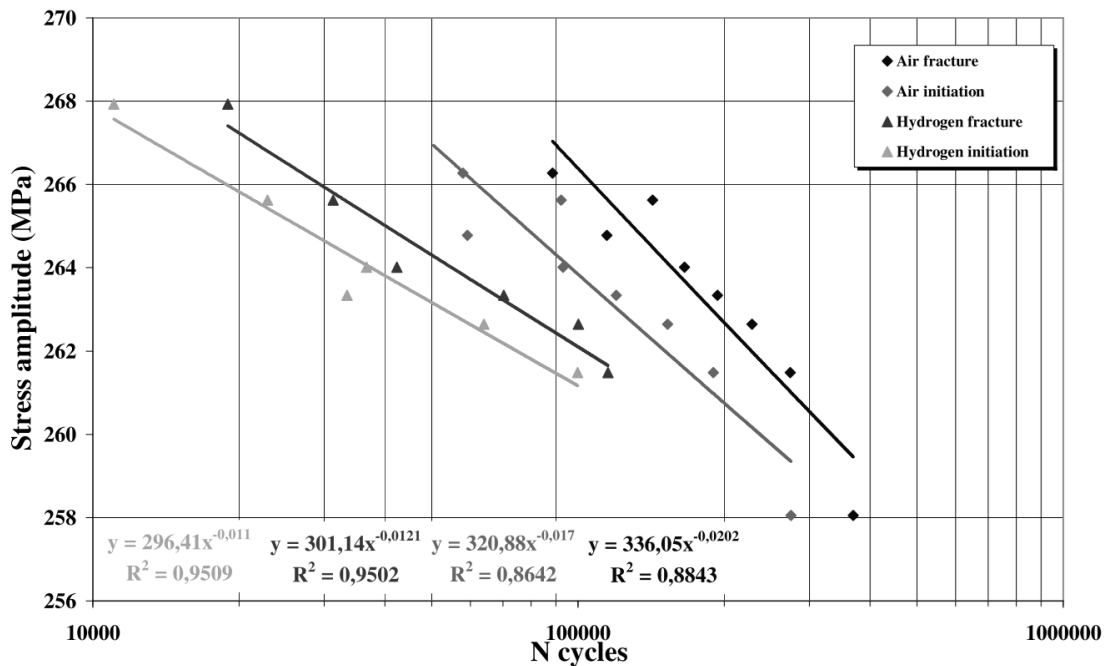


Figure 1.15. Fatigue endurance curves at initiation and at failures of X52 steel with and without hydrogen charging

2 Micromechanics of Hydrogen Embrittlement

According to the definition given in paragraph 1.4, in order to analyse and model hydrogen embrittlement, it is necessary to study all the aspects enumerated in paragraph 1.4. For this reason, first, the main concepts of fracture mechanics and stress distribution at crack tip will be reviewed; then, diffusion kinetics and trapping theory will be shown to justify micromechanical models treated in literature such as HEDE, HELD and AIDE.

2.1 Diffusion and trapping of hydrogen in iron lattice

As shown before, hydrogen embrittlement is strongly dependent on time. This is a clear evidence that hydrogen embrittlement is a phenomenon governed by kinetics and, hence, by its diffusion and enriching at crack tip.

Atomic hydrogen diffuses easily in metals owing to its small atomic radius (53pm) that is similar to the length of interstitial sites in metal lattice; hydrogen diffusivity value in iron is around $10^{-5} \text{cm}^2/\text{s}$. Hydrogen mobility in carbon steel and low-alloy steel is much higher than any other atoms since its small radius. Parameters that deeply affect hydrogen diffusivity are: lattice characteristics, stress state and plastic deformation that implies an increase of the dislocation density [21]. An important remark should be done if considering either FCC or BCC structure. BCC structure, typical of ferrite, can contain (solute) less hydrogen than FCC (typical of austenite); on the other hand, in ferrite, hydrogen diffusion is higher than austenite. In Figure 2.1a, hydrogen diffusivity vs. temperature for different lattice structure is plotted; it can be noticed that, in ferrite, diffusivity varies within a large range. The hydrogen solubility in steel also depends to temperature and pressure, as reported in Figure 2.1b.

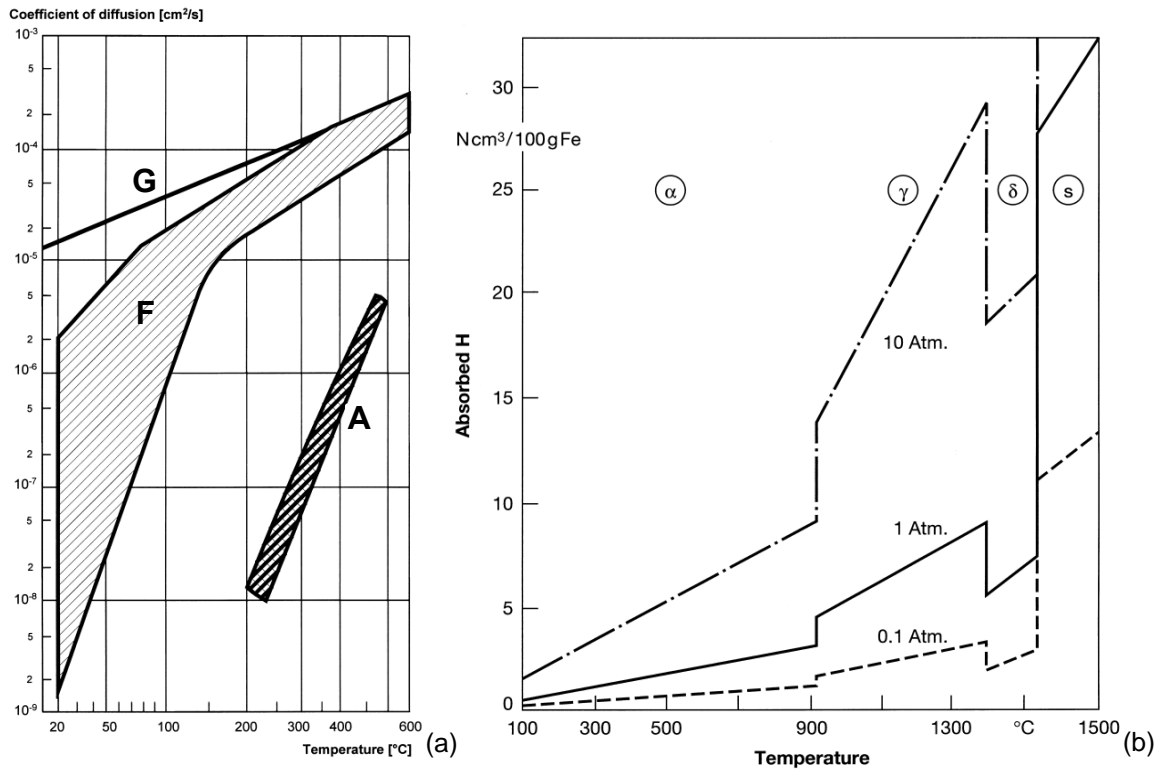


Figure 2.1. (a) Hydrogen diffusivity in ferrite (F) and austenite (A) and (b) solubility of hydrogen in iron as a function of temperature and pressure

Indeed, diffusion is affected by microstructural variables (precipitates and inclusions) and by alloying elements [22]. There are other potential mechanisms for hydrogen diffusion that consider dislocations, shortcuts and interstitial jumps. In the next paragraph a simplified model for hydrogen diffusion will be given only considering diffusion coefficient while, in paragraph 2.1.2, hydrogen trapping is considered.

2.1.1 Simplified model for hydrogen diffusion in steel

Hydrogen diffusion in a metal lattice (considered perfectly homogeneous), can be modeled, in a simplified way, with Fick diffusion laws [23]:

$$J = -D\nabla C \quad 2.1$$

$$\frac{\partial C}{\partial t} = D\nabla^2 C \quad 2.2$$

Where:

- J [mol·cm⁻¹·s⁻¹] is hydrogen flux;
- D [cm²·s⁻¹] is diffusivity;

- C [$\text{mol}\cdot\text{cm}^{-3}$] is H concentration;
- t [s] is time.

First Fick's law is valid only in stationary conditions when the concentration of the diffusing atoms is constant in time. Otherwise, when concentration is time-dependent Fick's second law should be used. Diffusivity D can be expressed as a function of temperature through an Arrhenius-like equation:

$$D = D_0 \cdot \exp\left(-\frac{E_A}{R \cdot T}\right) \quad 2.3$$

Where:

- D_0 [$\text{cm}^2\cdot\text{s}^{-1}$] is the diffusivity at infinitive temperature;
- E_A [$\text{J}\cdot\text{mol}^{-1}$] is the activation energy for diffusion;
- T [K] is the absolute temperature of the diffusion process;
- $R=8,314472$ [$\text{J}\cdot(\text{mol}\cdot\text{K})^{-1}$] is the gas constant.

Diffusivity can vary according to other parameters such as concentration of the diffusing atom; this dependence will not be considered in order to simplify the calculations.

For a semi-infinite specimen, Eq. 2.2 can be solved by giving suitable boundary conditions:

- $C(t=0)=\text{const.}=C_0$, bulk concentration of hydrogen
- $C(x=0)=\text{const.}=C_s$, surface concentration of hydrogen

in order to write the following Equation:

$$\frac{C - C_0}{C_s - C_0} = 1 - \text{erf}\left(\frac{x}{\sqrt{4Dt}}\right) = \text{erfc}\left(\frac{x}{\sqrt{4Dt}}\right) \quad 2.4$$

Where x is the distance from free surface and erf is the error function.

Really, hydrogen diffusivity in steels depends on many factors: composition, microstructure, inclusion content and dimensions, elastic or plastic deformation and temperature. Only at room temperature, in fact, diffusivity assume a wide range, between about 10^{-9} and 10^{-5} cm^2/s (Figure 2.1a).

2.1.2 Hydrogen trapping in steels

Darken and Smith [24] were apparently the first to suggest that the delayed transport of hydrogen in cold worked steels, as determined by measurements of permeation transients, was caused by attractive interaction between lattice-dissolved hydrogen and microstructural imperfection, or traps. These traps are favourable energy sites where hydrogen places itself either in a reversible or irreversible way, accordingly to the binding energy between hydrogen and the trap. Trap binding energy can vary with temperature, but, in general, when one hydrogen atom moves from an interstitial lattice site to a trap, the probability that it has to move to another site lowers drastically. Since trap-H binding energy is much higher than NILS-H binding energy (NILS=normal interstitial lattice site), the energy barrier to overcome it is so high that probability to move out of a trap drops.

The more attractive traps, with a high irreversible grade, are inclusions of manganese sulphide; other possible irreversible trapping sites, ordered with decreasing of irreversibility, are:

- oxides and sulphides inclusions;
- titanium, niobium or vanadium carbide and carbonitride;
- cementite.

The consequences of these traps on apparent diffusion of hydrogen are [25]:

- increased apparent solubility;
- decreased apparent diffusivity;
- apparent shifting from Fick's law;
- increased local hydrogen concentration.

Irreversible traps, mentioned above, once saturated, do not take part to any process of hydrogen enriching owing to their high trapping energy, on the other hand, reversible trapping energies are worth to be considered when hydrogen enriching at crack tip needs to be modeled. Reversible trapping sites are: dislocation cores, grain boundaries, interfaces (inclusions and precipitates), vacancies and cavities.

The most important trapping site is given by dislocation cores, since the number of dislocations varies accordingly with the plastic strain ϵ_p , its number can be very large where stresses are concentrated, such as at crack tip. Many attempts were done in trying to quantify dislocation binding energy. A successful attempt was made by Kumnick and Johnson [26], they calculated trap binding energy for deformed iron and trap density as function of plastic strain. Results of their work are shown in Table 2.1; a binding energy approximately of $60 \text{ kJ}\cdot\text{mol}^{-1}$ was found for deep trapping state.

Table 2.1. Trap parameters of iron determined at different deformation levels and temperatures [26]

% Cold work	Trap density N_T [m^{-3}]	Binding Energy E_b
0 (Annealed)	$8.5 \cdot 10^{20}$	
15	$5.9 \cdot 10^{22}$	↑
30	$5 \cdot 10^{22}$	$14.3 \pm 1.1 \text{ kcal} \cdot \text{mol}^{-1} \text{H}$
40	$7 \cdot 10^{22}$	$(59.9 \pm 4.6 \text{ kJ} \cdot \text{mol}^{-1} \text{H})$
60	$1.5 \cdot 10^{23}$	↓
80	$1.8 \cdot 10^{23}$	

First trapping models were developed separately respectively by McNabb and Foster [27] and Oriani [28]. Oriani's theory appears easier to understand and to apply, even if it considers that equilibrium between trapping sites and lattice sites is reached quickly. This assumption can be good if considering slow tests (low strain rate), otherwise it can lead to inaccuracy and time dependence must be considered.

Hydrogen is assumed to reside either at NILS (normal interstitial lattice site) or reversible sites at microstructural defects, such as: internal interfaces or dislocations generated by plastic deformation. The two populations are always in equilibrium according to his theory, such as:

$$\frac{\theta_T}{1-\theta_T} = \frac{\theta_L}{1-\theta_L} \exp\left(\frac{W_B}{RT}\right) \quad 2.5$$

Where:

- θ_T is the occupancy of trapping sites;
- θ_L is the occupancy of NILS sites;
- W_B is the trap binding energy, calculated by Kumnick and Jonhson (Table 2.1);
- R is the gas constant and T the absolute temperature;

The hydrogen concentration in trapping sites C_T , measured in hydrogen atoms per unit volume, can be written as:

$$C_T = \theta_T \alpha N_T \quad 2.6$$

Where α denotes the number of sites per trap and N_T denotes the trap density in number of traps per unit volume. The hydrogen concentration C_L in NILS, measured in hydrogen atoms per unit volume, can be phrased as:

$$C_L = \theta_L \beta N_L \quad 2.7$$

Where β denotes the number of NILS per solvent atom, N_L denotes the number of solvent atom per unit volume given by $N_L = N_A / V_M$ with N_A equal to Avogadro's number and V_M the molar volume of host lattice.

Oriani suggested to substitute the diffusivity (Eq. 2.3), valid for a trap free lattice with a new effective diffusion coefficient D_{eff} that takes into account trapping such as:

$$D_{eff} = D_L \frac{1}{1 + K \frac{N_T}{N_L}} \quad 2.8$$

Where K is the equilibrium constant that can be expressed as $\exp(W_B / RT)$.

2.1.3 Crack tip enriching due to hydrostatic stresses and plastic strain

As mentioned in the previous paragraph, plastic strain can increase the number of dislocations and traps. $N_T = N_T(\epsilon_P)$ denotes the trap density, in number of traps per unit volume, as a function of the amount of local plastic strain ϵ_P (Table 2.1). Another parameter that can affect hydrogen solubility is hydrostatic stress; it was shown that cubic distortion of metal lattice, by interstitial hydrogen atoms, gives rise to a macroscopic volume change V_H per mole of H; therefore, H atoms interact only with the hydrostatic part of the stress field σ_h , changing the chemical potential by a term $\sigma_h V_H$. In thermodynamic equilibrium, the chemical potential of H has to be the same in all the regions of the sample. Thus an inhomogeneous spatial distribution of hydrostatic stresses (such as at crack tip), leads to a redistribution of H-concentration according to [29]:

$$\begin{aligned} \mu_H(\sigma_h = 0) &= \mu_H^0 + RT \ln c_0 = \mu_H(\sigma_h \neq 0) \\ &= \mu_H^0 + RT \ln c(x) + \sigma_h V_H \end{aligned} \quad 2.9$$

$$\text{or} \quad c(x) = c_0 \exp\left(\frac{\sigma_h(x) V_H}{RT}\right)$$

Where μ_H^0 is the standard value of μ_H and c_0 is the H-concentration at zero hydrostatic stress (*e.g.* far away from hydrostatic stresses). Eq. 2.9 is valid for low concentrations only, *i.e.* for the ideal dilute case [29]. Eq. 2.9 can be rearranged and written as it follows:

$$\frac{\theta_L}{1 - \theta_L} = \frac{\theta_L^0}{1 - \theta_L^0} \exp\left(\frac{J_1 V_H}{3RT}\right) \quad 2.10$$

Where J_1 is the first stress invariant of the stress tensor and is divided by 3 to give the hydrostatic stress and θ_L^0 is the NILS occupancy when no stress is applied.

2.1.4 Modified hydrogen diffusion model

At crack tip, stresses and strain cannot be neglected and they must be taken into account in a time-dependent diffusion model; McNabb and Foster proposed the following equation, derived from a modification of Fick's law, as the governing equation for transient hydrogen diffusion accounting for trapping and hydrostatic drift [27]:

$$\frac{\partial C_L}{\partial t} + N_T \frac{\partial \theta_T}{\partial t} = \nabla \cdot (D_L \nabla C_L) \quad 2.11$$

Working out Eq. 2.11 with Eq. from 2.5 to 2.10, leads to the governing equation for hydrogen diffusion [30]:

$$\frac{D}{D_{\text{eff}}} \frac{dC_L}{dt} + \alpha \theta_T \frac{dN_T}{d\varepsilon_P} \frac{d\varepsilon_P}{dt} - DC_{L,ii} + \left(\frac{DV_H}{3RT} C_L \sigma_{kk,i} \right)_{,i} = 0 \quad 2.12$$

Equation 2.12 shows that in order to calculate the hydrogen distribution within a solid, one should solve a coupled problem of hydrogen diffusion and elastoplasticity. Oriani's model assumes that the trap filling kinetics is very quick. Consequently, the effective diffusion coefficient D_{eff} is less than the normal NISL diffusion coefficient D as long as traps are not saturated or new traps are created by plastic straining [30].

2.2 Micromechanical theories of HE

Before it was shown that stresses distribution and plastic strain can largely modify hydrogen concentration and diffusion and, since at crack tip these conditions occur, recent theories have been introduced to link the high local H concentration to damaging micro-mechanisms that lead to failure. The first theory, called hydrogen enhanced decohesion, introduced by Troiano, was later taken on by other theories involving dislocation models (HELP and AIDE). It is still impossible to assess which is the most correct theory, nevertheless, it was shown that all of them can explain the damage phenomena due to hydrogen embrittlement. In this paragraph all the theories will be shown with relative models. In his review of hydrogen assisted cracking, Gangloff [2] gives a clear overview of the main theories on internal HE that will be reported below; nevertheless, his work is mainly qualitative and, for this reason, quantitative models will be added from literature.

2.2.1 HEDE, Hydrogen Enhanced DEcohesion

The HEDE mechanism was first suggested by Troiano, and developed in detail by Oriani and co-workers. In this model, hydrogen segregates at the crack tip FPZ (fracture process zone) and, there, reduces the cohesive bonding strength between metal atoms. The HEDE gives the concept that hydrogen damage occurs in the FPZ when the local crack tip tensile

stress exceeds the maximum-local atomic cohesion strength, reduced by the presence of hydrogen.

In the HEDE scenario, hydrogen damage sites are located at a distance ahead of the crack tip surface where tensile stresses are maximized. Predictions may derive from knowledge of crack tip stress, hydrogen concentration at damage sites, and its relationship with the interatomic bonding force vs. atom displacement. It is possible to presume that HEDE is the dominant mechanism for IHAC (internal hydrogen assisted cracking) and HEAC (hydrogen environmentally assisted cracking) in high strength alloys that do not form hydrides. HEDE is likely for several reasons. First, large concentrations of hydrogen should accumulate at the crack tip owing to very high crack tip stresses and, in addition, hydrogen is trapped along the crack path [2].

Dislocations promote a local stress concentration around decohesion sites so to weaken the metal bonds. Decoherence can take place in different zones such as: at crack tip, or right ahead, and where dislocations increase stress concentration. Fractographic observations have shown that this mechanism occurs especially with brittle fracture surfaces; typical fracture surfaces caused by HEDE are intergranular and transgranular and are usually smooth, although also plasticization can be observed [1].

Oriani and Josephic [31] have shown that over a wide range of hydrogen concentrations, the tensile stress required to fracture a high strength steel, may be approximated by:

$$F(C) = F_0 - \alpha C \tag{2.13}$$

Where F_0 is the fracture tensile stress with no hydrogen, α is a constant of the material that can be experimentally extrapolated and $F(C)$ is the cohesive force between the metal atoms in the lattice, function of hydrogen concentration.

Concluding, all HEDE-based models contain one or more adjustable parameters owing to uncertain features related to a crack tip problem.

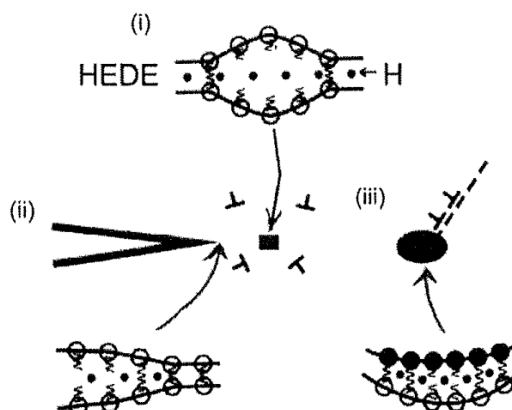


Figure 2.2. HEDE mechanism representation, iron bonds are weakened by hydrogen in the lattice, dislocation can increase stress field

2.2.2 Hydrogen Affected Localized Plasticity, HELP and AIDE

It was suggested that H stimulates dislocation mechanics that localize plastic deformation enough, resulting in subcritical crack growth with brittle characteristics on the macroscopic scale. Two variations of this concept have been advanced as the AIDE and HELP mechanisms.

2.2.2.1 HELP, Hydrogen Enhanced Localized Plasticity

It was suggested that dissolved hydrogen atoms enhances the mobility of dislocations, resulting in extreme localization of plastic deformation sufficient to enable subcritical crack growth that is macroscopically brittle. The HELP mechanism differs from AIDE (that will be explained in the next paragraph) in that dislocation mobility is enhanced due to hydrogen accumulation about dislocation cores, resulting in reduced elastic energies of interaction between moving dislocations and a variety of obstacles. Since hydrogen reduces interaction energy, the stress required for dislocations motion is decreased and plasticity is enhanced. The primary evidence for HELP is in situ high voltage electron microscopy of thinned specimens subjected to plastic deformation during exposure to either vacuum or H_2 . These investigations revealed an increased number of dislocations in a pileup, as well as initiation of dislocation motion, due to H_2 introduction to the electron microscope. Studies of hydrogen effects on bulk specimens show decreased flow stress, increased stress relaxation, and altered strain rate sensitivity due to dissolved-bulk hydrogen. However, the geometry of localized flow in such high strength microstructures has not been developed. Modeling of dislocation mobility has not included hydrogen drag on the moving-dislocation line. Finally, the HELP mechanism has not been developed to yield semi-quantitative predictions of K_{TH} or $(da/dt)_H$ [1].

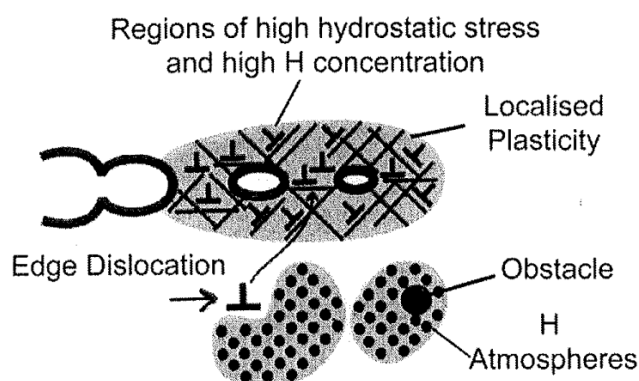


Figure 2.3. HELP mechanism; it supposes the coalescence of microvoids due to local plasticization where high hydrogen concentration is present [1]

In Figure 2.3, the HELP mechanism is shown. The propagation of the crack is supported by the coalescence of microvoids (microdimples) in the plastic zone ahead of the tip.

The figure shows also how hydrogen can minimize the elastic interaction energy between an obstacle and a dislocation, in this way dislocation movement is easier and its pileup can occur at lower stress levels.

A model has been suggested by Sofronis and Birnbaum [30] that considers the decrease in post-yield flow stress, σ_y , depends upon the total concentration of hydrogen atoms per solvent atoms (H/M), C , and the equivalent plastic strain, $\bar{\varepsilon}^p$, according to the hardening relation:

$$\sigma_y(\bar{\varepsilon}^p, C) = \sigma_0(C) \left(1 + \frac{\bar{\varepsilon}^p}{\varepsilon_0} \right) \quad 2.14$$

Material softening follows an assumed relationship:

$$\sigma_0(C) = [(\xi - 1)C + 1] \sigma_0 \quad 2.15$$

Where ξ denotes a material softening parameter (≤ 1 , measured on ductile void growth) that describe the intensity of hydrogen-induced softening, and σ_0 defines the initial yield stress in absence of hydrogen [32].

2.2.2.2 AIDE, Adsorption Induced Dislocation Emission

Lynch [1] argued that H-induced weakening of metal-atom bond strength results in enhanced emission of dislocations from crack tip surfaces where hydrogen is absorbed. AIDE attributes H-enhanced crack growth as predominantly due to this focused emission of dislocations, exactly from the crack front and along intersecting planes that geometrically favour sharp-crack opening and advance rather than crack tip blunting in the absence of hydrogen. During loading, plastic deformation is also triggered within the crack tip plastic zone and microvoids formation, with or without an assist from dissolved hydrogen, could occur. The link-up of voids adds a component to crack advance and maintains a sharp crack tip by interacting with the intense slip bands from crack tip dislocation emission. The crack surface should reflect this advance process and contain facet-like features parallel to the plane that bisects crack tip slip planes, as well as a high density of microvoids if this latter feature occurs. Facets may be parallel to low index planes for certain symmetric slip plane configurations, but also along higher index planes if the crack tip slip state is unbalanced. Intergranular cracking in the AIDE formulation reflects preferential adsorption of hydrogen along the line of intersection between the grain boundary plane and crack front, and perhaps a higher density of precipitates that may form preferentially along grain boundaries. This mechanism is best suited for HEAC; however, hydrogen localization to a crack tip during IHAC could also be result in AIDE. The AIDE mechanism is debated because of weaknesses in the supporting evidence.

The structure of slip about a crack tip in a hydrogen exposed metal has never been characterized sufficiently to show hydrogen stimulated dislocation emission and associated geometric crack extension [2].

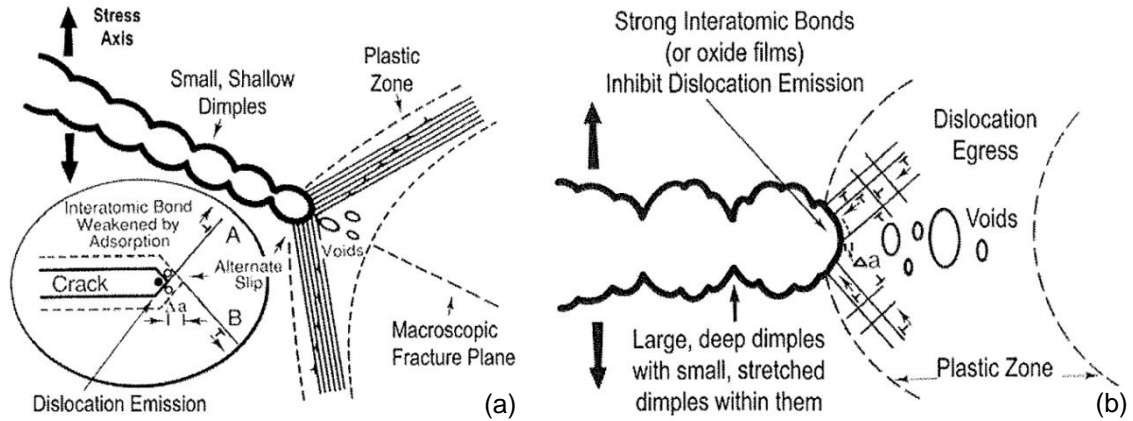


Figure 2.4. Schematic diagrams illustrating (a) the adsorption-induced dislocation emission (AIDE) mechanism for transgranular crack growth, which involves alternate-slip from crack tips facilitating coalescence of crack with voids formed in the plastic zone ahead of cracks, and (b) ductile crack growth involving coalescence of crack with voids by egress of dislocations nucleated from near-crack-tip sources [1]

In Figure 2.4 two different mechanisms for crack growth owing to AIDE mechanism are shown. For this model there are not reliable quantitative relations; in many researches, investigations have been conducted in a short lapse of time and within few atomic planes, so that it is very tough to connect the mechanism to the macro behaviour.

3 Experimental Procedures and Results

Mechanical characterization of the two steels analyzed has been done through: tensile, Charpy impact, toughness and fatigue crack growth tests. All tests have been designed and carried out accordingly to international regulation ASTM or ISO. Since some tests aspects were not completely standardized, regulations have been applied with some change every time it was necessary. Tests were carried out in a range of temperature between $T=-128^{\circ}\text{C}$ and $T=23^{\circ}\text{C}$ for hydrogen charged and uncharged specimens; in fatigue crack propagation tests, also the change in load frequency was chosen as a parameter to be investigated. Specimens were charged with a diffusible hydrogen content of about 2ppm. It was then verified that also small amounts of hydrogen are able to remarkably affect mechanical behaviour of steels and that it also depends on temperature and load frequency. At the same time, numerical models have been developed to simulate and predict Charpy impact, thermal exchange properties and stress state for C(T) specimens with and without side grooves (side notches, provided on specimens lateral surface along the crack growth direction, that allows better crack propagation in toughness tests). These simulations allowed to design and evaluate test results more critically. It was assessed that, for very ductile steels, toughness tests should be carried out with side-grooved specimens.

An innovative electrochemical non-hazardous hydrogen charging technique [33] has been developed at the Chemical department CMIC “Giulio Natta” of the Politecnico di Milano. Thanks to this technique, it has been possible to control the amount of hydrogen in the metal lattice and hence to perform mechanical tests on H-charged material.

Hydrogen charging of steels results in a complex interaction between solute hydrogen atoms and all the microstructural components in the material [1]. Consequently effects of hydrogen on mechanical properties of steels depend on many parameters: composition, microstructure (phases, constituents, precipitates, inclusions) and macrostructure (banding, segregations) of the steel, hydrogen charging conditions (source of hydrogen, temperature, surface conditions, stress/strain conditions during charging) and testing conditions (temperature, deformation rate, specimen preparation, orientation and dimensions).

Such a complex correlation causes scatter in the experimental results and sometimes contradictory evidences. For example, ductility, in terms of reduction in area (RA) or elongation, is always reduced in presence of hydrogen, for low alloy and pressure vessel steels [34][35], while the effect on yield strength is not always consistent, both increase and decrease have been reported by different Authors in presence of hydrogen [35][36]. Hydrogen can also affect the fatigue limit [37] and fatigue crack growth rate [20][38][39]. Concerning fracture mechanics tests, most of them are oriented to the measurement of K_{ISSC} in sulphide stress cracking tests around room temperature ($25\div 35^{\circ}\text{C}$), the more

critical range for the occurrence of this phenomenon in carbon and low alloy steels [40][41][42][43].

For pipeline steels API 5L X65 and X80 critical CTOD, measured under cathodic hydrogen charging, decreased with increasing cathodic current density, increasing hydrogen pre-load time and decreasing strain rate during testing [44][45].

ΔK vs da/dt curves have been measured on high strength low alloy steel (0.05C-1.30Mn-0.22Ti) quenched and tempered at different temperatures and electrolytically charged with hydrogen [46] in order to obtain K_{th} values and crack growth rates in different metallurgical conditions.

Some indications about the effect of hydrogen on mechanical properties can be derived also from some burst tests or failure analyses [47][48][49]. Tests carried out on pressure vessel ASTM A516 Grade 70 steel showed that the critical CTOD value after hydrogen charging in NACE solution for 96-120 hours decreased with respect to the value measured on the same material not containing hydrogen [50]. A brittle failure of a 10" pipeline steel (API 5L X42) carrying sour gas initiated from a groove-like flaw associated with an ERW weld seam (cold weld): the toughness of the weld material was estimated $74\text{MPa}\cdot\text{m}^{1/2}$ for the original material while in the failed one the toughness decreased to $49\text{MPa}\cdot\text{m}^{1/2}$ [49].

Decrease of impact strength, ductility (reduction in area in tensile test) and fracture toughness of pipeline steel X52 after 30 year service in gas pipelines has been verified, more pronounced in the down-in parts of the pipe [51]. According to the opinion of the Authors of this research, the main factor of the decreasing of the mechanical properties was the microdamage, which has been indirectly confirmed by the increased hydrogen trapping. The reduction of the fracture toughness for a pipeline steel API 5L X70 has been reported in [52]. From the data reported it is clear that literature results about the effect of hydrogen on mechanical properties on ferritic steels are not very abundant and the results are not always consistent. Moreover, most of the available results are relative to room temperature tests, therefore, in order to measure the combined effect of hydrogen and very low temperature on fracture toughness of carbon and low alloy steels, in the present research tests were carried out in a wide range of temperatures below room temperature on specimens pre-charged with hydrogen.

3.1 Materials characterization

Experimental tests have been carried out by means of specimens cut from two seamless pipes. Both the materials are very "clean" and produced through a normal commercial production line. The two steels, which have been investigated in this research, are widely used in piping for oil transportation and are the following:

- $2^{1/4}\text{Cr-1Mo}$ steel, namely ASME SA-182 F22 [53]
(pipe: outer diameter=320mm, thickness=65mm);
- Micro-alloyed C-Mn steel, API 5L X65 grade [54]
(pipe: outer diameter=323mm, thickness=46mm).

F22 steel pipe is a Q&T pipe from ingot casting-forging-piercing-hot rolling-quench and tempering production route.

X65 steel pipe is a Q&T pipe from conventional billet casting-piercing-hot rolling-quench and tempering operations. Both materials are for sour service use, so that they underwent through all the required qualifications.

3.1.1 SA-182 F22 steel

The first steel, also known with the commercial name SA-182 F22, according to ASME regulation [53], is forged steel. This steel is designed for high temperature and high pressure working conditions. Its good mechanical properties rely on a fine dispersion of molybdenum carbides and a small amount of chromium that increases corrosion properties. According to regulation its mechanical properties are guaranteed until $T=600^{\circ}\text{C}$.

The chemical composition in weight percentage of F22 (also known as $2\frac{1}{4}\text{Cr-1Mo}$) is shown in Table 3.1.

Table 3.1. Chemical composition [wt%] of F22

Material	C	Mn	S	P	Si	Cr	Mo
F22	0.05 - 0.15	0.3 - 0.6	0.025	0.025	0.5	2.0 - 2.5	0.87 - 1.13

This steel according to ISO regulation is named 10 Cr-Mo 9-10. In Table 3.2 the mechanical and physical properties from literature are reported.

Table 3.2. Mechanical and physical properties of F22 steel

Properties	Temperature [K]	Value
E [MPa]	293.15	206500
	153.15	219942.8
ν	293.15	0.288
	153.15	0.27625
c_p [kJ/kg K]	293.15	0.442
	153.15	0.27625
α [$^{\circ}\text{C}^{-1}$]	293.15	$1.11 \cdot 10^{-5}$
	153.15	$9.54 \cdot 10^{-6}$
k [W/m K]	293.15	36.3
	153.15	28.5
ρ [kg/m^3]	293.15	7860

All specimens that have been used in mechanical tests were made from the pipe bulk, provided by *Ring Mill*; the steel was first forged, then hot worked and finally quenched. In Table 3.3 the chemical composition, experimentally identified, is shown and in Table 3.4 hardness profile along thickness direction is reported. It was observed a good homogeneity of hardness along the whole thickness. These measurements were carried out at Centro Sviluppo Materiali (CSM).

F22 microstructure along thickness is shown in Figure 3.1.

Table 3.3. Chemical composition experimentally observed [Wt%] for F22

Material	C	Mn	Cr	Mo	Ni	Nb	V	Ti
F22	0.14	0.43	2.25	1.04	0.08	0.023	<0.01	<0.01

Table 3.4. Hardness values along thickness for F22

	F22 - HV 10			Average
	OD	193	192	192
MW	195	192	187	193
ID	190	187	187	188

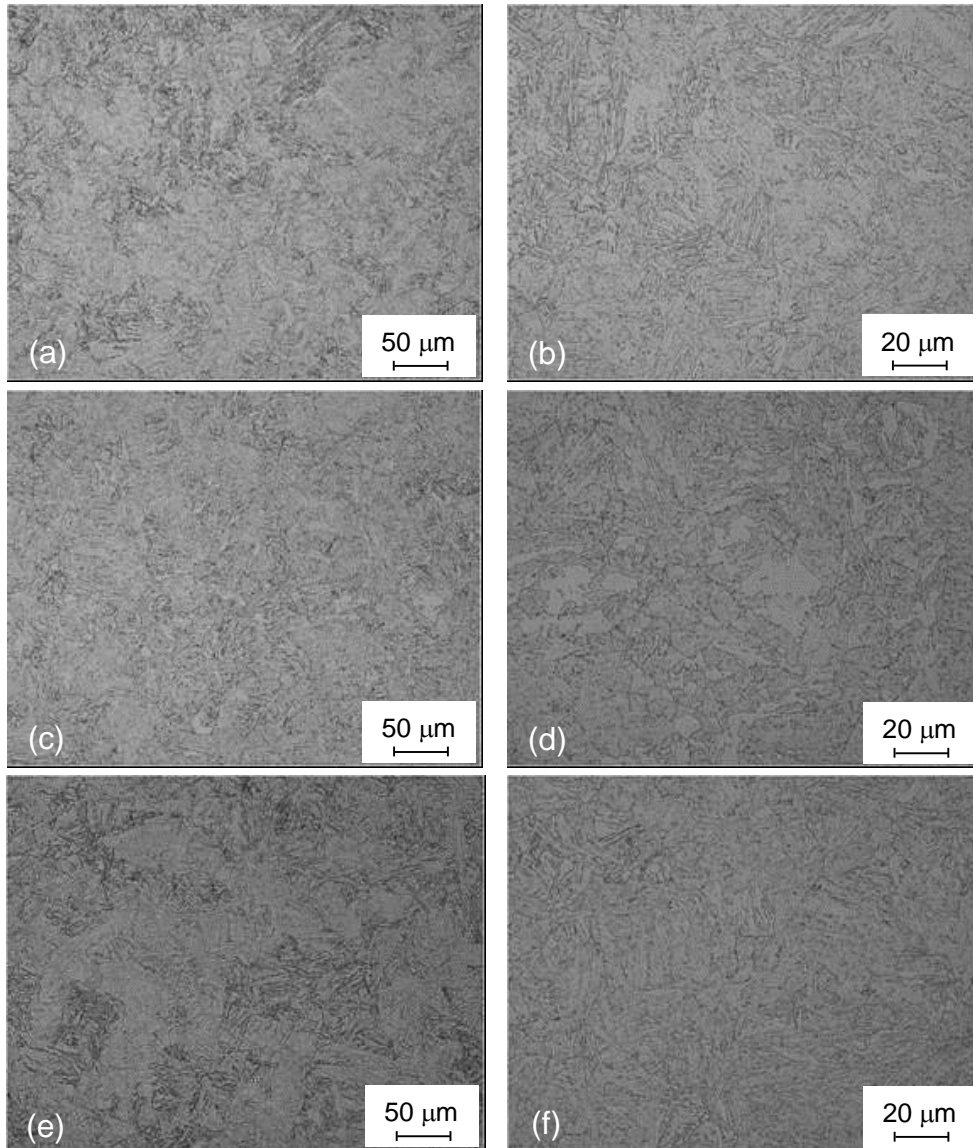


Figure 3.1. Microstructure of F22 steel along thickness; top (a, b) middle (c, d) and bottom (e, f) of the pipe

section

F22 steel is a low alloy steel with 2.25%Cr and 1%Mo, the microstructure is typical of tempered lath martensite, i.e., elongated ferrite grains with finely dispersed carbides. Microstructure is homogeneously distributed along thickness and formed by martensite and bainite. Metallographic attacks also show prior-austenitic grains; the microstructure is rather homogeneous. Inclusion density is very low; material has been treated with calcium and inclusion shape is round (type D globular inclusions) and no elongated inclusions are present; longitudinal and transverse orientation don't show any difference neither as inclusion density nor as mean diameter (1.2 μ m long. surface, 1.3 μ m transv. surface); no central segregation is present.

Specimens for testing were made out directly from the pipe material as depicted in Figure 3.2, where it is possible to distinguish: tensile specimens [55], CV specimen [56][57], and CT specimens [58].

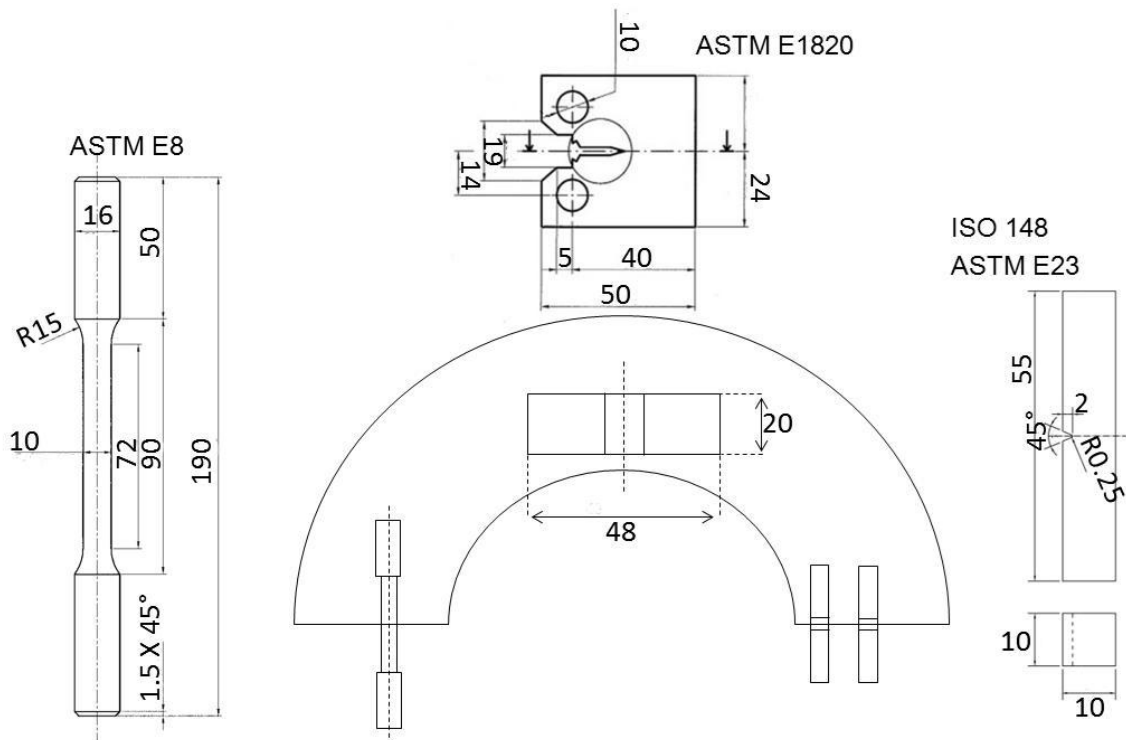


Figure 3.2. Specimens designing for tests

Three tensile tests have been carried out to obtain static properties of the material according to standard [55]. Average test results are shown in Table 3.5.

Table 3.5. Mechanical properties experimentally observed for F22

Material	σ_{YS} [MPa]	σ_{TS} [MPa]	E [MPa]	A [%]
F22	468 \pm 2.7	592 \pm 2.1	206500 \pm 1500	20 \pm 2.5

As it can be noticed, material properties are typical of ductile steel, dispersion of results is well-centred. The characteristic stress-strain curve for F22 is shown in Figure 3.3.

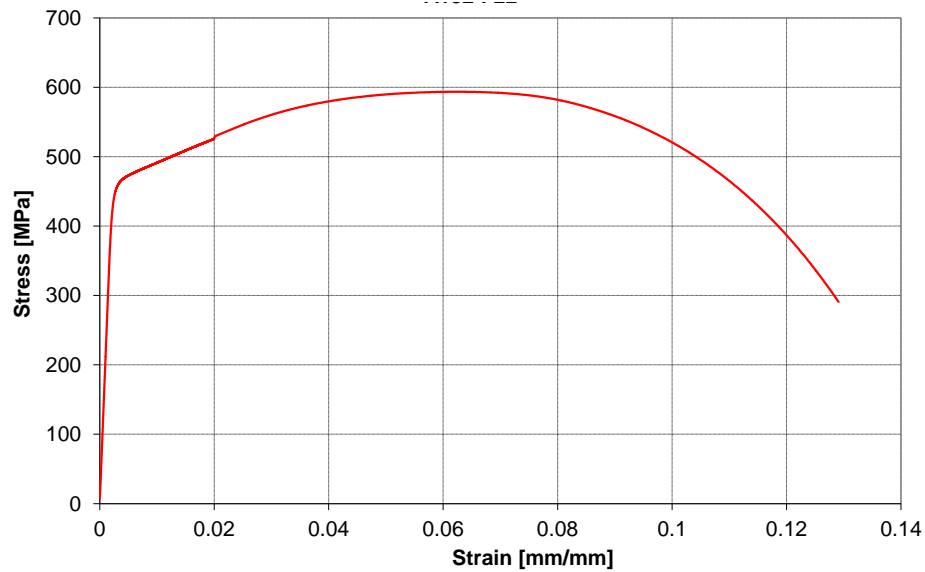


Figure 3.3. Stress-strain curve for F22 steel

All tests results and curves are very similar, for this reason only one curve is shown.

3.1.2 API 5L X65 steel

The second steel is commercially named API 5L X65. Its standard is API [54] that is translated with few differences in ISO [59]. This steel is mainly used in piping for petroleum and natural gas transportation.

Pipes are produced according to two different techniques: seamless and welded; in our case pipes are seamless. The chemical composition of X65 in weigh percentage is shown in Table 3.6.

Table 3.6. Chemical composition [wt%] of X65

Material	C	Mn	P	S	V	Nb	Ti
X65	0.28	1.4	0.03	0.03		Sum < 0.15	

X65 is a low alloy steel with 1.4% of manganese that increases toughness and quenching properties. In Table 3.7 mechanical and physical properties of X65 are reported.

Table 3.7. Mechanical and physical properties of X65 steel

Properties	Temperature [K]	Value
E [MPa]	293.15	206208
	153.15	212196
ν	293.15	0.301
c_p [kJ/kg K]	293.15	0.489
	153.15	0.2843
α [$^{\circ}\text{C}^{-1}$]	293.15	$1.05 \cdot 10^{-5}$
	153.15	$9.38 \cdot 10^{-6}$
k [W/m K]	293.15	35.8
	153.15	28.1
ρ [kg/m^3]	293.15	7860

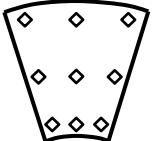
All specimen were made directly from the seamless pipe provided by Tenaris S.A. company.

Specimens were made out of the pipe according to the Figure 3.2, pipe's outer diameter is equal to $D_o=323\text{mm}$ and thickness $t=46\text{ mm}$. The chemical composition, experimentally observed, is reported in Table 3.8. In Table 3.9 hardness profile along thickness is shown.

Table 3.8. Chemical composition experimentally observed [Wt%] for X65

Material	C	Mn	Cr	Mo	Ni	Nb	V	Ti
X65	0.11	1.18	0.17	0.15	0.42	0.023	0.06	<0.01

Table 3.9. Hardness values along thickness for X65

	X65 - HV 10			Average
	OD	243	240	243
MW	195	194	193	194
ID	220	220	221	220

Hardness profile is less homogeneous than F22; hardness is higher near the outer diameter and lower close to the inner diameter. X65 microstructure along thickness is shown in Figure 3.4.

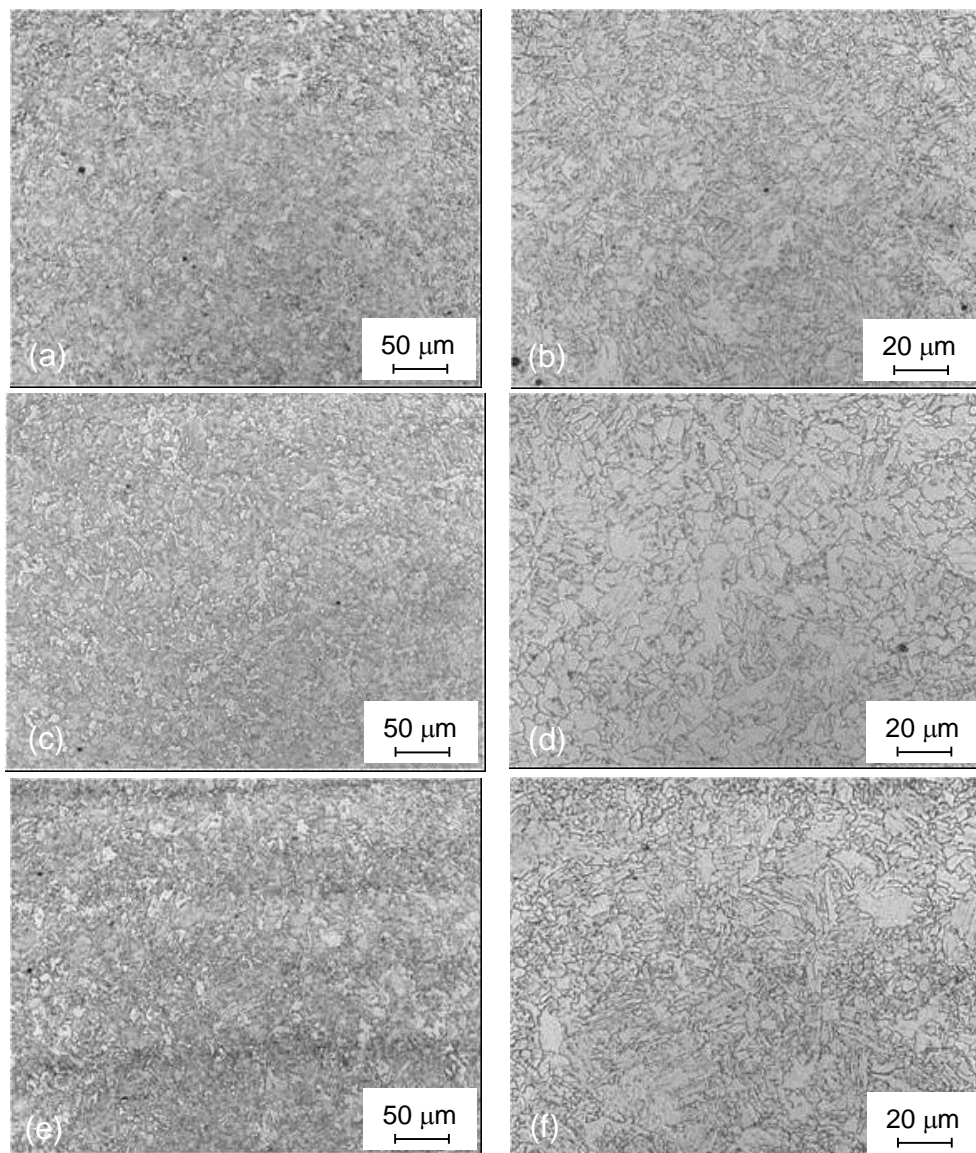


Figure 3.4. Microstructure of X65 steel along thickness; top (a, b) middle (c, d) and bottom (e, f) of the pipe section

Near the centre of the pipe, acicular ferrite can be noticed, X65 has a less well-distributed microstructure along thickness, nevertheless distribution is well acceptable; ferrite structure is non equiaxed and it was formed during a continuous cooling process at temperature slightly above upper bainite and also bainite is present near the outer diameter. X65 steel is a C-Mn steel with Ti as carbide former, a small amount of Cr, Mo and Ni has been added to improve hardenability and Ca for the inclusion shape control. The microstructure is a rather homogeneous equiaxed and acicular ferrite with finely dispersed carbides. Inclusion shape is round (type D globular inclusions) as it is expected for a “sour gas” material treated with calcium and no elongated inclusions are present. Longitudinal and transverse orientation don’t show any difference neither as inclusion density nor as mean diameter (1.5 μm long. surface, 1.4 μm transv. surface); no central segregation is present; inclusion density is rather high and on the external surface is higher.

slightly lower and with larger dimension (mean diameter $1.7\mu\text{m}$ and maximum diameter up to $7/8\mu\text{m}$).

Five tensile tests have been performed at room temperature to obtain static properties of the material according to regulation [55]. Average test results are reported in Table 3.10.

Table 3.10. Mechanical properties experimentally observed for X65

Material	σ_{YS} [MPa]	σ_{TS} [MPa]	E [MPa]	A [%]
X65	511 ± 6.7	609 ± 5.7	206208 ± 6049	21 ± 6.5

It was observed that mechanical properties of X65 are those typical of ductile steels, results dispersion is well concentrated; compared to F22, X65 shows a higher, though still good, results dispersion.

Stress-strain curve from one of the tensile tests is depicted in Figure 3.5.

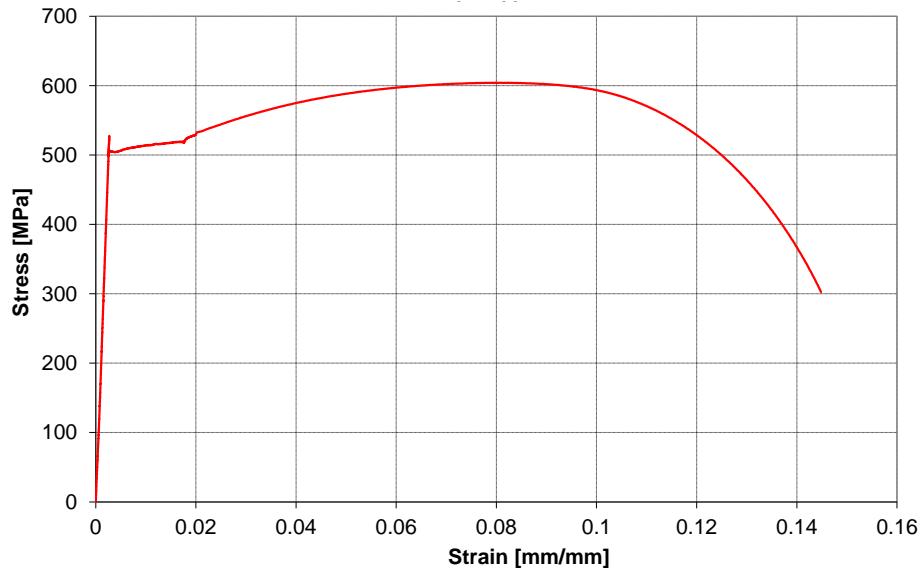


Figure 3.5. Stress-strain curve for X65 steel

All other stress-strain curves are similar to this one and it's worth nothing to show them.

3.2 Electrochemical hydrogen charging

The electrochemical hydrogen charging technique has been developed at CMIC “Giulio Natta” of the Politecnico di Milano. The method has the primary purpose to obtain controlled and reproducible charging conditions in an environment that can be prepared, handled and disposed in a simple and safe way. Hydrogen content charged into thick steel specimens should be comparable to that found in pipeline steels after a long service time.

The bibliographic review showed that some practical procedures were already available for hydrogen charging on ferritic carbon or low alloy steels although they did not seem applicable to our target, mainly because most of the authors used rather small and thin specimens [33], The basis for the setup of the hydrogen charging method was the work of Newman and Shreir [60], that is the most complete, accurate and reliable. The parameters of this method finally set up in CMIC laboratories for electrochemical hydrogen charging of mechanical testing specimens (CV and CT) have been:

- Solution: 0.4mol L^{-1} of CH_3COOH + 0.2mol L^{-1} of CH_3COONa , buffered at pH 4.3 and with 600ppm of sulphide as $\text{S}^{=}$ from hydrated sodium sulphide;
- complete de-oxygenation with pure N_2 ;
- room temperature, $T=25\pm 3^\circ\text{C}$;
- magnesium as anode material;
- current density equal to 0.5mA/cm^2 for 20hours.

An approximate estimation of the hydrogen content of the specimens charged in different conditions has been systematically made by using the hot glycerol method. This method is very simple and quick, then it is suitable for a routine control but underestimates the actual hydrogen content [61]. A detail of the apparatus is shown in Figure 3.6 in which it is possible to observe the hydrogen molecules that rise from the charged specimen into the funnel.

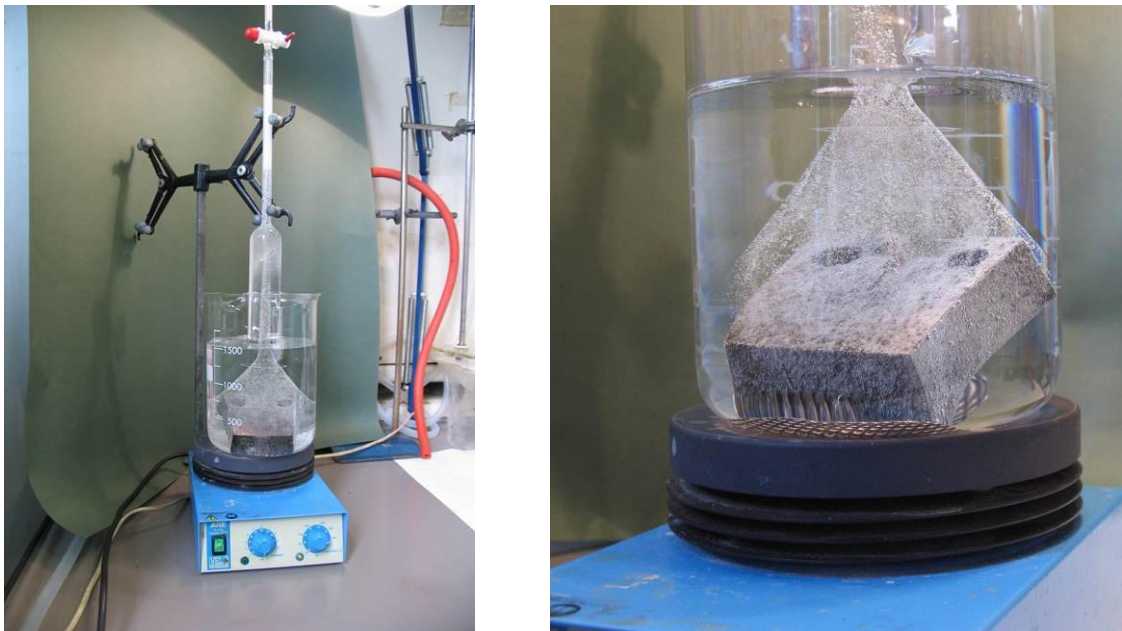


Figure 3.6. Apparatus for the determination of diffusible hydrogen in steel

A control measurement was performed in external laboratories, using a commercial LECO hydrogen analyser. The two methodologies were in general agreement. The details of the experiments are reported in the paper [33].

3.3 Cooling and transportation technique

As mentioned, tests needed to be performed among a large number of specimens varying temperature and in particular at very low temperatures. After the charging process, specimens were transported using two different techniques in order to maintain the hydrogen inside the bulk: the first method consists in an electroplating with a thin layer of nickel and a thicker one of copper for a total thickness of 25-28 μm , in order to decrease the diffusion coefficient outward, while the second method consists in keeping the specimens in a liquid nitrogen thermostatic bath, during the transportation, at $T=-196^{\circ}\text{C}$, in order to reduce the diffusion coefficient in the steel. The second method turned out to be more effective, safe and convenient and, for these reasons, it was embraced.

In order to carry out tests at low temperatures two different cooling techniques have been used:

- MTS 651 environmental chamber;
- ethanol-liquid nitrogen thermostatic bath.

In impact test, only the bath is used in order to reach the test temperature whereas in toughness and fatigue tests the temperature is primarily gotten with the bath and then maintained during the test with the environmental chamber.

3.3.1 Environmental chamber

The environmental chamber, shown in Figure 3.7, uses liquid nitrogen to set gas temperature until $T=-128^{\circ}\text{C}$. Nitrogen stored inside the vessel vaporizes when it reaches the chamber. Outside the chamber there is a control unit able to adjust the amount of nitrogen flowing inside the chamber and then able to keep a stable temperature inside, temperature then can be manually set.

Temperature inside the chamber is measured by a thermocouple placed in the bottom of the chamber, close to the gas flow-in grid. Environmental chamber was used for toughness and fatigue crack growth tests. In Figure 3.7, it is also shown the testing machine, MTS 810, used for crack growth and toughness test.

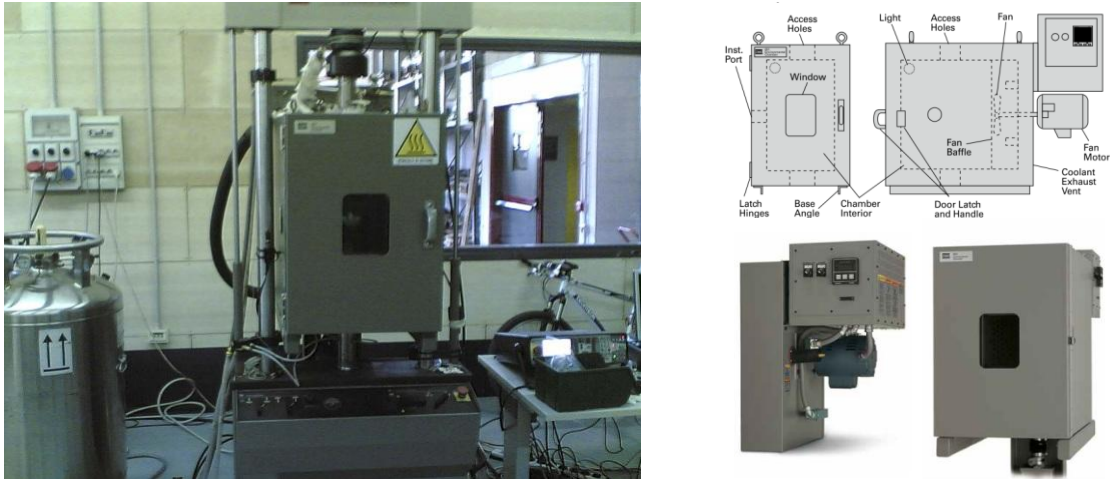


Figure 3.7. Image of the environmental chamber, the testing machine and of the nitrogen vessel

3.3.2 Ethanol-liquid nitrogen conditioning bath

In order to bring the specimens at the testing temperature, a quick and efficacious method was used; it consists in immersing the specimens in an ethanol-liquid nitrogen bath, kept at the requested temperature by adjusting the correct proportion between ethanol and liquid nitrogen. The equipment includes a small insulated plastic vessel with a void zone between the inner and outer surfaces and a lid on top as shown in Figure 3.8.



Figure 3.8. Image of the insulated vessel for Charpy specimens cooling whose temperature is controlled by a thermocouple

A thermocouple, bound to a weight is placed inside the vessel to control the bath temperature. Inside the vessel, ethanol and liquid nitrogen, are mixed (liquid nitrogen vaporizes while absorbing heat from ethanol). This mixture can reach temperatures close to $T=-110^{\circ}\text{C}$, indeed $T=-114^{\circ}\text{C}$ is the ethanol solidification temperature. Then by controlling the amount of liquid nitrogen poured inside the vessel it is possible to control the bath temperature.



Figure 3.9. Ethanol-liquid nitrogen bath inside the thermal vessel

It is quite complicated to reach temperatures close to $T=-110^{\circ}\text{C}$ because ethanol tends to solidify, going towards a jelly state; only through a careful stirring it is possible to keep the bath in a liquid state.

Once the correct temperature of the bath is reached it is possible to immerse the specimens inside. In case of a liquid environment, the regulation suggests to keep the specimen for at least 5 minutes inside. When the cover is closed the temperature inside the vessel is maintained constants and the thermocouple enables to check the temperature. Charpy specimens are one bulk piece with no holes and quite thin, for this reason it is not possible to monitor the temperature inside them; nevertheless it is reasonable to say that thanks to the long immersing time the correct temperature is reached throughout the whole specimen. This bath was used for all tests; indeed, for Charpy impact energy, it is sufficient to bring specimen at the requested temperature while for other tests (crack growth and toughness) it was used to bring the specimen at the test temperature faster than keeping it inside the environmental chamber.

3.4 Charpy impact test

Charpy impact tests were performed on CV specimens varying temperature and the position inside the pipe thickness were they have been extracted. Tests are performed in according to regulation [56][57]. For impact tests, it was used a Charpy pendulum as shown in Figure 3.10; pendulum was calibrated before testing.

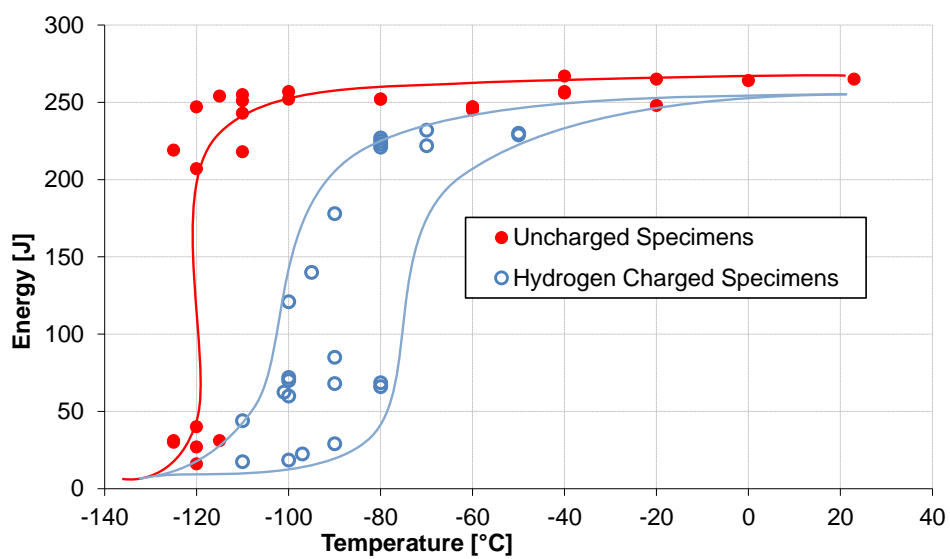


Figure 3.10. Charpy pendulum for Impact tests presents at Falco laboratories (Politecnico di Milano)

3.4.1 Charpy impact test results: F22 steel

In Figure 3.11 the Charpy impact energy values as a function of temperature for F22 steel are depicted. Ductile-brittle transition temperature (DBTT) is defined accordingly to standard [56] corresponding to an energy of 27J.

It comes out clearly that for hydrogen charged specimens DBTT is much higher than the one for uncharged specimens. In Figure 3.12 the percentage of brittle area as a function of temperature is depicted.



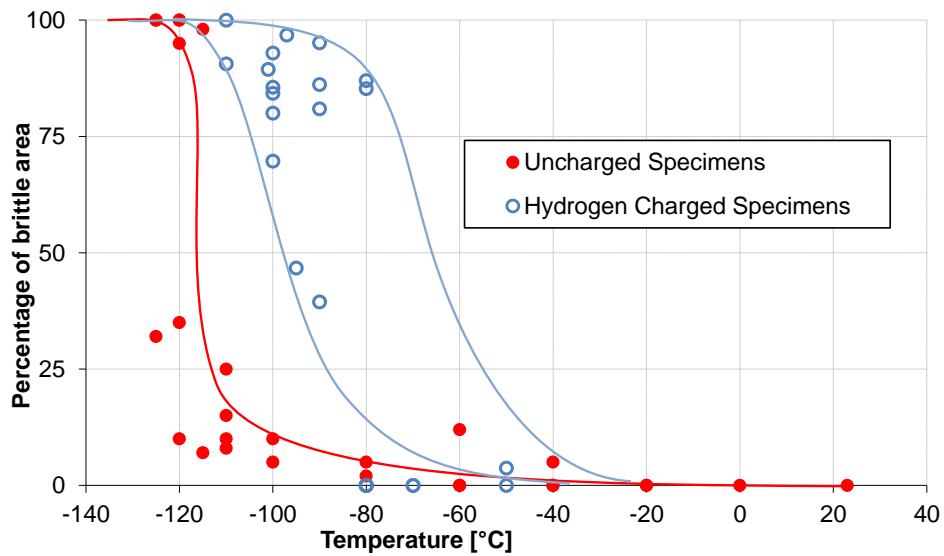


Figure 3.12. F22 steel: percentage of brittle area as a function of temperature

3.4.2 Charpy impact test results: X65 steel

In Figure 3.13 resilience values as a function of temperature are depicted for X65 steel. Figure 3.14 shows the percentage of brittle area as a function of temperature for X65 steel.

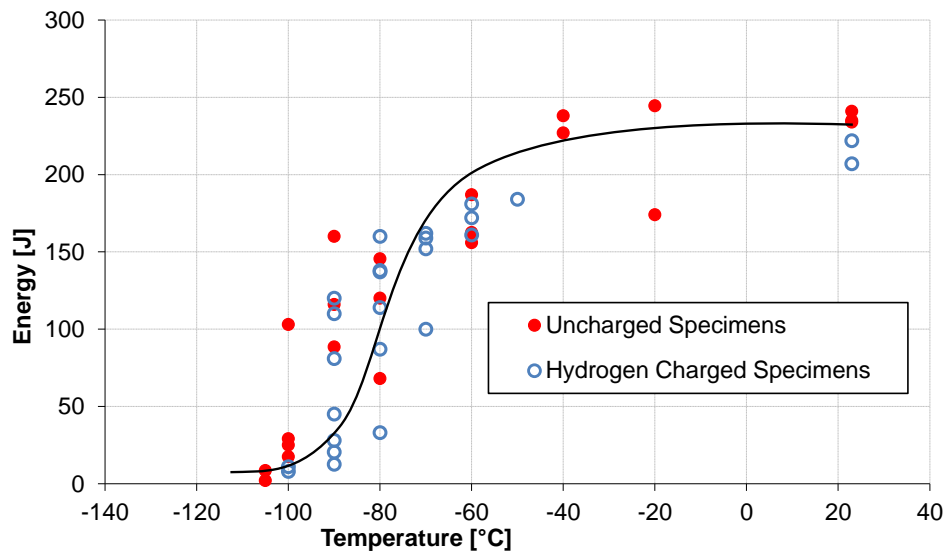


Figure 3.13. X65 steel: impact energy as function of temperature

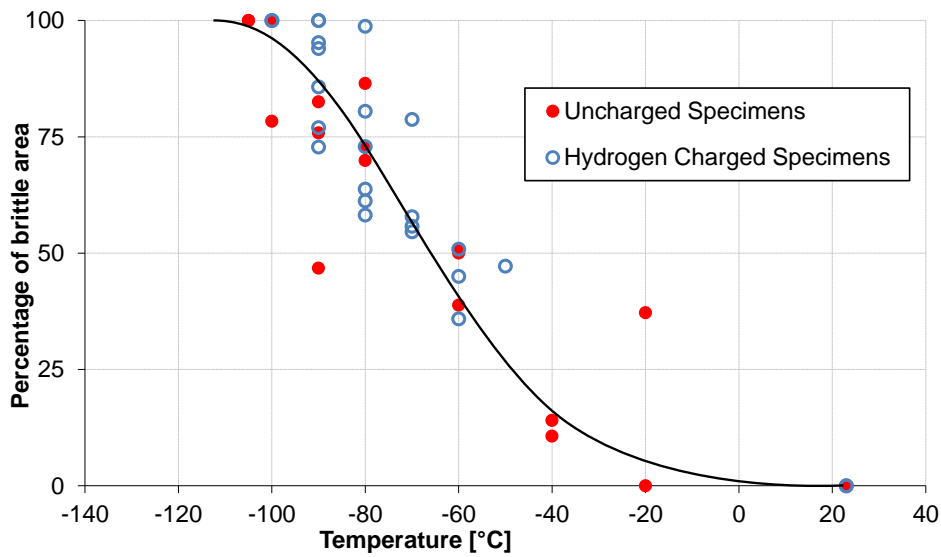


Figure 3.14. X65 steel: percentage of brittle area as a function of temperature

3.4.3 Remarks on results

It was observed a remarkably different behaviour between X65 and F22 steels whether hydrogen charged or uncharged. In particular the uncharged F22 steel does not show any change in energy to rupture until a temperature equal to $T=-100^{\circ}\text{C}$: energy, lost during the test whether at $T=-100^{\circ}\text{C}$ or room temperature, is almost the same.

This is supported by the percentage of brittle area: on the specimens, tested at $T=-100^{\circ}\text{C}$, percentage of brittle is between 5-10%. The curve starts to drop slightly around $T=-110^{\circ}\text{C}$; while for lower temperatures, of about $T=-120^{\circ}\text{C}$, ductile-brittle transition occurs.

The transition zone of hydrogen charged specimens is larger and the energy values are more scattered. The BDTT of charged F22 specimens increases of about 30°C with respect of the uncharged specimens, if it is considered the value in correspondence of an impact energy of 27J. By considering, on the contrary, the FATT value the increase is in the range of 20°C .

As it can be seen from plots in Figure 3.11 and Figure 3.12, in charged specimens, at temperatures around $T=-90^{\circ}\text{C}$ brittle behaviour occurs. Moreover, it was observed the difference in the transition temperature: it appears clearer for uncharged specimens while for charged specimens the transition is “blurred”. Low values of Charpy toughness for F22 steel appear also at temperature equal to $T=-80^{\circ}\text{C}$. In presence of hydrogen upper shelf energy is slightly decreased from 270 to 250J.

For F22 it was found a difference in transition temperatures for charged and uncharged specimens of about 30°C and an increase of the transition temperature from $T=-120^{\circ}\text{C}$ to $T=-90^{\circ}\text{C}$.

The Charpy transition curve of “as received” X65 steel is more scattered and less steep than the one of F22 steel. The transition is less clear: it was observed indeed a broad area between $T=-60^{\circ}\text{C}$ and $T=-100^{\circ}\text{C}$, in which a clear ductile-brittle transition cannot be spotted.

When the material is charged with hydrogen, the increase of BDTT is very limited and a shift of about 10°C only can be appreciated, using both the FATT and the 27J criterion.

The upper shelf energy is slightly decreased from 240 to 220J. An important aspect is the more scattered results for both energy and brittle area values of hydrogen charged samples compared to those of uncharged material.

With respect of ISO [59] standards, for the determination of the ductile-brittle transition temperature (when energy absorption in the impact is equal to 27J), it is still possible to find the transition temperature, in this case, equal to a value around $T=-100^{\circ}\text{C}$.

X65 charged specimens does not show any big difference, even if, a remarkable number of them, show a fragile transition around $T=-90^{\circ}\text{C}$.

It was assumed that hydrogen embrittlement effect, on X65 for high impact rate, is smaller than F22 steel.

3.5 Toughness test

Toughness tests have been carried out at Mechanics Department laboratories at Politecnico di Milano. Test methodology is governed by the standard [58]. Specimens were modified with side-groves according to [62][63]. Materials tested in this research present a strong ductile behaviour and for this reason, it turned out to be very difficult to evaluate K_{Ic} , accordingly to the international regulation that imposes large thickness of the specimens. Therefore it was followed a methodology suitable to determine experimentally the energetic parameter J_{Ic} , equal to K_{Ic} , but with less constrains on specimens thickness. Below, the basic derivation for J -integral calculation is reported for generic specimens. Thanks to instrumentation, it is possible to plot the force applied by the machine to the specimen against the displacement (crack opening). J can be calculated in displacement control through relation 3.1 [64].

$$J = -\frac{1}{B} \cdot \int_0^{\delta} \left(\frac{\partial P}{\partial a} \right)_{\delta} d\delta \quad 3.1$$

Where B is the thickness of the specimen, a is the crack length, P is the load, measured by the loading unit and δ is the displacement measured by an extensometer, as depicted in Figure 3.15.

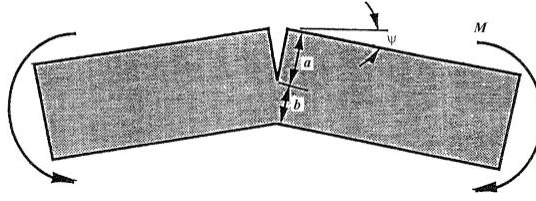


Figure 3.15. specimen under bending force

Bending angle ψ , in the case of a specimen subject to bending, is directly proportional to the momentum applied, equal to $PL/2$ and it is inversely proportional to the yield strength and the product Bb^2 (b is equal to the difference between W and a) that depends on the strength modulus. Taking into account a constant of proportionality C , it can then be rewritten as:

$$\psi = \frac{\delta}{L} = \frac{C \cdot P \cdot L}{2 \cdot \sigma_{sn} \cdot B \cdot b^2} \quad 3.2$$

This can be rearranged to:

$$P = \frac{2 \cdot \delta \cdot \sigma_{sn} \cdot B \cdot b^2}{L^2 \cdot C} \quad 3.3$$

And, deriving equation 3.3 respect to b , it leads to:

$$\frac{\partial P}{\partial b} = \frac{4 \cdot \delta \cdot \sigma_{sn} \cdot B \cdot b}{L^2 \cdot C} = \frac{2 \cdot P}{b} \quad 3.4$$

Since $da = -db$ it can be written as:

$$\frac{\partial P}{\partial a} = -\frac{\partial P}{\partial b} \quad 3.5$$

Then:

$$\frac{\partial P}{\partial a} = -\frac{2P}{b} \quad 3.6$$

It can be rewritten as:

$$J = \frac{1}{B} \cdot \int_0^\delta \frac{2 \cdot P}{b} d\delta = \frac{2}{Bb} \cdot \int_0^\delta P \cdot d\delta \quad 3.7$$

It can be noticed that the integral of the Eq. 3.7 is equal to the area under the plot P - δ in Figure 3.16.

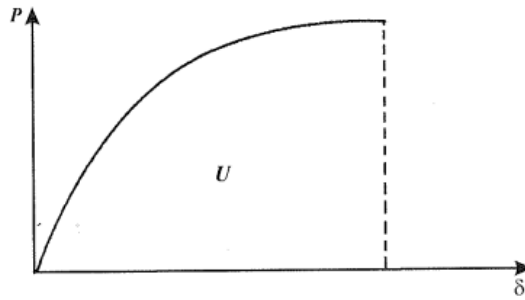


Figure 3.16. P-δ plot registered during the test of J integral

In this case, when specimen C(T) is subject to an aperture according to mode I, the final relation is modified by taking into account the different stress state in the specimen C(T) compared to the one under bending force. The relation then becomes:

$$J = \frac{\eta}{B \cdot b} \cdot \int_0^{\delta} P \cdot d\delta \quad 3.8$$

Where η depends on the ratio a/W and it is slightly higher than 2.

In order to calculate the value of J , tests have been carried out according to ASTM [58] through the compliance method. This method enables to save time and specimens for the calculation of the requested value, because it is possible to plot the whole curve $J-\Delta a$ with just one specimen.

The compliance method is based on the measurement of the compliance C , as indicated in Figure 3.17; it consists in loading the specimen increasing load P , then removing partially the load, measure the compliance and repeat it for every loading ramp. As the crack increase, the specimen becomes more compliant that is less stiff.

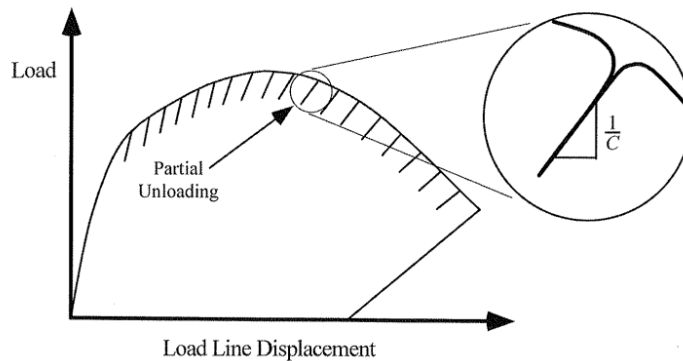


Figure 3.17. Load as a function of displacement during a toughness test: to be noted the decrease of the slope (opposite of compliance) while increasing the displacement.

This process goes on until the last load and/or rupture of the specimen (that could not occur for very tough materials such those one). Figure 3.18 shows a plot of the output data from a real toughness test provided by the testing machine.

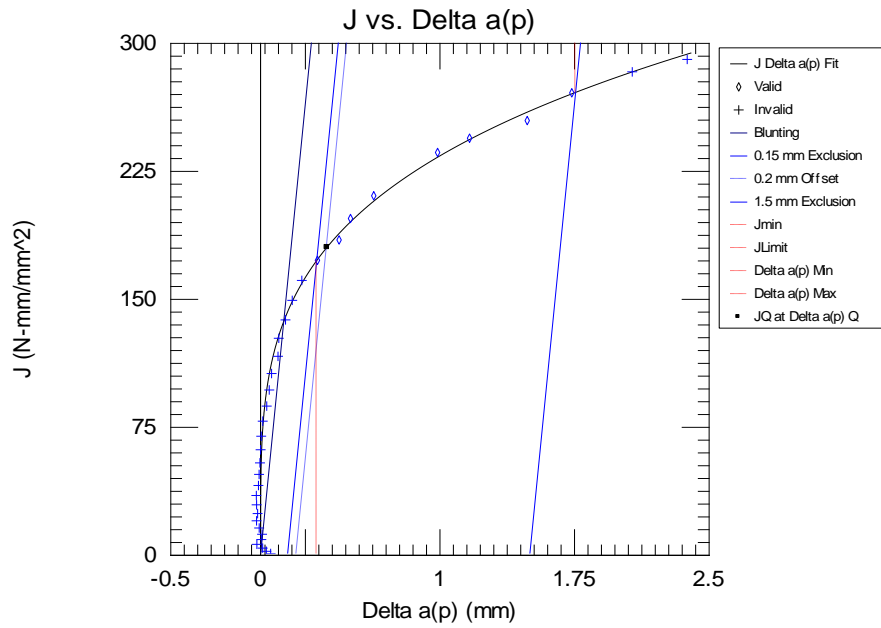


Figure 3.18. Plot of a toughness test output data

The slope of the loading ramps gives the value of the compliance. Through calibration it is possible to obtain the value of the crack length a during the test and the Δa increases. The intersection between the characteristic curve of the material with the *blunting line* (characteristic line indicated by regulation to obtain J_{Ic}) gives the value of J_{Ic} . The *blunting line* can be calculated through this equation.

$$J = 2 \cdot \sigma_{YS} \cdot \Delta a \tag{3.9}$$

Where σ_{YS} is the yield strength. Specimens used in this research are Compact Tension specimens as shown in Figure 3.2. This enables to contain the amount of material needed and to have more compact and easy to handle specimen that has to undergo to different operation such as: hydrogen charging and mechanical testing. Geometry of the specimen is shown in Figure 3.19.

As material, for welding the thermocouple wire (made of copper and constantan) to the specimen, a tin alloy was chosen, because of its good weldability, low melting point and good resistance at low temperatures.

In order to measure the internal temperature of the specimen it was chosen to make a small hole where the thermocouple was welded in, as shown in Figure 3.20a.

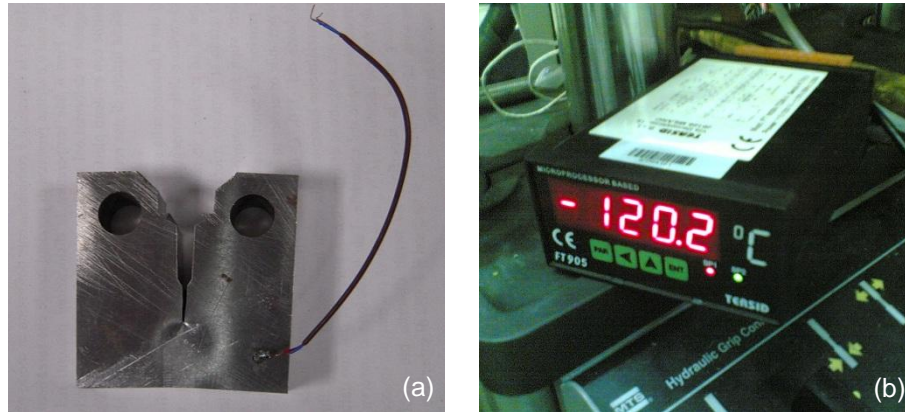


Figure 3.20. (a) Welded thermocouple wire inside the hole and (b) core temperature indication

In Figure 3.20b it is also reported the device used to check the specimen core temperature in order to compare it with the environmental gas temperature.

3.5.1 Fracture toughness test results

Specimens have been hydrogen charged at Chemical Department and transported to the Mechanical Department where tests were performed [65][66][67][68].

Few F22 specimens were kept for 24 hours in air at $T=30^{\circ}\text{C}$ (24h@ 30°C) to assess the presence of hydrogen after being exposed to room temperature. In these conditions it can be expected that a large amount of diffusible hydrogen can escape from the specimen, being the exposure time at room temperature almost the same of the charging one, that is equal to 20 hours.

In Figure 3.21 values of J_q for F22 steel versus temperature are reported. Green dots indicate specimens kept at room temperature in air for 24h.

In Figure 3.22 values of J_q for X65 steel versus temperature are reported.

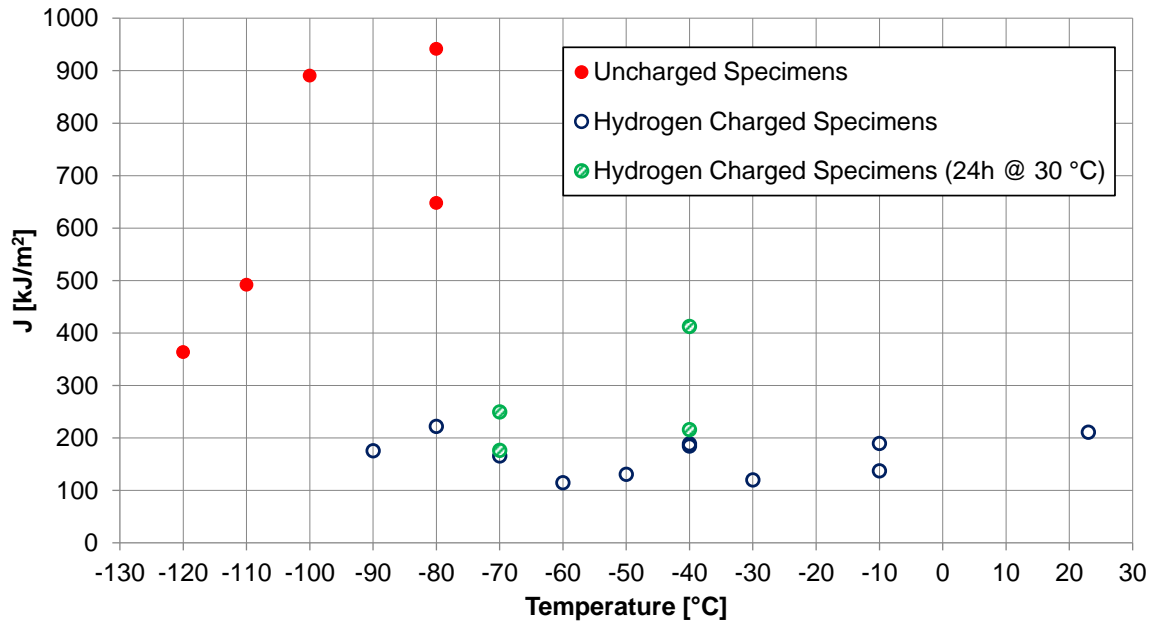


Figure 3.21. F22 steel: J_q values obtained by uncharged and hydrogen charged specimens

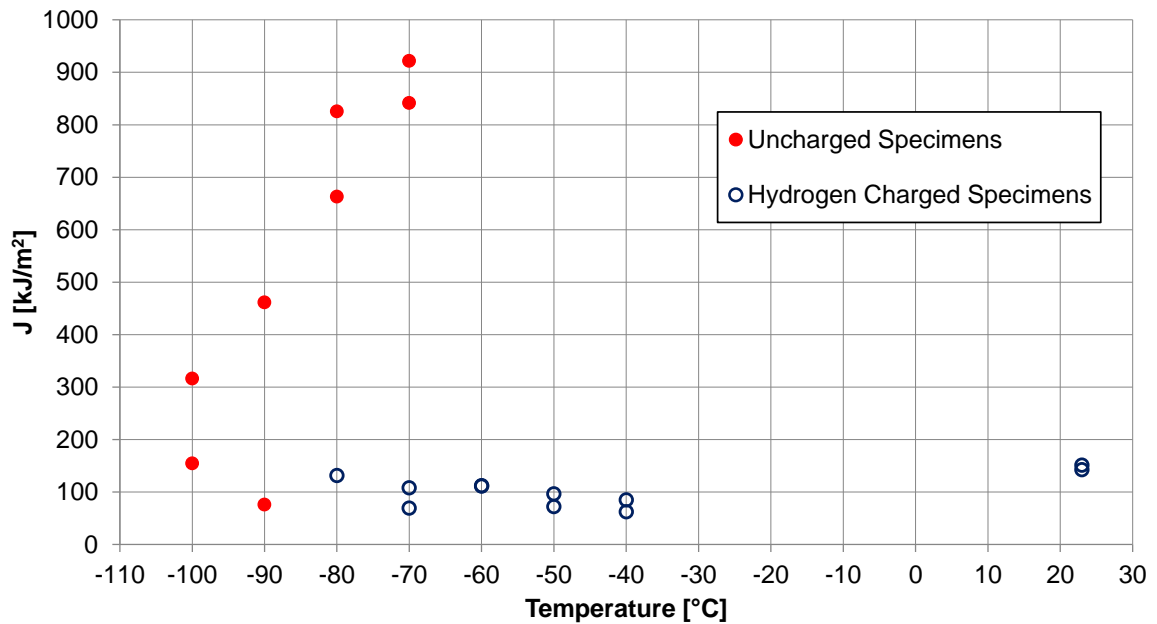


Figure 3.22. X65 steel: J_q values obtained by uncharged and hydrogen charged specimens

The effect of hydrogen charge is more evident if the toughness fracture curves are considered. When material is charged with hydrogen, in fact, J_q values decrease significantly in both steels with respect to the values obtained in the uncharged conditions. It was observed that, for tests that require more time in terms of load speed application, hydrogen embrittlement is enhanced in both steels and remarkable damages occur at temperatures higher than those for impact tests.

Figure 3.21 shows the measured values of J_Q vs. temperature for F22 steel with and without hydrogen. All the specimens, after the hydrogen charge, were maintained in liquid nitrogen while the specimens indicated by dotted circles, in Figure 3.21, were kept in air at room temperature for 24h to allow some diffusible hydrogen to escape from the specimen.

Toughness values of uncharged F22 specimens are larger than 900kJ/m^2 to a temperature of $T=-100^\circ\text{C}$, then they start to decrease. During the tests the cracks never propagate in an unstable way, and also the stable crack propagation is very small. The plastic zone at the crack tip is very extended and the crack tip blunts without considerable propagation.

The J_q values of hydrogen charged specimens are significantly lower and almost constant ($J_q \approx 150\text{kJ/m}^2$) in all the experimented temperature range to the room temperature.

If uncharged specimens, at temperatures around $T=-100^\circ\text{C}$, show still high J_q values, that still depend on thickness size, hydrogen charged specimen show a strong embrittlement, with values that drop until about 100kJ/m^2 at temperatures around $T=-90^\circ\text{C}$.

It must be said that J_q values are still high enough thanks to the good toughness properties of such materials. Finally it should be pointed out that, also specimens kept at $T=30^\circ\text{C}$ for 24h (green dots) show a remarkably reduction of toughness: this means that a relevant quantity of hydrogen was trapped inside other sites with a high activation energy.

Similar considerations are valid for X65 steel: Figure 3.22 shows that the J_q values of the hydrogen charged specimens are significantly lower than uncharged ones and while uncharged material shows a clear transition in the range $-70\div-100^\circ\text{C}$, in the hydrogen charged specimens the J_q value is almost constant ($J_q \approx 90\text{kJ/m}^2$) with the temperature in the range $-80\div-25^\circ\text{C}$.

It is interesting to split the elastic from the plastic part of J_q to better understand the loss of plasticity due to hydrogen.

In Figure 3.23 and Figure 3.24 plots of J_{el} and J_{pl} as a function of the test temperature are shown respectively for F22 and X65 steels.

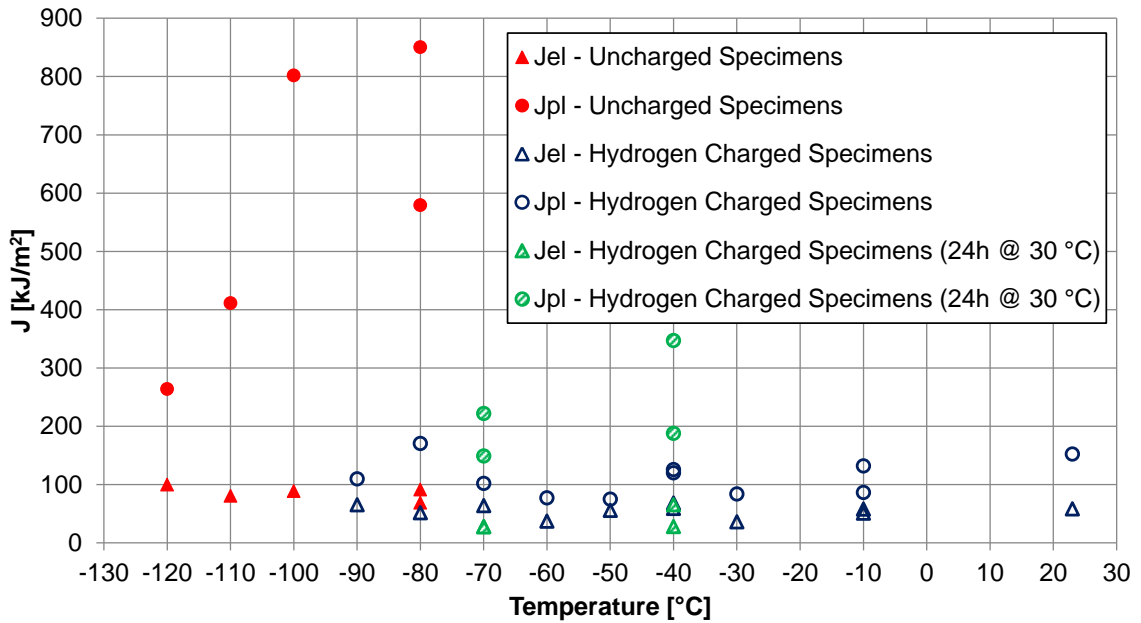


Figure 3.23. F22 steel: J_{el} and J_{pl} components vs. temperature, uncharged and hydrogen charged specimens

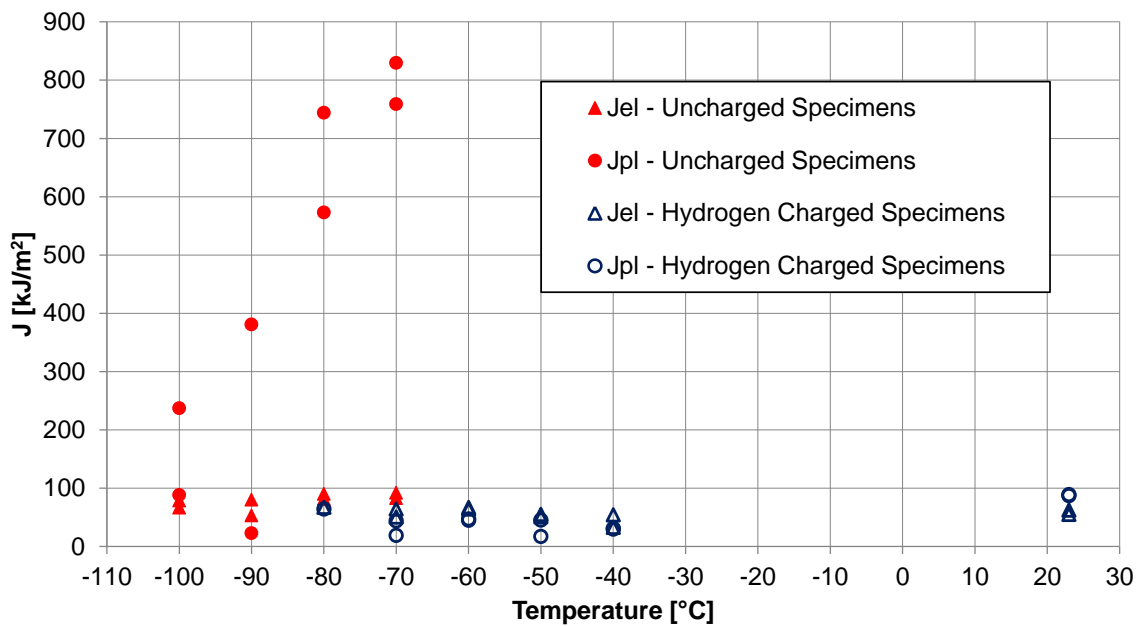


Figure 3.24. X65 steel: J_{el} and J_{pl} components vs. temperature, uncharged and hydrogen charged specimens

It is evident, from the two plots, that for hydrogen charged specimens there is a relevant loss in plastic component: the elastic component is almost constant, in fact, J_{el} is similar either for charged and uncharged specimens; on the contrary, the presence of hydrogen drastically reduces the plastic component. The presence of hydrogen modifies the fracture mode of the material: the plastic part is smaller and the extension of the propagated crack is larger.

This situation can be better shown by load line displacement graph from toughness tests. In Figure 3.25 and Figure 3.26 load curves against load line displacement are shown; for F22, curves at $T=-80^{\circ}\text{C}$ are shown, while for X65 curves are taken at $T=-70^{\circ}\text{C}$ (F22 is tougher than X65).

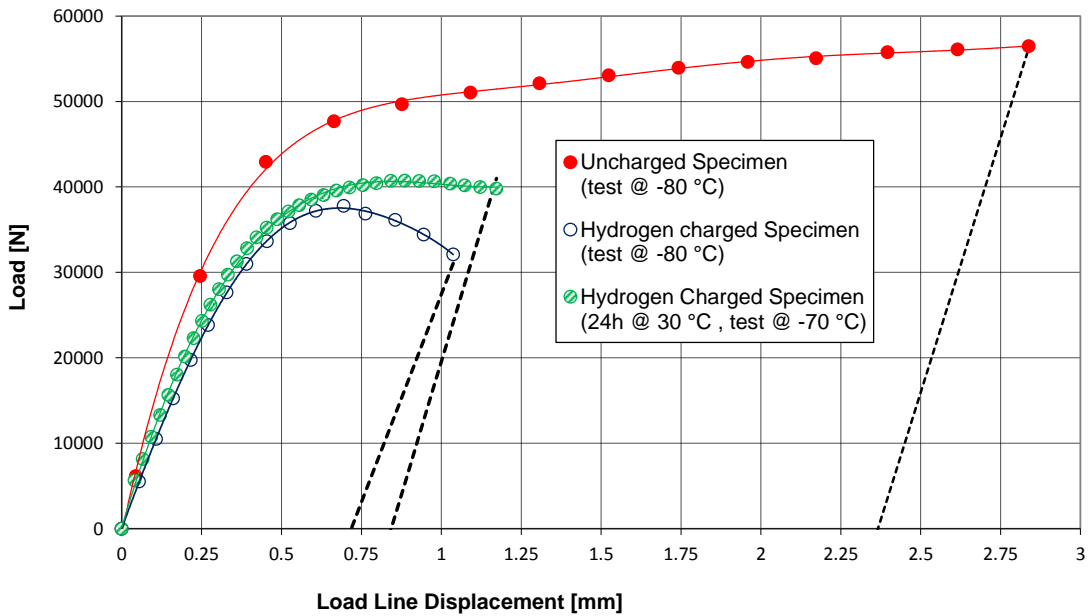


Figure 3.25. F22 steel: Load vs. LLD for uncharged and hydrogen charged specimens

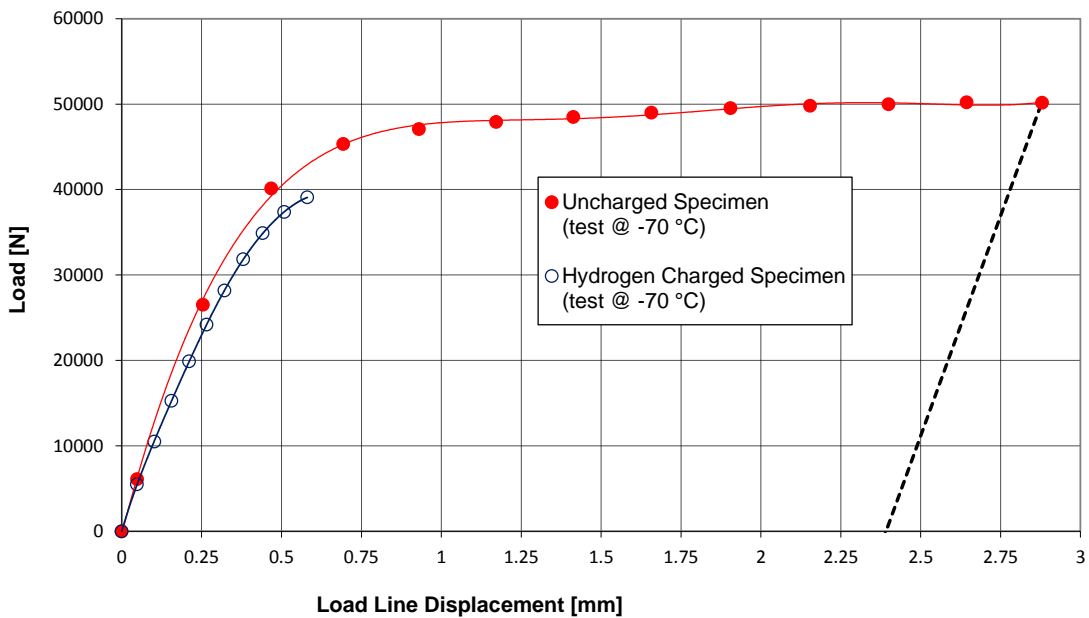


Figure 3.26. X65 steel: Load vs. LLD for uncharged and hydrogen charged specimens

Figure 3.25 shows the comparison among the curves load vs. load line displacement (LLD) for different specimens of F22 steel: uncharged specimen shows a very long plateau with a slightly increasing load and an extremely limited crack extension, the charged one displays a maximum in the load with a much more limited LLD but with a more extended crack propagation; the specimens degassed 24 hours after hydrogen charging show an intermediate behaviour. In no cases there is unstable crack propagation.

It is evident from these plots that, in charged specimens, there is a lower plastic contribution than the one present in the uncharged specimen. The steel changes its mechanical properties and loses toughness.

In Figure 3.26, X65 specimens show the same behaviour of F22 specimens, but it is to underline that the charged specimen shows an unstable crack propagation during test. To better investigate fracture surfaces after toughness test, a heat-tinting thermal treatment was performed on specimens when stable growth occurred during test and no unstable crack propagation occurs at the end of the test. This treatment consists in heating the sample at $T=300^{\circ}\text{C}$ for 30 minutes, quenching in liquid nitrogen and then opening it in a brittle condition. Figure 3.27 shows the fracture surfaces of F22 hydrogen charged and uncharged specimens.

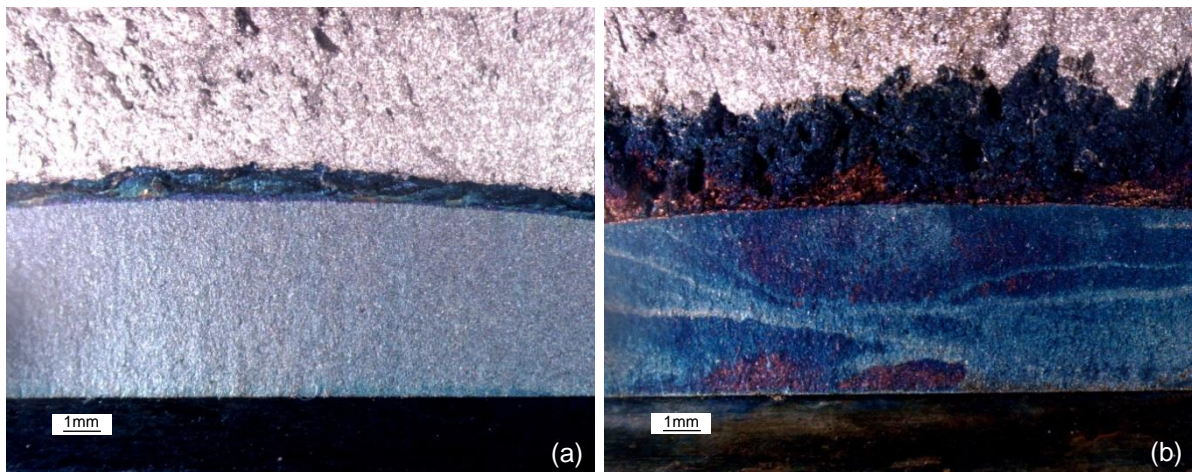


Figure 3.27. Stable crack propagation for F22 specimens: (a) uncharged specimen, $T=-100^{\circ}\text{C}$, $J_q > 890\text{KJ/m}^2$, $\Delta a_{\text{final}}=0.5\text{mm}$ and (b) Charged specimen, $T=-90^{\circ}\text{C}$, $J_q=179\text{kJ/m}^2$, $\Delta a_{\text{final}}=2.5\text{mm}$

It can be observed that, in the uncharged specimen, crack extension is small due to a very tough behaviour; this is confirmed by the correspondent high value of J_q . What happens in reality is a blunting (increase of the tip radius) of the crack tip due to plasticity without tearing of the material. On the other side, in presence of hydrogen, the crack propagations is broad and clear. This will be clarified in SEM fractographic analysis. Heat-tinting is also useful in order to estimate the mean crack length, as reported in the standard [58]. In Figure 3.28, the propagation occurred in a non-side-grooved specimen is compared with one in a side-grooved specimen.

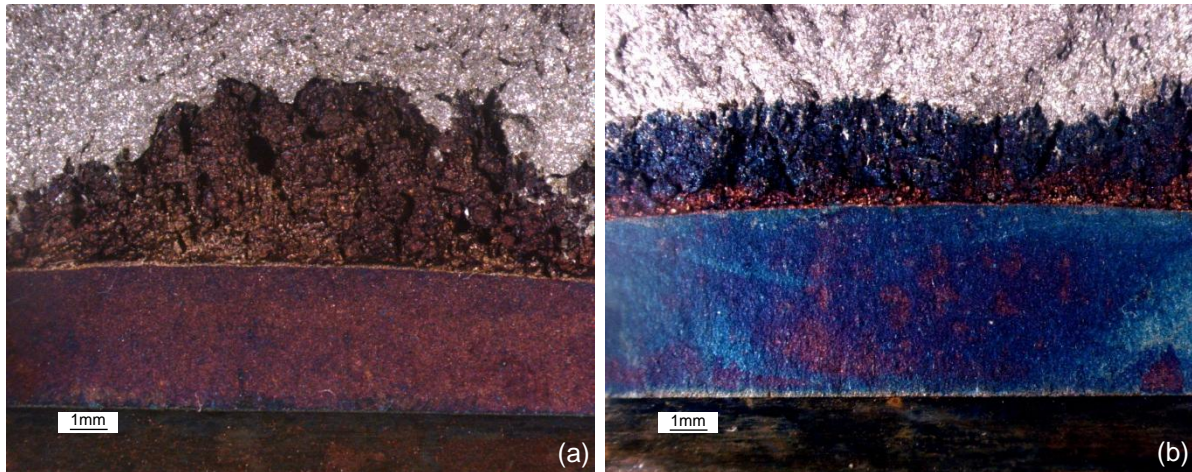


Figure 3.28. Propagation in (a) non-side-grooved specimen and (b) side-grooved specimen

It is possible to observe that, the using of side-grooves, allows to provide a straight and more constant crack front instead of the half-moon shape produced without side-groove.

3.6 Fatigue crack growth test

Fatigue crack propagation is usually described through da/dN - ΔK plots; da/dN is the crack growth rate per cycle and is plotted as a function of ΔK ($\Delta K = K_{max} - K_{min}$). K , the stress intensity factor, is defined as follow:

$$K = \beta \cdot \sigma \sqrt{\pi a} \quad 3.10$$

Where:

- β is a dimensionless parameter depending on geometry loading conditions;
- σ is the stress that can be associated to σ_{max} or σ_{min} ;
- a is the crack length.

In Figure 3.29 a typical da/dN - ΔK plot is depicted; there different regions can be pointed out:

- region *I*: where a threshold value ΔK_{th} is defined below which there is no crack propagation or very slow crack growth;
- region *II*: where there is a linear relation between crack growth and ΔK and Paris law can be applied: $da/dN = C \cdot \Delta K^m$;
- region *III*: where crack growth increases rapidly to a limit value of ΔK where unstable propagation occurs, $K_{max} = K_C$.

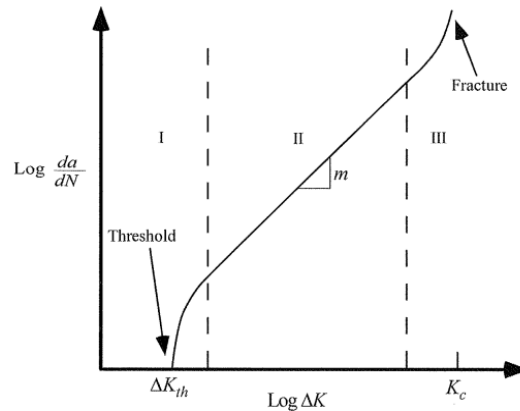


Figure 3.29. Typical crack growth rate as a function of ΔK for steels [69]

Specimens used for this test are C(T) specimen with W equal to 40mm. According to regulation from this dimension all other dimensions are obtained: a must be in a range between $0.2W$ and $0.975W$.

During the whole test the following relation must be satisfied:

$$(W - a) \geq \frac{\pi}{4} \cdot \left(\frac{K_{\max}}{\sigma_{ys}} \right)^2 \quad 3.11$$

Crack propagation tests were carried out by varying test temperature and load frequency. All tests were carried out accordingly to International standard ASTM [70]. Tests were carried out in load control; it means that load applied by the machine to the specimen is a sinusoidal wave shaped with σ_{min} and σ_{max} ratio equal to $R=0.1$. Measurements of crack growth were made through the compliance method. Precracking of the specimen was performed using $F_{\max}=6800N$ and $F_{\min}=680N$. Clip on gage was used to measure the crack opening.

3.6.1 Fatigue test results: F22 steel

On F22 steels crack propagation tests were carried out for charged and uncharged specimens by varying temperature and frequency [71][72], using MTS 810 machine and the environmental chamber. From other works it is well-known that hydrogen embrittlement is very dependent on frequency [20][73] even if, the combined effect of frequency and temperature, is never thoroughly investigated. In Table 3.11 the crack propagation test-plan is depicted with the parameters considered as variable in the tests.

Table 3.11. Crack propagation test plan for F22 specimens.

Uncharged specimen		Charged specimen	
T [°C]	f [Hz]	T [°C]	f [Hz]
RT, -60, -100	20	RT, -30	1, 10

Figure 3.30 shows results from fatigue crack propagation tests of uncharged specimens. It should be immediately noticed that, for uncharged specimens, the effect of temperature on the crack growth rate is not significant; the curves are very similar, with the same slope and slightly differing in the y-intercept. Propagation tests on uncharged specimens were carried out at a load frequency equal to $f=20\text{Hz}$. In normal environment conditions, as widely shown in literature, frequency is not a parameter that affecting the crack growth rate.

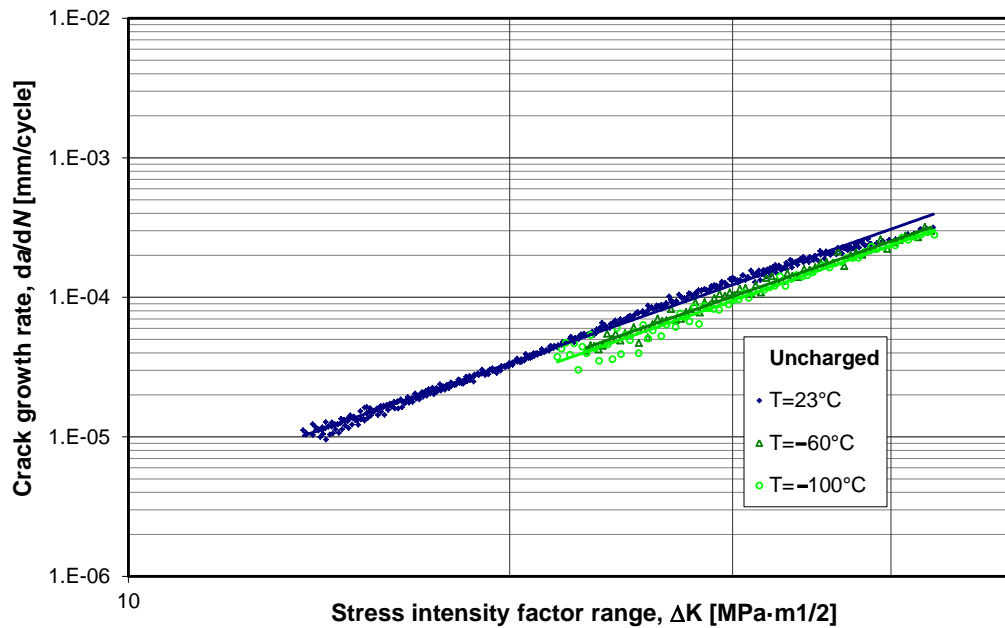


Figure 3.30. F22 steel: crack growth rate for uncharged specimens at different temperatures

Paris coefficients have been calculated and are shown below:

$$\left(\frac{da}{dN}\right)_{T=23^{\circ}\text{C}}^{\text{NoH}} = 2.3 \cdot 10^{-9} \Delta K^{3.191}$$

$$\left(\frac{da}{dN}\right)_{T=-60^{\circ}\text{C}}^{\text{NoH}} = 2.1 \cdot 10^{-9} \Delta K^{3.167}$$

$$\left(\frac{da}{dN}\right)_{T=-100^{\circ}\text{C}}^{\text{NoH}} = 1.9 \cdot 10^{-9} \Delta K^{3.174}$$

It should be pointed out that variations between crack growth rates, at different temperatures, are very small and that crack growth rates at same ΔK , decrease while decreasing temperature, as expected. Indeed, cyclic plastic zone is reduced while decreasing temperature due to the contemporary increase of yield strength.

Figure 3.31 shows results from fatigue crack propagation tests on H-charged C(T) specimens, at room temperature; two frequencies test were taken: $f=1\text{Hz}$ and $f=10\text{Hz}$. In the Figure the uncharged specimens curve is shown in order to compare the different behaviours.

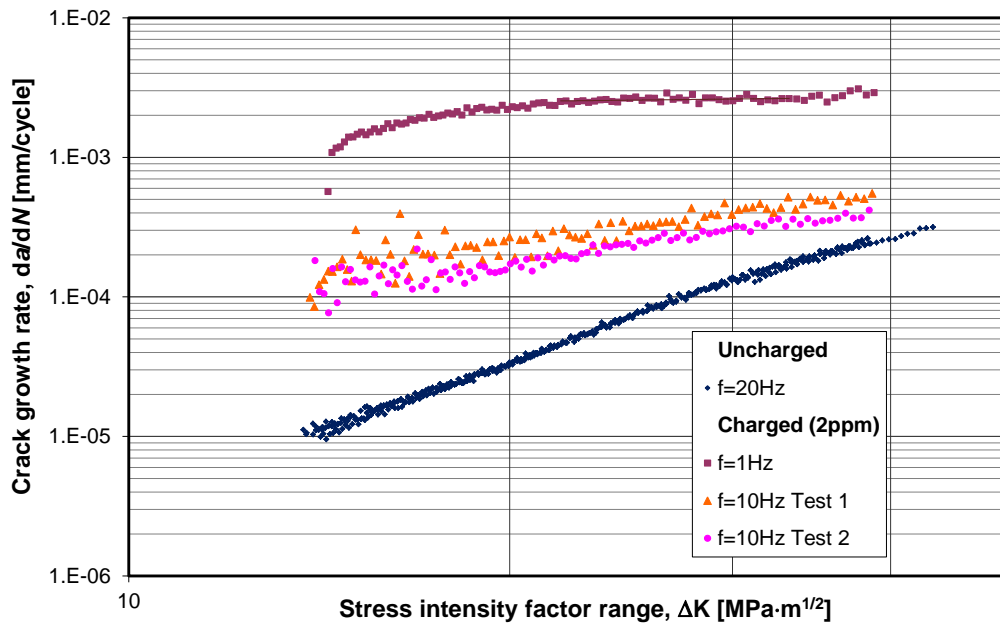


Figure 3.31. F22 steel: crack propagation rates, by varying the frequency at room temperature

The blue line indicates the test carried out at room temperature on uncharged F22 specimen; it can be noted that there is a perfect connection between Paris theory and experimental data. A linear and constant trend of the crack growth rate in the whole ΔK range is observed, too. On the other hand, for hydrogen charged specimen tested at $f=10\text{Hz}$ (orange and pink marks), a general increase in crack growth rate was observed at similar ΔK . In particular, at low ΔK , embrittlement effect is clearly significant because of the high amount of hydrogen atoms reaching the crack tip. At higher values of ΔK , propagation rate becomes similar to the values of uncharged specimens. This phenomenon can be interpreted as it follows: crack growth rate is the result of a sum of two contributions (hydrogen effect and load effect), at low ΔK hydrogen effect is predominant, while for higher values of ΔK mechanical propagation, due to high loads, becomes predominant. In the last case, the fatigue behaviour is mainly controlled by the mechanical properties of the material (as if it is hydrogen free) since there is not enough time for hydrogen to reach the crack tip because of the high crack growth rate.

Again, by observing Figure 3.31, the curve of hydrogen charged specimen at $f=1\text{Hz}$ and room temperature shows a strong enhancement of the embrittling effect of almost two orders of magnitude when compared to the uncharged specimen.

This can be explained by the fact that the crack tip spends longer time at maximum load since, hydrostatic stress segregates hydrogen. It was observed that crack growth is somehow independent from load condition ΔK since it propagates at a constant rate.

As a matter of fact, ΔK is not that influential since embrittlement effect occurs at a constant and remarkable growth rate. Figure 3.32 shows, test results of charged specimens, tested at $T=-30^{\circ}\text{C}$, and at $f=1\text{Hz}$ and $f=10\text{Hz}$.

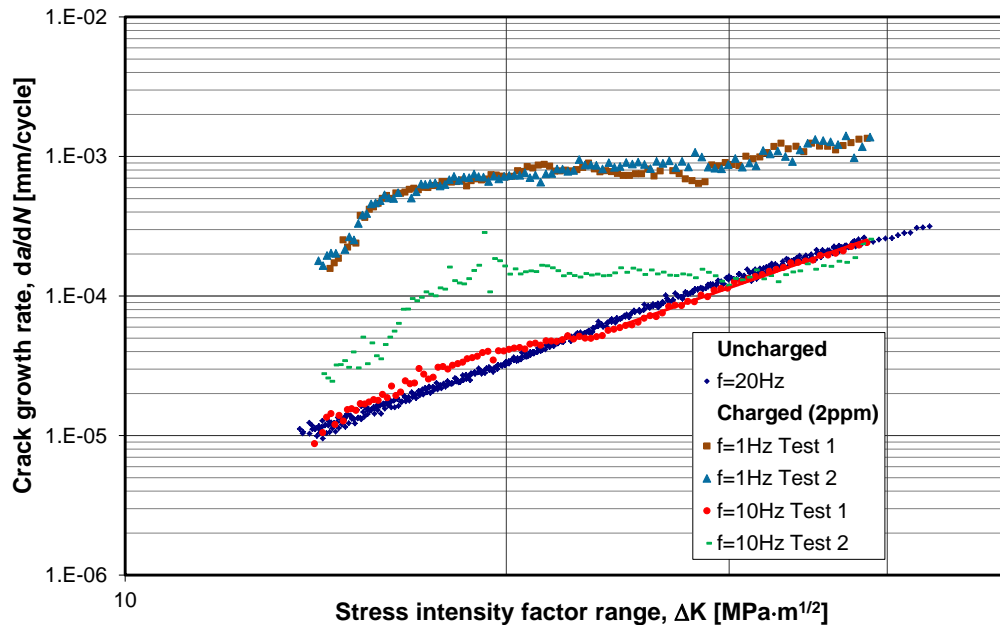


Figure 3.32. F22 steel: crack propagation rates, by varying the frequency at $T=-30^{\circ}\text{C}$

Also at this test temperature, it was observed a horizontal trend for the charged specimens, nevertheless it was noted a smaller embrittling effect of the hydrogen; for analogous frequencies, owing to low temperature, there is a slowdown of hydrogen diffusion at the crack tip.

Especially at high ΔK values, for tests carried out at $T=-30^{\circ}\text{C}$ and $f=10\text{Hz}$ on charged specimens, it was observed that the crack growth rate approaches the uncharged curve.

This fact shows that hydrogen influence on crack growth rate is reduced compared to tests carried out at $T=23^{\circ}\text{C}$. Figure 3.33 shows all results on F22 specimens together in order to give a better display of the trends and dependence of hydrogen embrittlement on frequency and temperature.

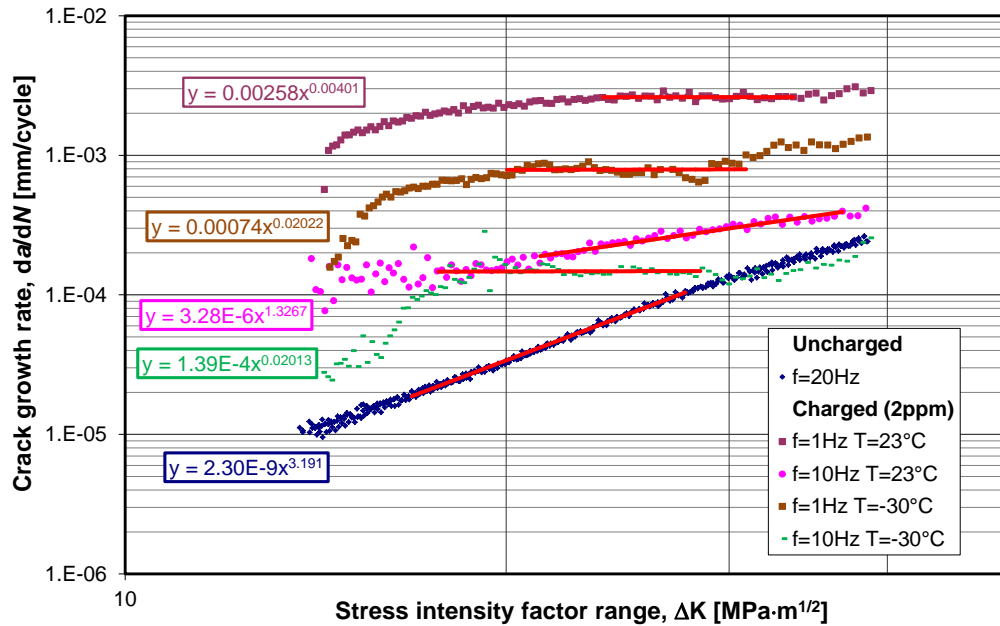


Figure 3.33. F22 steel: fatigue crack propagation test results on charged and uncharged specimens at different temperatures and frequencies

Crack growth coefficients are given below; it can be noted that, for charged materials, Paris coefficients are not those typical of steels:

$$\left(\frac{da}{dN}\right)_{T=23^{\circ}C}^{NoH} = 2.30 \cdot 10^{-9} \Delta K^{3.1910}$$

$$\left(\frac{da}{dN}\right)_{T=23^{\circ}C, f=1Hz}^H = 2.58 \cdot 10^{-3} \Delta K^{0.0040}, \quad \left(\frac{da}{dN}\right)_{T=23^{\circ}C, f=10Hz}^H = 3.28 \cdot 10^{-6} \Delta K^{1.3267}$$

$$\left(\frac{da}{dN}\right)_{T=-30^{\circ}C, f=1Hz}^H = 7.40 \cdot 10^{-4} \Delta K^{0.0202}, \quad \left(\frac{da}{dN}\right)_{T=-30^{\circ}C, f=10Hz}^H = 1.39 \cdot 10^{-4} \Delta K^{0.0201}$$

Differences of these values are clearly noticeable by comparing test results at different temperatures. It was also observed a good reproducibility of the results. It can be noted that, in charged specimens, m exponent tends to zero. This fact means that crack growth rate reaches a plateau and at the same time, since it is not completely equal to zero, there is still a mechanical contribution.

In Figure 3.34 crack length as a function of cycles number is shown.

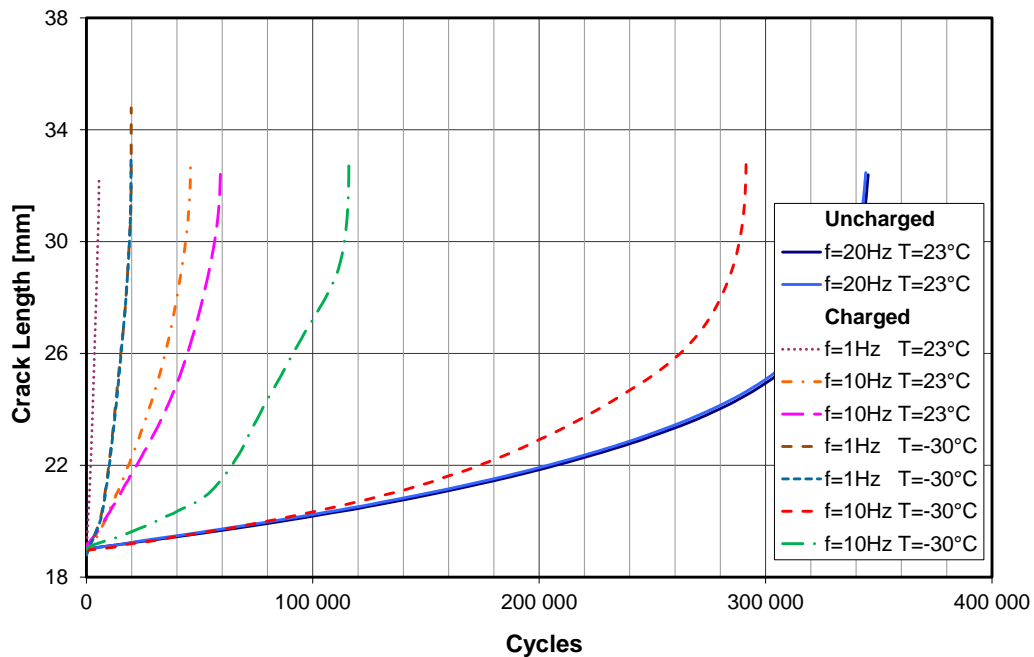


Figure 3.34. F22 steel: crack length as a function of number of cycles

It is evident the change of propagation rate when hydrogen is present; by looking at the number of cycles to failure, it can be noted that, for a hydrogen charged specimen tested at room temperature and $f=1\text{Hz}$, this value is equal to 5,500 cycle; while, for a hydrogen free specimen this value is equal to 340,000 cycles. This fact means that crack growth rate is 60 times faster in the hydrogen charged specimen. To better show the hydrogen effect on fatigue crack growth, Figure 3.35 shows the ratio between propagation rate in charged da/dN_H and uncharged da/dN_{NoH} specimens as a function of frequencies at similar ΔK and at $T=23^\circ\text{C}$.

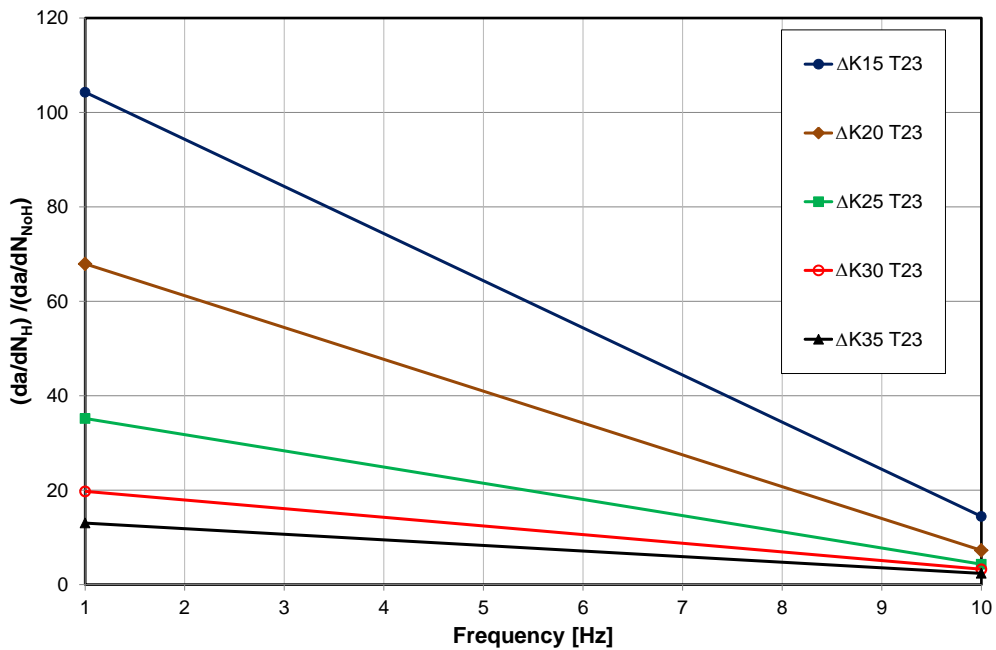


Figure 3.35. F22 steel: $(da/dN_H)/(da/dN_{NoH})$ ratio as a function of load frequency at $T=23^\circ\text{C}$

Crack growth rate variation, in low frequency tests, is large for low values of ΔK and decrease while increasing ΔK , when the crack propagation curve of the uncharged material reaches values close to the curve of the hydrogen charged material. After this value the curves are similar. When frequencies are higher, a decrease in crack growth rates ratio was observed; this is due to the fact that hydrogen has less time available to reach the crack tip. Figure 3.36 shows propagation rates ratio as a function of frequency for tests carried out at $T=-30^\circ\text{C}$.

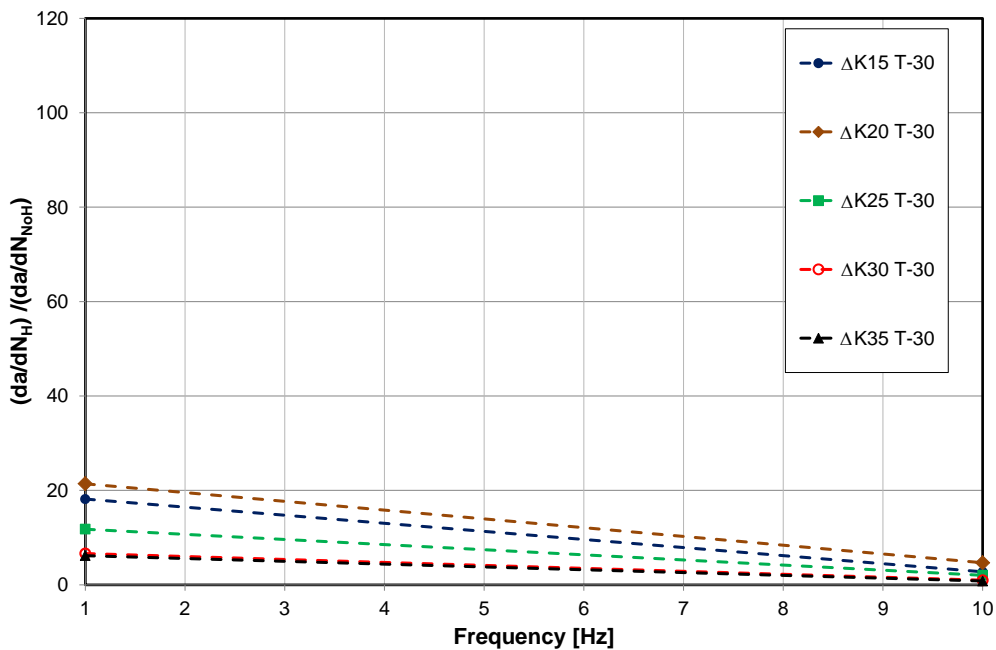


Figure 3.36. F22 steel: $(da/dN_H)/(da/dN_{NoH})$ ratio as a function of load frequency at $T=-30^\circ\text{C}$

At lower temperature, $(da/dN_H)/(da/dN_{NoH})$ ratio is smaller, meaning that hydrogen embrittling effect is mitigated. The explanation lies in the fact that, at lower temperature, hydrogen atoms take more time to diffuse at the crack tip. Moreover it was observed that the ratio at $\Delta K=15\text{MPa}\sqrt{\text{m}}$ is smaller than the ratio at $\Delta K=20\text{MPa}\sqrt{\text{m}}$ because in this case propagation is still dependent on fracture mechanisms connected to the applied loads.

In Figure 3.37 the influence of temperature on $(da/dN_H)/(da/dN_{NoH})$ ratio is shown, for both tested temperatures: $T=23^\circ\text{C}$ and $T=-30^\circ\text{C}$.

If taking the worst condition, that occurs at room temperature with a load frequency $f=1\text{Hz}$ and at low ΔK values, around $15\text{MPa}\sqrt{\text{m}}$, crack propagation rate, in hydrogen charged material, is 100 times higher than the one obtained by uncharged specimens.

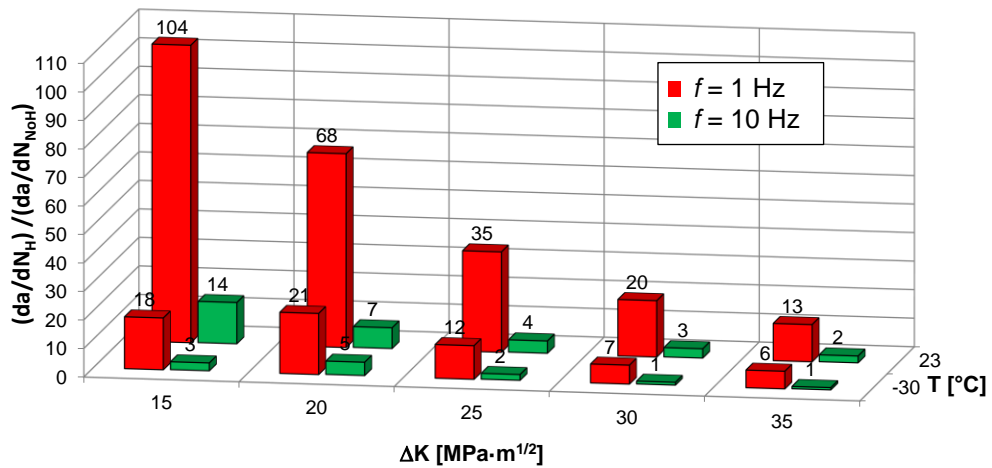


Figure 3.37. F22 steel: $(da/dN_H)/(da/dN_{NoH})$ ratio as a function of frequency at different temperature

The reduction in crack growth rate at different temperatures can be directly compared with the reduction of the diffusion coefficient from $T=23^\circ\text{C}$ to $T=-30^\circ\text{C}$. The diffusion coefficient, in solids, at different temperatures is often found to be well predicted by the following relation:

$$D = D^0 \cdot e^{\frac{-E_a}{RT}} \left[\frac{m^2}{s} \right]$$

Where:

- D_0 = pre-exponential factor = $0.88 \cdot 10^{-8} [m^2 / s]$
- E_a = activation energy = $15.5 \cdot 10^3 [J / mol]$
- R = gas constant = $8.314472 [J / (mol \cdot K)]$
- T = temperature $[K]$

The diffusion coefficients have been calculated equal to:

$$D_{23^{\circ}\text{C}} = 1.62 \cdot 10^{-11} \text{ [m}^2 / \text{s]} \quad D_{-30^{\circ}\text{C}} = 4.1 \cdot 10^{-12} \text{ [m}^2 / \text{s]}$$

The ratio is:

$$\frac{D_{23^{\circ}\text{C}}}{D_{-30^{\circ}\text{C}}} = \frac{1.62 \cdot 10^{-11}}{4.1 \cdot 10^{-12}} = 3.96$$

A comparison can be made with the crack growth rate ratios at T=23°C and T=-30°C at similar ΔK . Those values are reported below.

$f=1\text{Hz}$	$f=10\text{Hz}$
$\left(\frac{da / dN_{H_{-23^{\circ}\text{C}}_{-1\text{Hz}}}}{da / dN_{H_{-30^{\circ}\text{C}}_{-1\text{Hz}}}} \right)_{\Delta K=15\text{MPa}\cdot\text{m}^{1/2}} = 5.74$	$\left(\frac{da / dN_{H_{-23^{\circ}\text{C}}_{-10\text{Hz}}}}{da / dN_{H_{-30^{\circ}\text{C}}_{-10\text{Hz}}}} \right)_{\Delta K=15\text{MPa}\cdot\text{m}^{1/2}} = 5.24$
$\left(\frac{da / dN_{H_{-23^{\circ}\text{C}}_{-1\text{Hz}}}}{da / dN_{H_{-30^{\circ}\text{C}}_{-1\text{Hz}}}} \right)_{\Delta K=20\text{MPa}\cdot\text{m}^{1/2}} = 3.17$	$\left(\frac{da / dN_{H_{-23^{\circ}\text{C}}_{-10\text{Hz}}}}{da / dN_{H_{-30^{\circ}\text{C}}_{-10\text{Hz}}}} \right)_{\Delta K=20\text{MPa}\cdot\text{m}^{1/2}} = 1.56$
$\left(\frac{da / dN_{H_{-23^{\circ}\text{C}}_{-1\text{Hz}}}}{da / dN_{H_{-30^{\circ}\text{C}}_{-1\text{Hz}}}} \right)_{\Delta K=25\text{MPa}\cdot\text{m}^{1/2}} = 2.98$	$\left(\frac{da / dN_{H_{-23^{\circ}\text{C}}_{-10\text{Hz}}}}{da / dN_{H_{-30^{\circ}\text{C}}_{-10\text{Hz}}}} \right)_{\Delta K=25\text{MPa}\cdot\text{m}^{1/2}} = 2.13$
$\left(\frac{da / dN_{H_{-23^{\circ}\text{C}}_{-1\text{Hz}}}}{da / dN_{H_{-30^{\circ}\text{C}}_{-1\text{Hz}}}} \right)_{\Delta K=30\text{MPa}\cdot\text{m}^{1/2}} = 2.98$	$\left(\frac{da / dN_{H_{-23^{\circ}\text{C}}_{-10\text{Hz}}}}{da / dN_{H_{-30^{\circ}\text{C}}_{-10\text{Hz}}}} \right)_{\Delta K=30\text{MPa}\cdot\text{m}^{1/2}} = 3.33$
$\left(\frac{da / dN_{H_{-23^{\circ}\text{C}}_{-1\text{Hz}}}}{da / dN_{H_{-30^{\circ}\text{C}}_{-1\text{Hz}}}} \right)_{\Delta K=35\text{MPa}\cdot\text{m}^{1/2}} = 2.11$	$\left(\frac{da / dN_{H_{-23^{\circ}\text{C}}_{-10\text{Hz}}}}{da / dN_{H_{-30^{\circ}\text{C}}_{-10\text{Hz}}}} \right)_{\Delta K=35\text{MPa}\cdot\text{m}^{1/2}} = 3.01$

Crack growth rate ratios and diffusion coefficients ratio are very similar almost to say that the variation of diffusion coefficient, due to the temperature change, is one of the main responsible of the change in crack growth rate.

3.6.2 Fatigue test results: X65 steel

Crack propagation tests, similar to the previous case were carried out by means of X65 specimens, by varying temperature and frequency.

Table 3.12 shows crack propagation test-plan and test parameters.

Table 3.12. Crack propagation test plan for X65 specimens.

Uncharged specimen		Charged specimen	
T [°C]	f [Hz]	T [°C]	f [Hz]
RT	10, 20	RT, -30	1, 10

On uncharged specimens crack growth tests were performed at two different frequencies: $f=20\text{Hz}$ and $f=10\text{Hz}$. Curves are almost identical, as depicted in Figure 3.38. Crack propagation rate vs. ΔK is interpolated by two lines with different slopes (named step): Paris coefficient m , that indicates the acceleration of the crack growth rate, is higher in the first part and equal to 4.4, when an expected value for steels is equal to 3, and a lower one in the second part, where a reduction in crack growth rate was observed since m is equal to 2.2. ΔK_{step} is about at $25.5\text{MPa}\sqrt{\text{m}}$; the curves coefficients are equal to:

$$\left(\frac{da}{dN}\right)_{I, T=23^{\circ}\text{C}}^{NoH} = 1.01 \cdot 10^{-10} \Delta K^{4.3748}$$

$$\left(\frac{da}{dN}\right)_{II, T=23^{\circ}\text{C}}^{NoH} = 1.04 \cdot 10^{-7} \Delta K^{2.2231}$$

According to literature [74], variation in Paris exponents can be attributed to microstructural properties and in particular to microstructure dimension. Even though the phenomenon observed is typical of aluminium and titanium alloys, it was found also on steels. It is controlled by the size of the cyclic plastic zone, indeed, when it reaches a certain length, comparable with around few grain diameters, dislocations are constrained by different mechanism since new slip planes are activated and grain boundaries take part to the process. For this reason, there is a reduction of Paris exponent, which means an increased strength of the material and a higher constrain to dislocation movements; that is what was experimentally observed in X65 steel. This behaviour is shown in Figure 3.39, where different metals are depicted, in $da/dN-\Delta K$ plots.

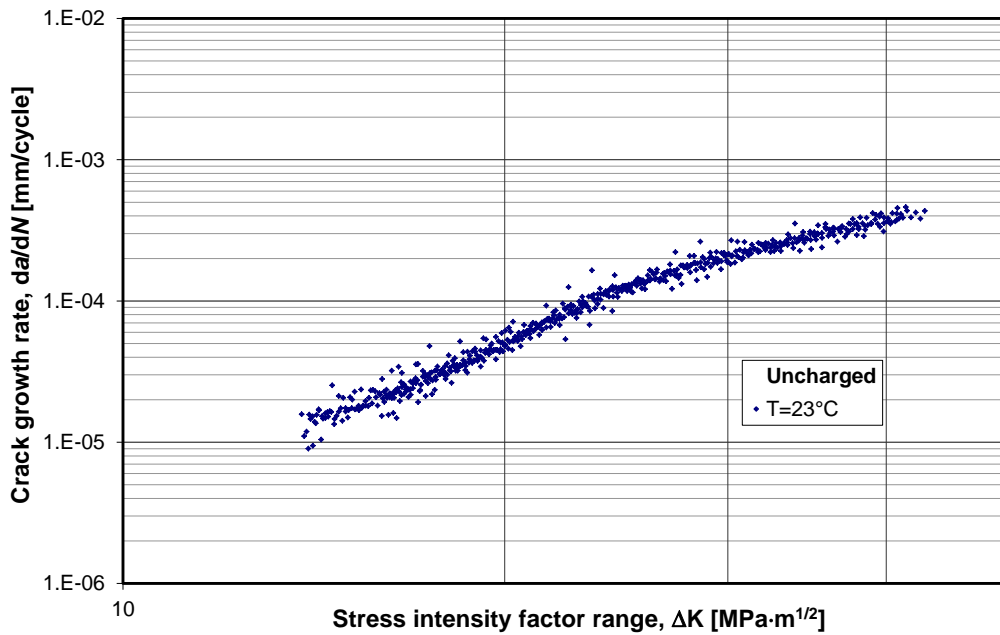


Figure 3.38. X65 steel: crack propagation rates, by varying the frequency at room temperature

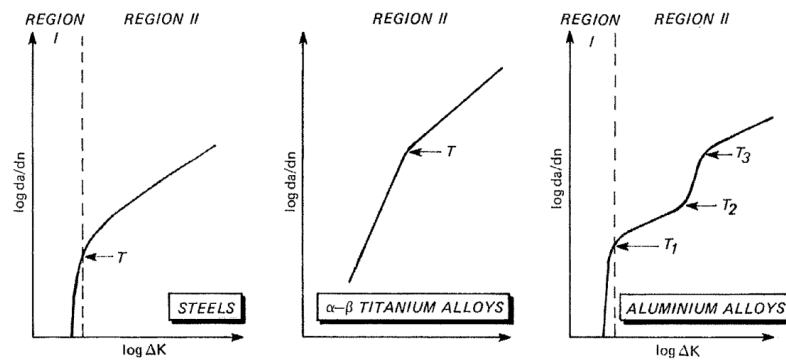


Figure 3.39. Schematization of the effect of cyclic plastic zone size on the fatigue crack growth rate curve:
T is the transitions, influenced by the relation between cyclic plastic zone size and microstructure

In Figure 3.40 results from fatigue crack growth tests, on charged specimens at room temperature, are shown; two frequencies test were investigated: $f=1\text{Hz}$ and $f=10\text{Hz}$. Test frequencies were taken similarly to F22 tests.

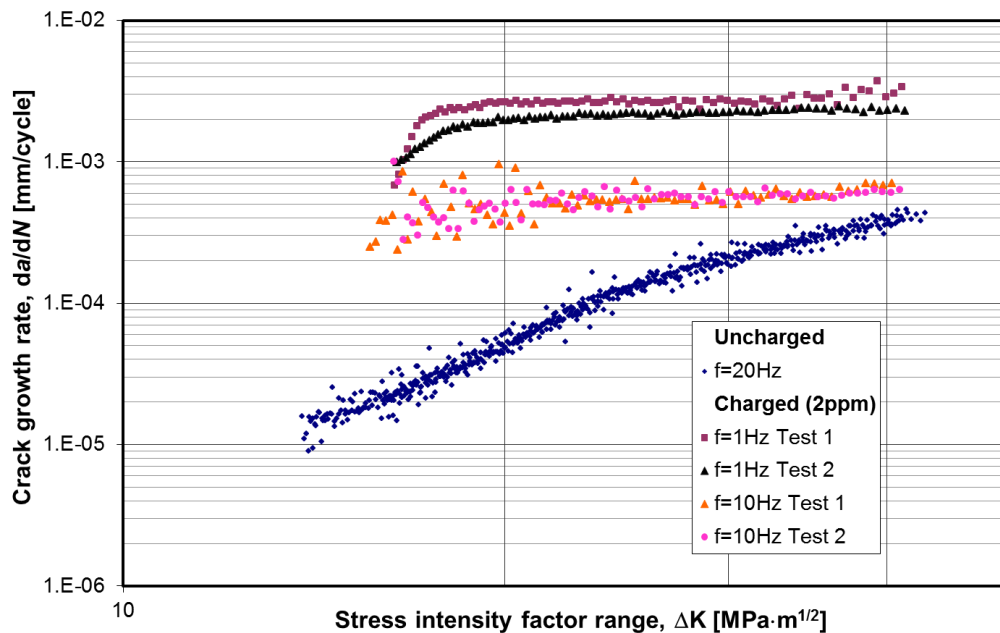


Figure 3.40. X65 steel: crack propagation rates, by varying the frequency at room temperature

Hydrogen effect causes an embrittlement and a crack growth acceleration comparable with the one observed during F22 testing. Plateau regions are easily noticeable for both test frequencies, $f=1\text{Hz}$ and $f=10\text{Hz}$; also, as stated above, crack growth rate reaches a constant value independent from crack length and load level, since it is independent from ΔK . Figure 3.41 shows results for specimens tested at $T=-30^\circ\text{C}$ and similar frequencies. Also at this test temperature, it was observed a horizontal trend for the charged specimens; nevertheless, it was noticed a smaller embrittling effect by the hydrogen presence; for analogous frequencies. This fact can be explained with thermal considerations: at lower temperatures, there is a slowdown of hydrogen diffusion reaching the FPZ (fracture process zone). Especially at high ΔK values, for tests carried out at $T=-30^\circ\text{C}$ and $f=10\text{Hz}$ on charged specimens, it was observed that the crack growth rate approaches the uncharged curve. This fact shows that hydrogen influence on crack growth rate is reduced compared to tests carried out at $T=23^\circ\text{C}$.

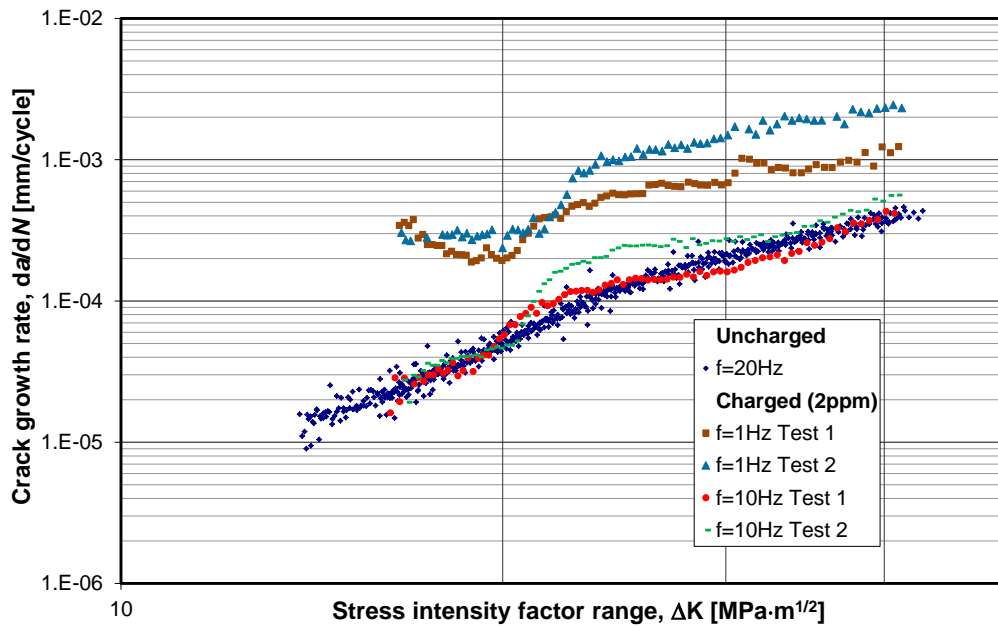


Figure 3.41. X65 steel: crack propagation rates, by varying the frequency at $T=-30^{\circ}\text{C}$

In this case, temperature plays a very important role in hydrogen embrittling effect; indeed, hydrogen diffusivity inside the lattice decreases and $da/dN-\Delta K$ curves approaches the uncharged material behaviour. As it can be noted, in the same ΔK range of where at room temperature there is a plateau, the curve at $T=-30^{\circ}\text{C}$ present a positive slope.

Also, in the curve at $T=-30^{\circ}\text{C}$ and $f=1\text{Hz}$, it is well-noticeable how hydrogen embrittling effect has a maximum at medium ΔK range, while, for lower and higher values material behaviour is again similar to the uncharged one, that is the typical fatigue behaviour of the material without hydrogen. It means that, if hydrogen embrittlement assisted cracking on crack growth were not taken into account, the most surprising and catastrophic damages can occur at medium ΔK range, since in this range deviation from ordinary behaviour is maximum.

In Figure 3.42 all results regarding X65 are depicted in order to give a better display of the trends and the dependence of hydrogen embrittlement on frequency and temperature.

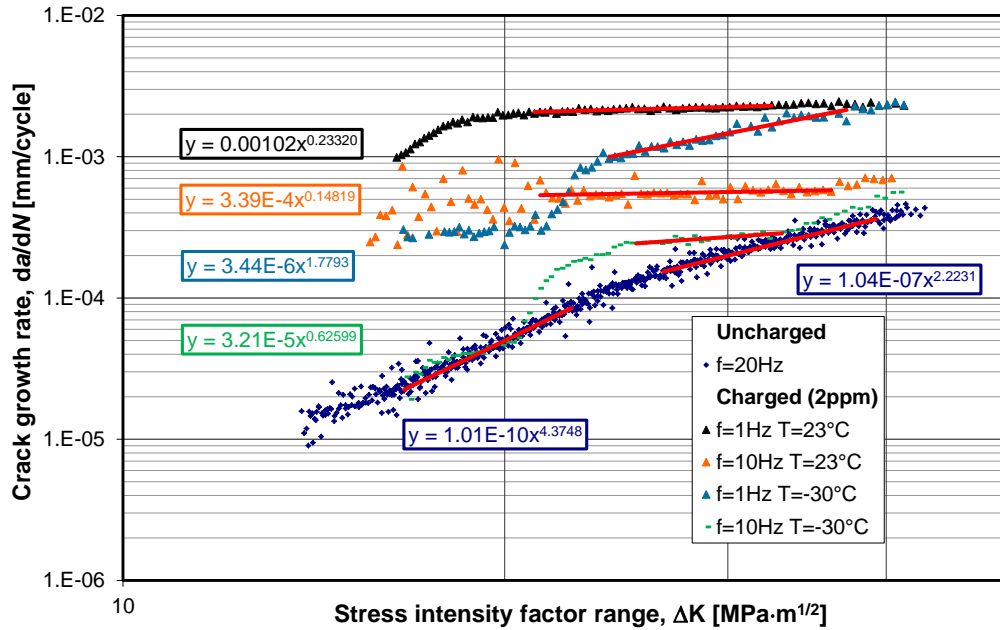


Figure 3.42. X65 steel: fatigue crack propagation test results on charged and uncharged specimens at different temperatures and frequencies

Crack propagation equations and coefficients of the X65 curves are given below:

$$\left(\frac{da}{dN}\right)_{I, T=23^{\circ}C}^{NoH} = 1.01 \cdot 10^{-10} \Delta K^{4.3748}, \quad \left(\frac{da}{dN}\right)_{II, T=23^{\circ}C}^{NoH} = 1.04 \cdot 10^{-7} \Delta K^{2.2231}$$

$$\left(\frac{da}{dN}\right)_{T=23^{\circ}C, f=1Hz}^H = 1.02 \cdot 10^{-3} \Delta K^{0.2332}, \quad \left(\frac{da}{dN}\right)_{T=23^{\circ}C, f=10Hz}^H = 3.39 \cdot 10^{-4} \Delta K^{0.1482}$$

$$\left(\frac{da}{dN}\right)_{T=-30^{\circ}C, f=1Hz}^H = 3.44 \cdot 10^{-6} \Delta K^{1.7793}, \quad \left(\frac{da}{dN}\right)_{T=-30^{\circ}C, f=10Hz}^H = 3.21 \cdot 10^{-5} \Delta K^{0.6260}$$

For hydrogen charged specimens, the calculation of Paris coefficients was done by considering the plateau region; as already discussed for F22, m coefficient approaches zero values at room temperature and low frequencies. In Figure 3.43 crack length as a function of cycles number is shown.

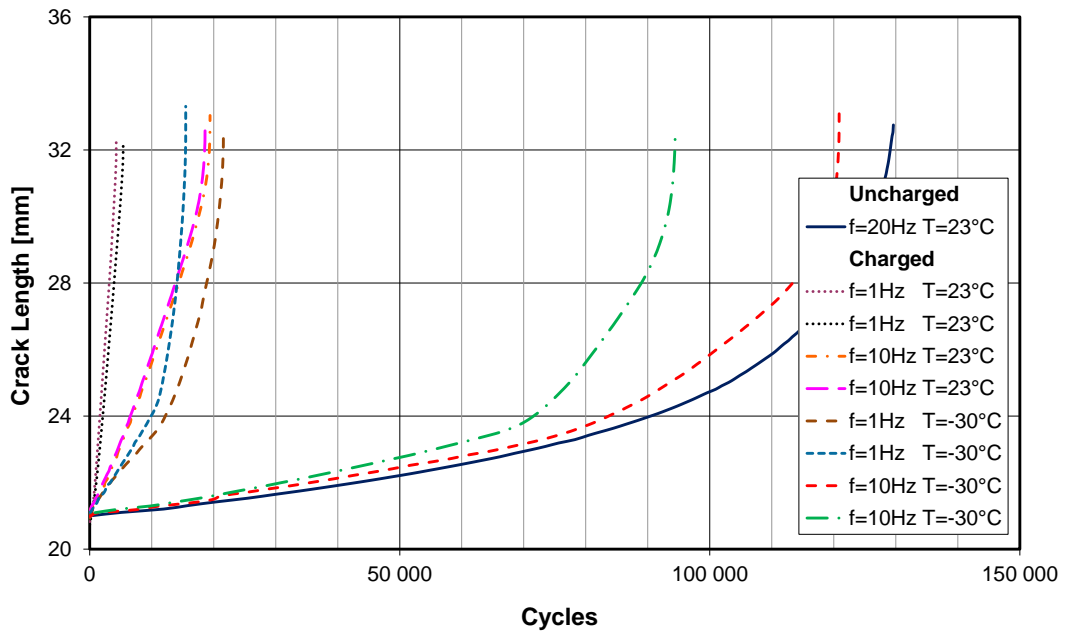


Figure 3.43. X65 steel: crack length as a function of number of cycles

As previously noted with F22 tests, when specimens are hydrogen charged, unstable propagation is reached 30 times faster than the uncharged case; the maximum enhancement is observed if comparing data for a hydrogen charged specimen at room temperature and $f=1\text{Hz}$ and the uncharged one.

As it will be shown later, maximum enhanced of hydrogen embrittlement appears at room temperature. In Figure 3.44 crack propagation rates ratios are shown; in particular ratios were calculated between charged specimens growth rate da/dN_H and uncharged specimen growth rate da/dN_{NoH} as a function of frequencies and ΔK at room temperature.

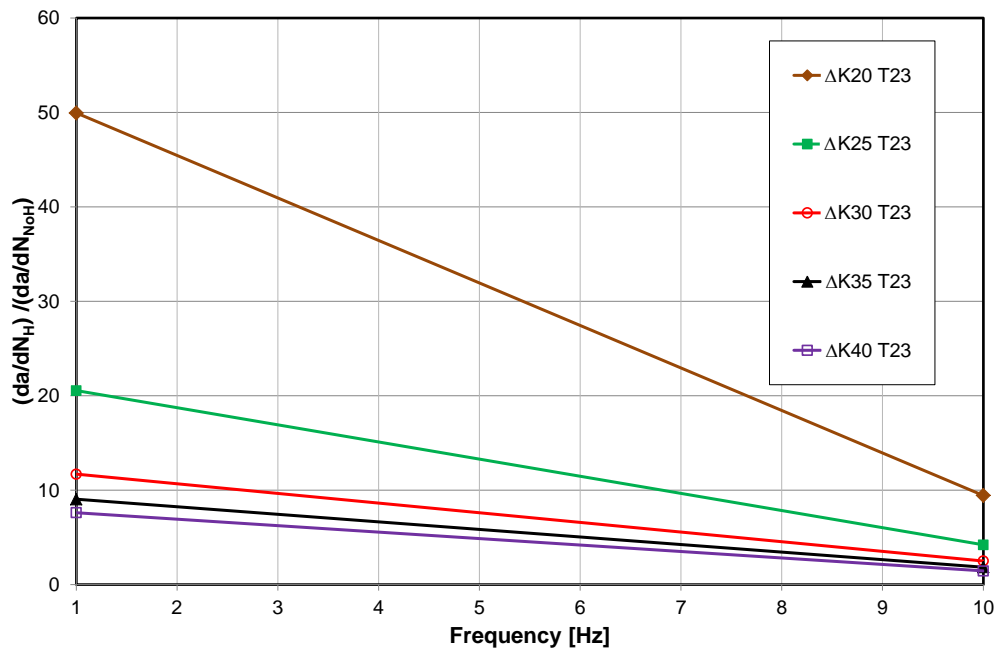


Figure 3.44: X65 steel: $(da/dN_H)/(da/dN_{NoH})$ ratio as a function of load frequency at $T=23^\circ\text{C}$

Results agree with those found for F22 steel; indeed, while increasing load frequency, hydrogen charged crack propagation rate goes closer to the uncharged material behaviour.

In Figure 3.45 same curves of those reported in Figure 3.44 are depicted, in this case test temperature is equal to $T=-30^\circ\text{C}$. Ratio scale was modified with respect to the previous graph for a better understanding of the results.

It was observed that, especially at low and high values of ΔK and precisely until $\Delta K=20\text{MPa}\sqrt{\text{m}}$ and after $\Delta K=30\text{MPa}\sqrt{\text{m}}$, and at high frequencies, crack propagation rates are very close to the uncharged behaviour. On the other hand, for values of ΔK in that range, there is a slight difference also at high frequencies. At low frequencies, it was noticed a rise of crack propagation rates ratio also for X65 steel, nevertheless this rise is not very high.

In Figure 3.46 the influence of temperature on $(da/dN_H)/(da/dN_{NoH})$ ratio is shown for both tested temperatures: $T=23^\circ\text{C}$ and $T=-30^\circ\text{C}$.

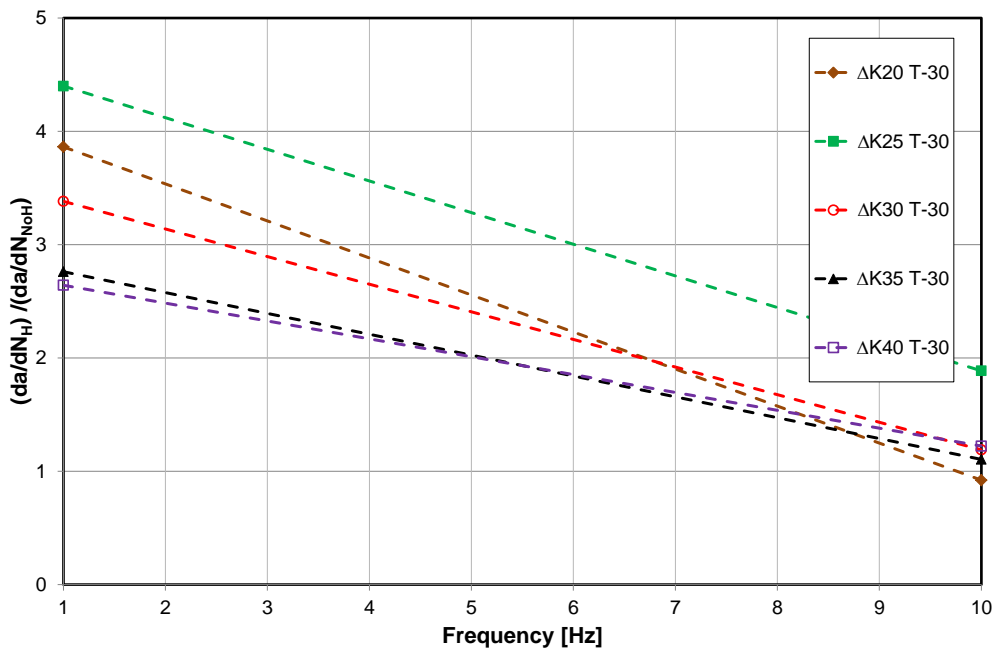


Figure 3.45: X65 steel: $(da/dN_H)/(da/dN_{NoH})$ ratio as a function of load frequency at $T=-30^{\circ}\text{C}$

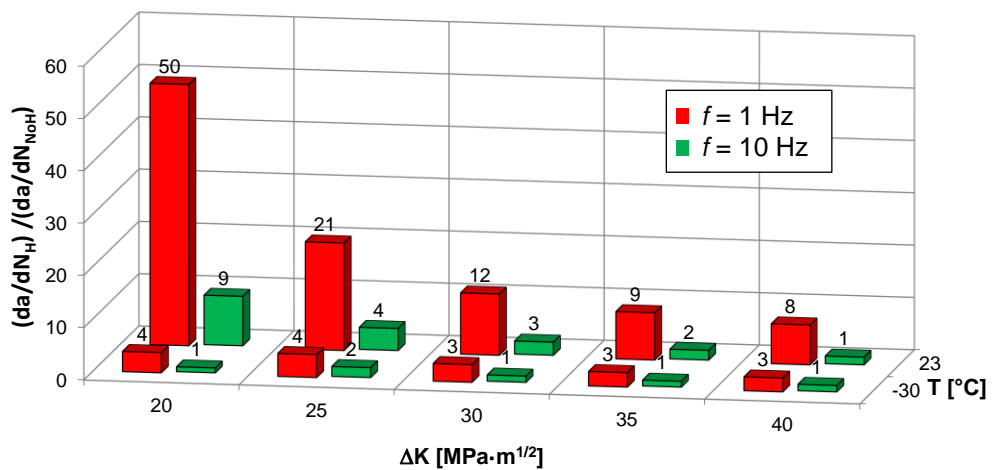


Figure 3.46: X65 steel: $(da/dN_H)/(da/dN_{NoH})$ ratio as a function of frequency at different temperature

Once again, pointing out the worst situation, that is for hydrogen charged specimen at room temperature, $f=1\text{Hz}$ and low ΔK , crack propagation rate is 50 times higher than the rate in the same condition for the uncharged specimen.

3.6.3 Remarks on results

A common feature that emerged from data is the presence of a transient and/or a large scatter of data at the beginning of the test until a certain, threshold, ΔK_{th} level. This threshold appears to be increased by frequency and decrease by increasing temperature. In particular this threshold seems lower for F22 steel (around $\Delta K=20\text{MPa}\sqrt{\text{m}}$, as it can be noted from Figure 3.33) and slightly higher for X65 steel (around $\Delta K=23\text{MPa}\sqrt{\text{m}}$, see Figure 3.42). After this transient, behaviour of the material seems more stable. It is difficult to assess quantitatively this transient since accurate tests need to be performed, nevertheless a better understanding will be provided in chapter 5 thanks to fractographic investigation and comparison with literature and theory shown in chapter 2. Another remark, that should be done, concerns the fact that specimens have been hydrogen precharged; in literature many of these tests are done under cathodic reaction (by varying the potential) of hydrogen so that results seem more like stress corrosion cracking (SCC) while in this work results are typical of HE of charged lattice.

4 Fatigue Crack Growth Predicting Model

4.1 Theory of the model

In this chapter, a model to predict the hydrogen embrittlement crack growth rate in the *II* region of the $da/dN-\Delta K$ plot is suggested. This model will predict the behaviour of the material as a function of the experimental parameters such as: test temperature, load frequency and ΔK . In particular, once the material behaviour without hydrogen and how hydrogen enhances embrittlement is known, it is possible to predict the crack growth rate and therefore the crack length after a certain number of cycles, at constant load, for a certain temperature and load frequency. This model is based on a superposition of effects: mechanical fatigue crack growth and purely hydrogen embrittled sustained growth, as given in [69] and revised in [75].

Fatigue crack growth in aggressive environments can be enhanced by sustained load during each load cycle. There are two main models which try to account for this effect:

- Superposition model, reported in [75] and given in Eq. 4.1;
- The process competition model, reported in [76].

The superposition model proposes that the overall crack growth rate is the sum of a baseline fatigue component (mechanical fatigue) and a component due to sustained load fracture (as in Figure 4.1). On the other hand, the process competition model assumes that fatigue and sustained load fracture are mutually competitive and that the crack will growth at the fastest available rate, whether that is the baseline fatigue crack growth rate or the crack growth rate per cycle owing to sustained load fracture. Superposition model is formulated as it follows:

$$\left(\frac{da}{dN}\right)_{TOT} = \left(\frac{da}{dN}\right)_B + \int \frac{da}{dt} K_I(t) dt \quad 4.1$$

B stands for baseline fatigue (mechanical fatigue) and the integral in Eq. 4.1 is taken over one cycle of the fatigue loading and incorporates the effect of frequency, f , and stress ratio, R , via $K_I(t)$.

In this experimental investigation, it was found, from SEM analysis (next chapter), that in the fracture surface, it can be spotted either the base mechanical fatigue (striations) and the sustained load fracture (facets and “cells” with inclusion inside). For this reason, superposition model was taken into account and applied.

4.1.1 Frequency and temperature dependence

The following derivation will be done for superposition model, for the reason already mentioned; since in this investigation stress ratio was not considered and significant parameters are temperature and frequency, it is possible to simplify the integral in Eq. 4.1 and give to it a physical meaning as it follows:

$$\int \frac{da}{dt} K_I(t) dt \cong \frac{d\bar{a}}{dt} \cdot \int dt = \frac{d\bar{a}}{dt} \cdot t = \left(\frac{d\bar{a}}{dt} \right)_{IHAC} \cdot \frac{1}{f} \quad \text{with} \quad \int \frac{da}{dt} K_I(t) \cong \left(\frac{d\bar{a}}{dt} \right)_{IHAC}$$

Where $\left(\frac{d\bar{a}}{dt} \right)_{IHAC}$ is the average sustained load fracture rate owing to internal hydrogen assisted cracking and, since the integral in Eq. 4.1 was calculated over one loading cycle, $t = 1/f$. Therefore, the superposition model, given in Eq. 4.1, can then be rearranged as it follows:

$$\left(\frac{da}{dN} \right)_{TOT} = \left(\frac{da}{dN} \right)_B + \frac{1}{f} \cdot \left(\frac{d\bar{a}}{dt} \right)_{IHAC} \quad 4.2$$

Hence, the superposition of both crack growth rates (*i.e.* baseline and IHAC) should give the frequency dependence of the overall crack propagation rate (TOT) once the behaviour in the II region of the uncharged material and the average sustained load fracture rate $\left(\frac{d\bar{a}}{dt} \right)_{IHAC}$ are known.

Figure 4.1 is a schematic of how the superposition model can be used to predict the overall crack growth rate curve for the materials in specific environmental and load conditions. It is also shown that there might be a K_{start} at which IHAC is null before and contributes after this level to crack growth; this behaviour was found also in tests data, nevertheless, accurate measurements need to be done in order to have a precise explanation of the phenomenon in a quantitative way; in the fractographic investigation this point will be better explained.

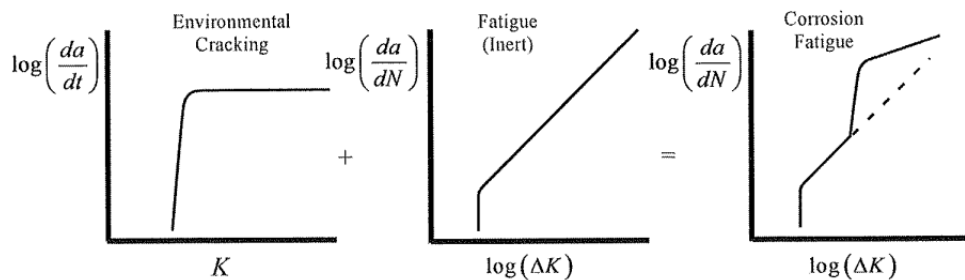


Figure 4.1. Superposition model

It can also be seen that the crack propagation due to hydrogen embrittlement is independent from ΔK in a certain range, between ΔK_{start} , where hydrogen presence starts to affect the material, and higher ΔK , where crack propagation is no longer dependent on

hydrogen embrittlement since mechanical growth is much higher and the material is approaching instability; this behaviour was found also in this analysis and that is the reason why it was possible to simplify the integral in Eq. 4.1. There are other models that calculate da/dt as a function of intrinsic parameters of the material such as elastic modulus, yield strength, strain hardening coefficient, diffusion coefficient, grain and inclusion size, hydrogen content and adjusting the value according to semi-empirical values. Nevertheless, these measurements take long time and still they cannot give an high accuracy; for these reasons it was chosen to measure the ratio, taking as reference a temperature $T=23^{\circ}\text{C}$; in this way all parameters that do not depend on temperature are cancelled and the diffusion coefficient is taken as index of the ratio between the growth rates [77]. It is then possible to write the following relation:

$$\frac{(d\bar{a}/dt)_{EAC}^{T=23^{\circ}\text{C}}}{(d\bar{a}/dt)_{EAC}^{T=-30^{\circ}\text{C}}} = \frac{D_{23^{\circ}\text{C}}}{D_{-30^{\circ}\text{C}}}$$

Crack growth rate is, in fact, a function of diffusion coefficient as shown in previous works [78] and depicted in Figure 4.2 where it is reported $\log(da/dt)$ versus temperature.

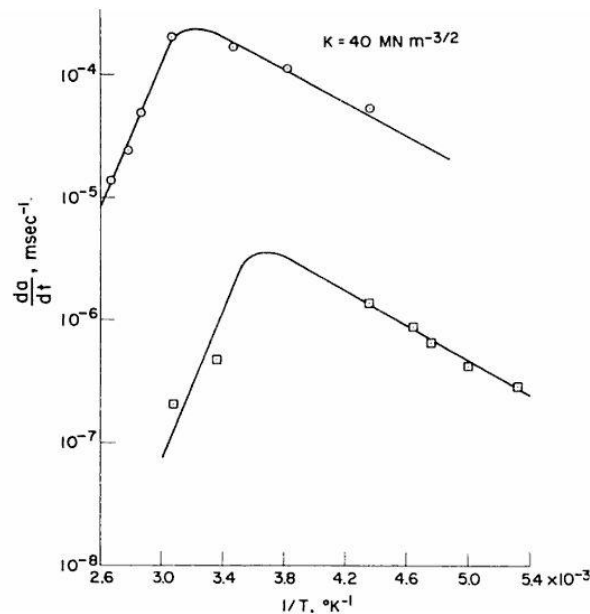


Figure 4.2. crack growth rate versus temperature in hydrogen gas for 4130 steel

4.2 Analytical procedure

For both steels, it was first pointed out the “Paris relation” of the uncharged material; it has been found that for F22 material constants are:

$$C = 2.3 \cdot 10^{-9} \text{ mm / cycle}$$

$$m = 3.1910$$

For X65, two different equations were used (see Chapter 3) and Paris coefficients are:

$$C_I = 1.01 \cdot 10^{-10} \text{ mm / cycle} \left. \begin{array}{l} \\ m_I = 4.3748 \end{array} \right\} \Delta K < 25.5 \text{ MPa}\sqrt{\text{m}}$$

$$C_{II} = 1.04 \cdot 10^{-7} \text{ mm / cycle} \left. \begin{array}{l} \\ m_{II} = 2.2231 \end{array} \right\} \Delta K > 25.5 \text{ MPa}\sqrt{\text{m}}$$

Then, the average crack growth rate per cycle owing to the hydrogen embrittlement was estimated. Calculations were done by taking as reference either $T=23^\circ\text{C}$ and $f=1\text{Hz}$ or the average of crack rates at different frequencies, using the following relation:

$$\left(\frac{d\bar{a}}{dt} \right)_{IHAC} = \left(\left(\frac{da}{dN} \right)_{TOT} - \left(\frac{da}{dN} \right)_B \right) \cdot f \quad 4.3$$

Analytically, determination of the average crack growth rate per cycle owing to the hydrogen embrittlement was found according to Eq. 4.3, by subtracting the data on the uncharged steel $(da/dN)_B$, that is Paris relation, to $(da/dN)_{TOT}$ of the charged specimen at the same ΔK in a range where still the IHAC effect is predominant (plateau region).

When crack propagation rate is much higher than the uncharged material the estimation can be performed by dividing the crack growth length and the elapsed time that this process takes in the plateau region. The reason why it was considered only this region is that in the plateau the hydrogen embrittlement contribution to crack growth is relevant compared to the uncharged case (almost 2 orders of magnitude).

Another parameter that should be estimated to a good fitting of the model is ΔK_{start} , that is the value of ΔK where crack propagation, in presence of hydrogen, begins to be influenced and increases.

$$(\Delta K)_{start} = K_I^{start} \cdot (1 - R) \quad 4.4$$

The superposition model doesn't consider the micromechanical mechanisms. Hydrogen embrittling acceleration occurs when a critical hydrogen concentration at the crack tip is reached. For this region the hydrogen diffusion and kinetics in FPZ (fracture process zone) and other variables (C_{cr} , C_0 , T , D , r_y , σ_H) should be taken into consideration. The experimental results show that ΔK_{start} is temperature and frequency dependent and the values are in the range of $12.5 \div 14.5 \text{ MPa}\sqrt{\text{m}}$. This behaviour and the values are considered in the model. Finally it can be assumed that the upper boundary of the model reaches asymptotically the critical K value of the material.

Since the model predicts a superposition of effect, and not a competition, there must be, and it was experimentally observed, a transient where hydrogen assisted cracking approaches the $(d\bar{a}/dt)_{EAC}$ rate in a range of ΔK from the threshold to the plateau value.

In order to avoid a step at ΔK_{start} , in the crack growth rate it can be choose to gradually introduce the effect of hydrogen embrittlement after this point; that corresponds to an interval of $2\text{MPa}\sqrt{\text{m}}$ in which the contribution of $(d\bar{a}/dt)_{EAC}$ is gradually introduced; the equation was then modified as it follows:

$$\left(\frac{da}{dN}\right)_{TOT} = \left(\frac{da}{dN}\right)_B + \frac{1}{f} \left(\frac{d\bar{a}}{dt}\right)_{IHAC} g(\Delta K) \quad 4.5$$

Where:

- $g(\Delta K)=0$ if $\Delta K < \Delta K_{start}$;
- $g(\Delta K)$ is a function of ΔK that goes from 0 to 1 when $\Delta K_{start} \leq (\Delta K) \leq \Delta K_{start}+2$
- $g(\Delta K)=1$ if $\Delta K > \Delta K_{start}+2$;

Temperature dependence was considered through the diffusion coefficients ratio knowing the values of diffusion coefficient at fixed temperature.

$$D = D_0 \cdot e^{\frac{-E_a}{RT}} \left[\frac{m^2}{s} \right] \quad 4.6$$

Since the ratio between diffusion coefficients cancel the influence of D_0 , the unique parameter that should be calculated is the activation energy for diffusion E_a , that can vary largely in the process zone owing to presence of high energy hydrogen traps such as dislocations, vacancies and the stress state itself, whose concentration is different than in the bulk material [79].

Activation energy for X65 and F22 steels was calculated from literature equal to 15.5kJ/mol , nevertheless this value can vary largely and depends on the site where the hydrogen is: low energy, when interstitial, ($E_a=1.6\text{kJ/mol}$) and high energy, when trapped, ($E_a=60\text{kJ/mol}$).

4.3 Results

4.3.1 Model for F22

For F22 steel average crack propagation rate owing to hydrogen assisted cracking is:

$$\left(\frac{d\bar{a}}{dt} \right)_{EAC}^{T=23^{\circ}C, f=1Hz} = 2.48 \cdot 10^{-3} \text{ mm} / \text{s}$$

Model results at $T=23^{\circ}C$ and at different frequencies are compared with test data as it can be seen from the overlapping in Figure 4.3.

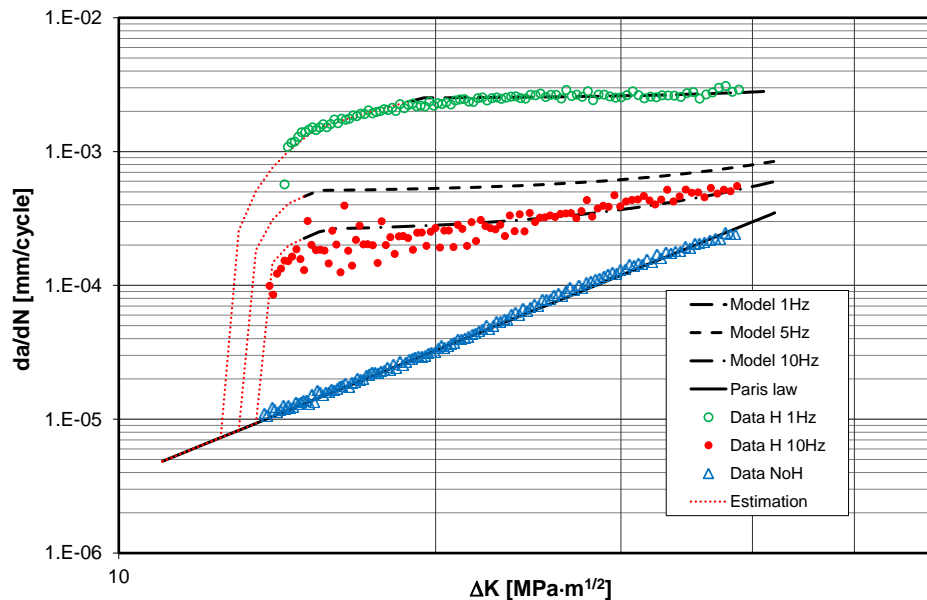


Figure 4.3. F22 steel: model prediction and experimental data at $T=23^{\circ}C$

Upper and lower limit values of ΔK were not experimentally determined but they are shown for a better understanding of the behaviour of the material tested in all the ΔK ranges.

As it can be seen, the model predicts effectively real material behaviour at $f=10Hz$ and, according to the theory, it is reliable in the tested range. Crack propagation rate at $T=-30^{\circ}C$ is:

$$\left(\frac{d\bar{a}}{dt} \right)_{EAC}^{T=-30^{\circ}C, f=1Hz} = 6.28 \cdot 10^{-4} \text{ mm} / \text{s}$$

Good agreement between test data and model prediction is found. From tests carried out at $T=-30^{\circ}\text{C}$, crack growth rate da/dt is equal to $8.98 \cdot 10^{-4} \text{ mm/s}$. The difference between the predicted and analytically calculated rate, equal to $6.28 \cdot 10^{-4} \text{ mm/s}$, is due to low accuracy of activation energy E_a evaluation; in fact, by reversing the model it is possible to estimate the activation energy by imposing a perfect fitting of the data; the result is equal to 11.5 kJ/mol , then smaller than the value taken from literature. Subsequently, it is possible to plot the crack propagation curves at $T=-30^{\circ}\text{C}$ through the model.

In Figure 4.4 the estimation is overlapped to the real data; also in this case model prediction is satisfactory.

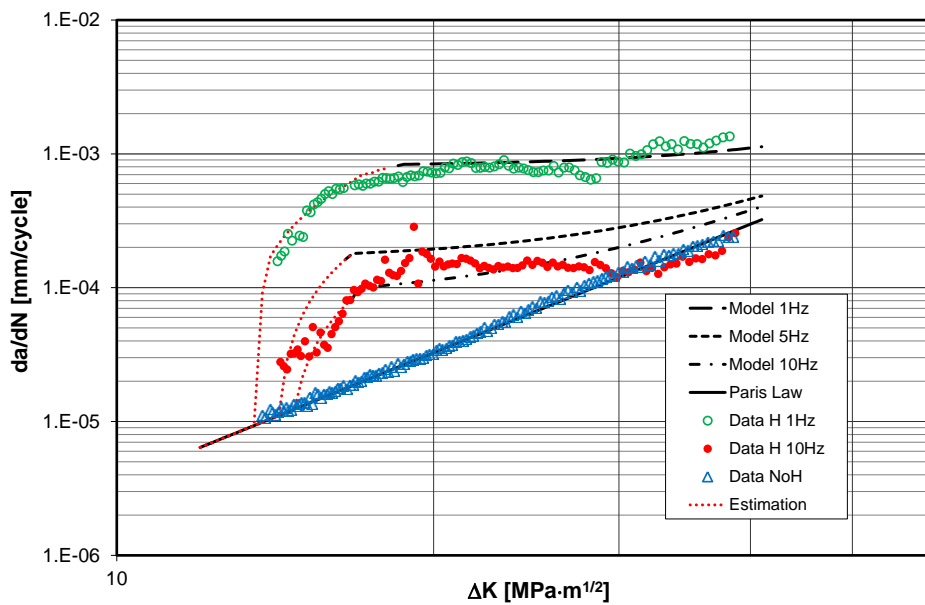


Figure 4.4. F22 steel: model prediction and experimental data at $T=-30^{\circ}\text{C}$

4.3.2 Model for X65

For X65 steel, crack propagation rate due to hydrogen effect is calculated and give the following value:

$$\left(\frac{d\bar{a}}{dt} \right)_{EAC}^{T=23^{\circ}\text{C}, f=1\text{Hz}} = 2.23 \cdot 10^{-3} \text{ mm / s}$$

Model prediction at $T=23^{\circ}\text{C}$ and different frequencies was compared with test data; in Figure 4.5 the superposition is shown.

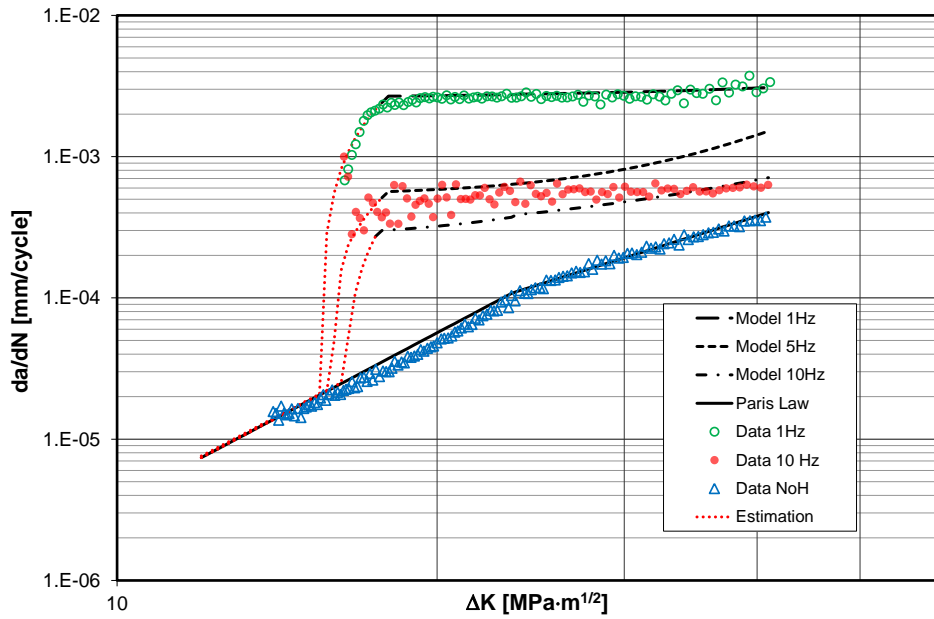


Figure 4.5. X65 steel: model prediction and experimental data at T=23°C

As it can be seen the model predicts effectively real material behaviour at $f=10\text{Hz}$ and, according to the theory, it is reliable in the tested range. Crack propagation rate at T=-30°C is:

$$\left(\frac{d\bar{a}}{dt} \right)_{EAC}^{T=-30^{\circ}\text{C}, f=1\text{Hz}} = 5.65 \cdot 10^{-4} \text{ mm / s}$$

Model prediction at T=-30°C and different frequencies was compared with test data; in Figure 4.6 the superposition is shown.

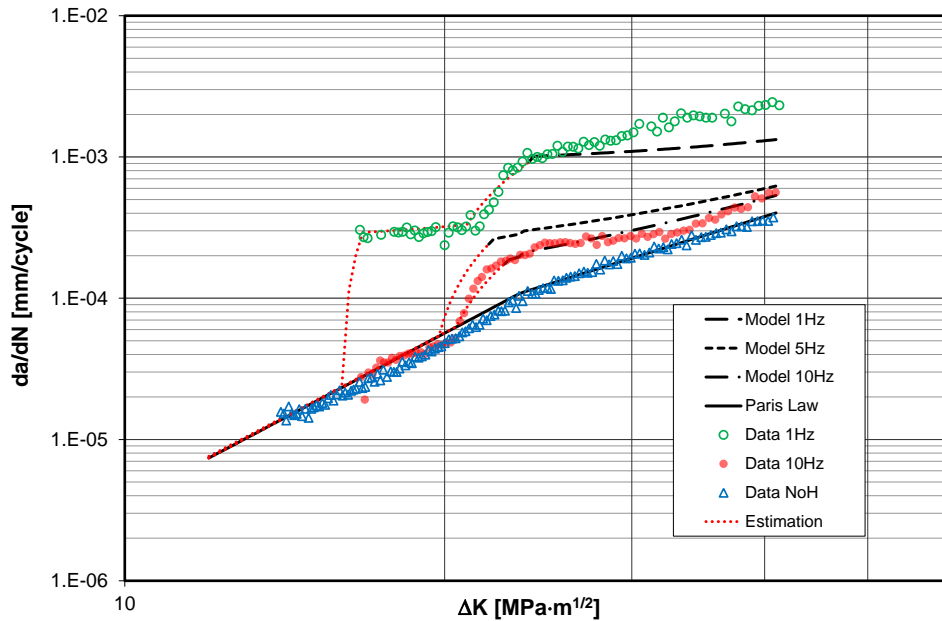


Figure 4.6. X65 steel: model prediction and experimental data at T=-30°C

4.4 Application of the model to a real crack-like pipelines defect

4.4.1 Application of the model to a real case (F22 pipeline)

Once that the experimental data for the test at T=23°C and at load frequency equal to $f=1\text{Hz}$ were obtained, it was possible, as shown above, to get crack growth rates at different temperatures and frequencies with good approximation.

In order to apply experimental data to a real case, it is necessary to implement the equations of the model in order to obtain a numerical analysis of the crack growth inside the pipeline. A semi elliptical longitudinal crack in a pipeline is schematized, with the aim to apply the model to an actual application, see Figure 4.7.

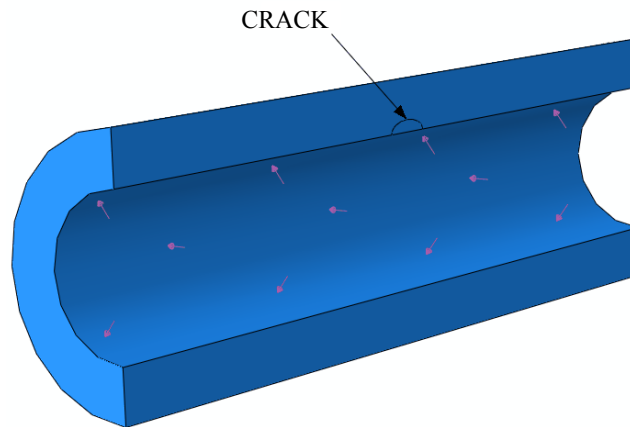


Figure 4.7. Modeling of the pipeline with a crack

A semi-elliptical crack is schematized, because the theoretical relations of the stress intensification factors is known. In Figure 4.8 crack geometry is shown.

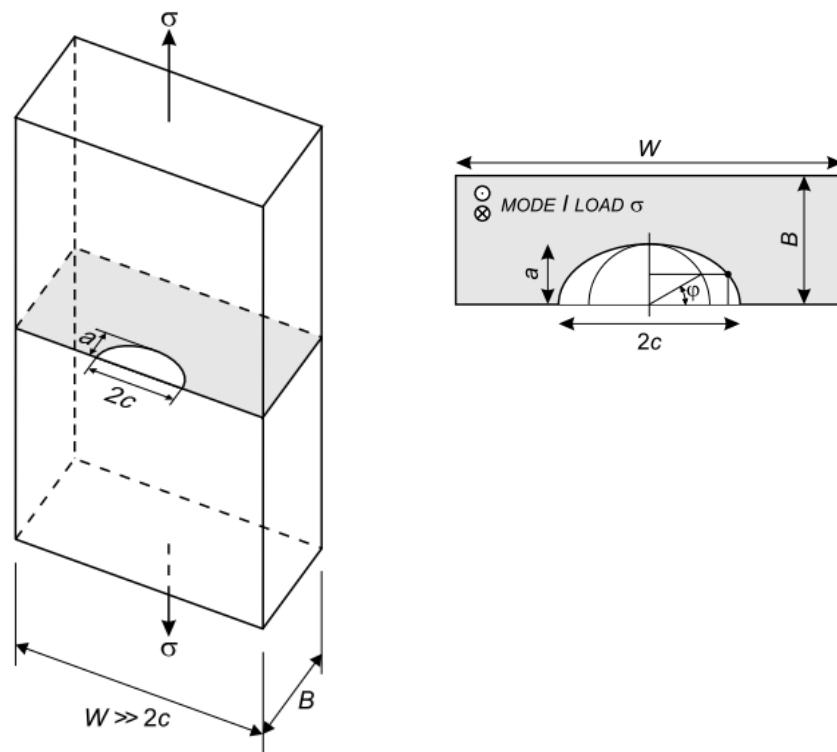


Figure 4.8. Crack Geometry

In order to calculate stress intensification factor the following equation [74] is used:

$$K_I = F \frac{\sigma \sqrt{\pi a}}{\Phi} \left(\sin^2 \varphi + \frac{a_c^2}{c^2} \cos^2 \varphi \right)^{1/4} \quad 4.7$$

Where F is a geometric function, depending on a , c and φ ; Φ is a coefficient depending on a and c . A sinusoidal internal pressure with $R=0.1$ is applied. The maximum pressure is 830 bar and the minimum value is 83 bar. The circumferential stresses and the stress intensity factors are then calculated. Circumferential stresses patterns through the thickness are shown in Figure 4.9.

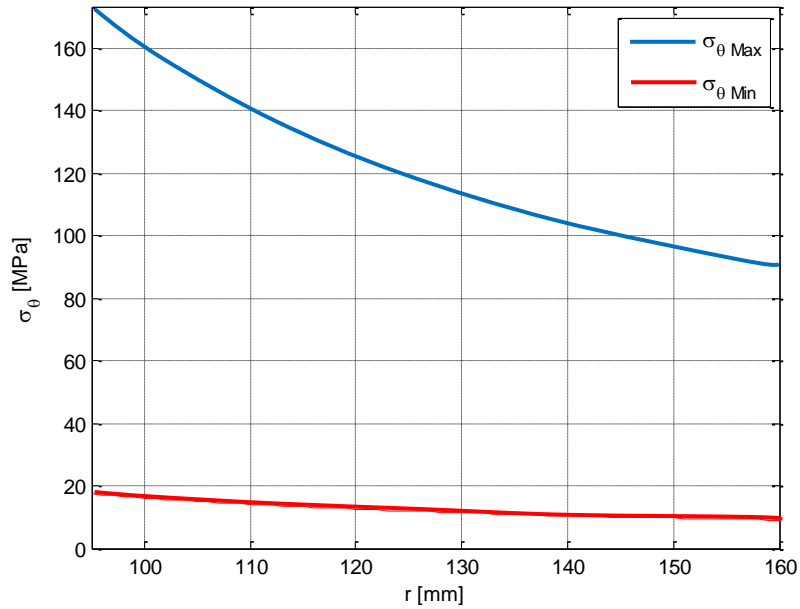


Figure 4.9. F22 pipeline: circumferential stress along thickness

For an easier coverage of the problem it was consider as the applied stress the average circumferential stress is considered as applied stress.

$$\begin{cases} \sigma_{\theta}^{\max_media} = 121.5 MPa \\ \sigma_{\theta}^{\min_media} = 12.1 MPa \end{cases} \quad 4.8$$

As initial crack dimensions, a and c , the values given in Figure 4.10 are chosen.

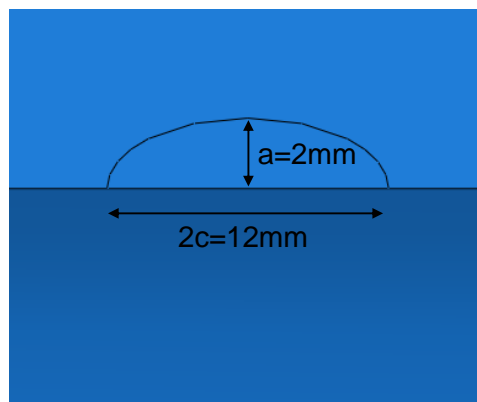


Figure 4.10. Crack dimensions

In these conditions, initial ΔK is:

$$\left. \begin{aligned} K_{I_{\max}} &= 9.432 \text{ MPa}\sqrt{m} \\ K_{I_{\min}} &= 0.943 \text{ MPa}\sqrt{m} \end{aligned} \right\} \Delta K = 8.489 \text{ MPa}\sqrt{m} \quad 4.9$$

Values were calculated in the point of maximum stress, $\varphi = 90^\circ$, whereas initial ΔK for $\varphi = 0^\circ$ is:

$$\left. \begin{aligned} K_{I_{\max_2C}} &= 3.459 \text{ MPa}\sqrt{m} \\ K_{I_{\min_2C}} &= 0.346 \text{ MPa}\sqrt{m} \end{aligned} \right\} \Delta K = 3.114 \text{ MPa}\sqrt{m} \quad 4.10$$

Through data obtained from toughness tests it is possible to obtain J_c values for the F22 steel with and without hydrogen presence.

$$\left. \begin{aligned} J_{c_NoH_F22} &= 800 \text{ kJ} / \text{m}^2 \\ J_{c_H_F22} &= 150 \text{ kJ} / \text{m}^2 \end{aligned} \right\} \quad 4.11$$

The value of J_c taken for the uncharged case is lower than the real value in fact it is taken as the average value between data obtained at $T=-80^\circ\text{C}$ and crack propagation during test is not enough extended to obtain a J_c (really, it is a J_q instead of a J_c , as mention in Chapter 3). From this values it is possible to obtain K_{Ic} through the following equation.

$$K = \sqrt{\frac{J \cdot E}{(1 - \nu^2)}} \quad 4.12$$

Values are:

$$\left. \begin{aligned} K_{Ic_NoH_F22} &= 425 \text{ MPa}\sqrt{m} \\ K_{Ic_H_F22} &= 184 \text{ MPa}\sqrt{m} \end{aligned} \right\} \quad 4.13$$

Rearranging equation and using as K_I the known value of K_{Ic} and the maximum stress, it is possible to calculate the critical length of the crack. According to this procedure critical crack length are:

$$\left. \begin{aligned} a_{c_NoH_F22} &= 4060 \text{ mm} \\ a_{c_H_F22} &= 761 \text{ mm} \end{aligned} \right\} \quad 4.14$$

Results are extremely high and higher than the thickness of the pipeline that is equal to 65mm; in this case there will be a leakage before break. On the other hand, considering the ductility of the material, plastic collapse should be taken into account.

Calculations were performed according to BS regulations [80]. The reference stress is defined as it follows:

$$\sigma_{ref} = \frac{P_b + (k_m - 1)P_m + [(P_b + (k_m - 1)P_m)^2 + 9P_m^2(1 - \alpha)^2]^{0.5}}{3(1 - \alpha)^2} \quad 4.15$$

If bending stresses are not considered, and $k_m=1$ is imposed, in absence of notches in the material, it is possible to apply the following equation:

$$\sigma_{ref} = \frac{-P_m + [(-P_m)^2 + 9P_m^2(1 - \alpha)^2]^{0.5}}{3(1 - \alpha)^2} \quad 4.16$$

With:

$$\alpha = \frac{(a / B)}{1 + \frac{B}{c}} \quad 4.17$$

Where P_m was chosen as the average maximum circumferential stress equal to 121.5MPa. Imposing the critical value $\sigma_{ref} = \sigma_f$, σ_f , the critical stress can be calculated as it follows:

$$\sigma_f = \frac{\sigma_{YS} + \sigma_{UT}}{2} = 500 \quad 4.18$$

With $\sigma_{YS}=415\text{MPa}$ and $\sigma_{UT}=585\text{MPa}$ obtained through ASME [53]. Rearranging equation 4.16 and imposing $2c=6a$ it is estimated that plastic collapse occurs for a crack length equal to:

$$a_{c_pl} = 61 \text{ mm} \quad 4.19$$

Therefore shortly before the end of the thickness equal to 65mm.

It is also possible to estimate the number of cycles to failure for the pipeline, under this loading condition and with the crack geometry defined in Figure 4.10. In Figure 4.11 the diagram of crack propagation at initial $\Delta K=8.489\text{MPa}\sqrt{\text{m}}$ is shown for a load frequency of $f=1\text{Hz}$.

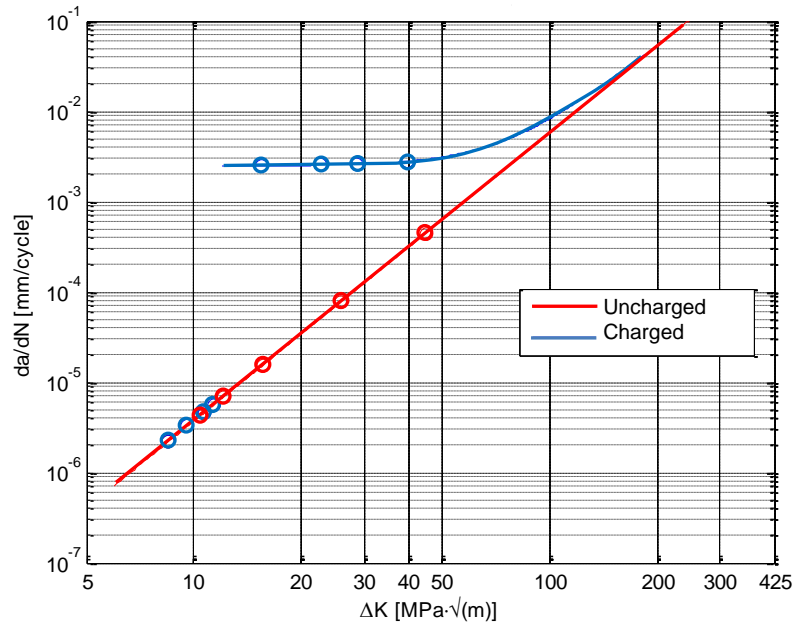


Figure 4.11. F22 pipeline: crack propagation diagram at $f=1\text{Hz}$ and $T=23^\circ\text{C}$

It can be noted that, for low ΔK , hydrogen effect is not relevant and propagation occurs following the Paris line of the uncharged material. Once $\Delta K=12\text{MPa}\sqrt{\text{m}}$ is reached, hydrogen effect increases crack growth rate. When the crack length reaches a value of 61mm plastic collapse occurs; this length is reached by the uncharged material in a number of cycles double compared to the hydrogen charged material:

$$\begin{aligned} Cycles_{end_NoH} &= 2,185,589 \\ Cycles_{end_H_1Hz_23^\circ C} &= 989,292 \end{aligned} \quad 4.20$$

Figure 4.12 shows crack length as a function of the number of loading cycles for charged and uncharged material.

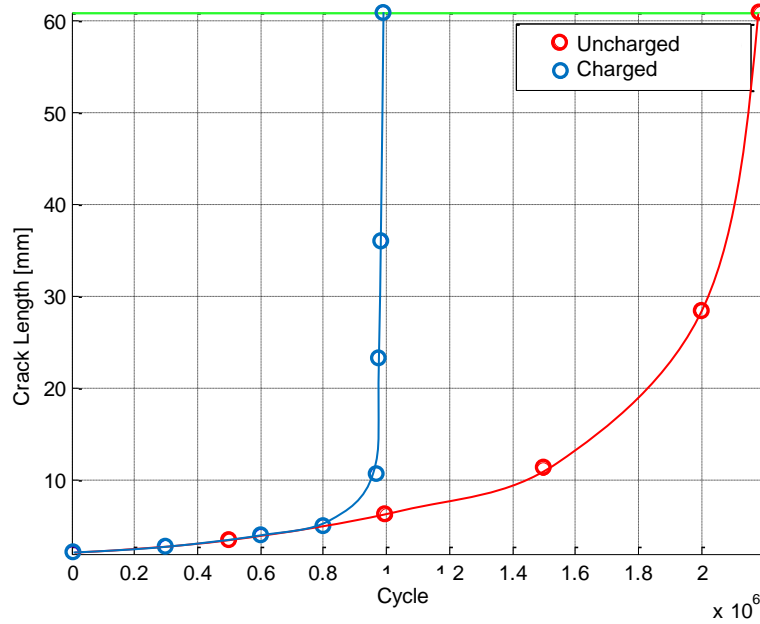


Figure 4.12. F22 pipeline: crack length as function of cycles at $f=1\text{Hz}$ and $T=23^\circ\text{C}$

It is also possible to estimate graphically the crack growth shape as a function of the number of loading cycles, as shown in Figure 4.13 and Figure 4.14.

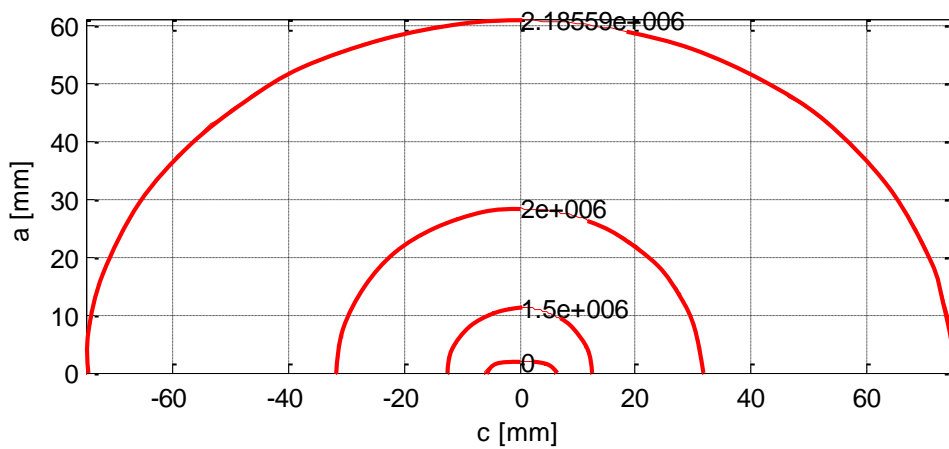


Figure 4.13. F22 pipeline: crack growth as function of cycles for uncharged material at $f=1\text{Hz}$ and $T=23^\circ\text{C}$

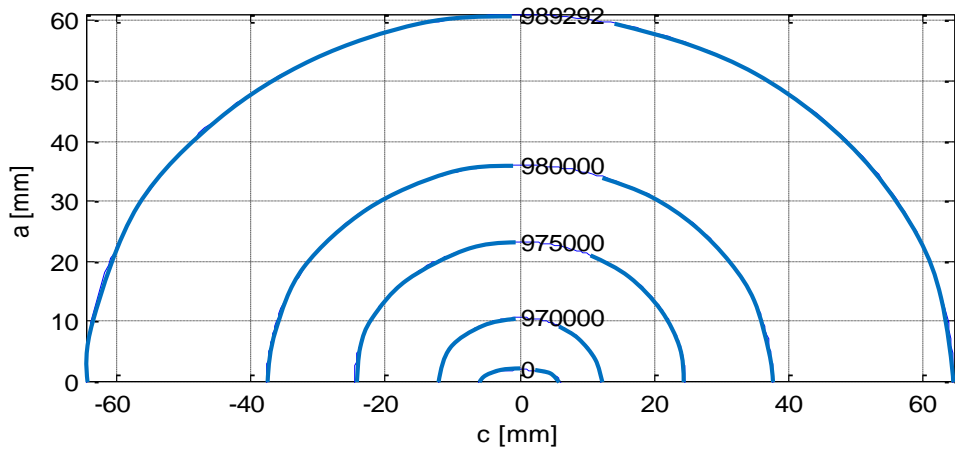


Figure 4.14. F22 pipeline: crack growth as function of cycles for charged material at $f=1\text{Hz}$ and $T=23^\circ\text{C}$

If the frequency of the variable loading is higher, for example frequency equals to $f=10\text{Hz}$, it would be possible to use the model to predict the number of cycles to failure, while keeping constant crack geometry and loading parameter; results are shown below:

$$Cycles_{end_H_10Hz_23^\circ C} = 1,123,735 \quad 4.21$$

The number of cycles to failure for the material without hydrogen remains constant while varying frequency. In Figure 4.15 crack propagation diagram for F22 pipeline at $f=10\text{Hz}$ and $T=23^\circ\text{C}$ is shown while in Figure 4.16 the crack length as a function of the number of loading cycles either for hydrogen charged and uncharged case is shown.

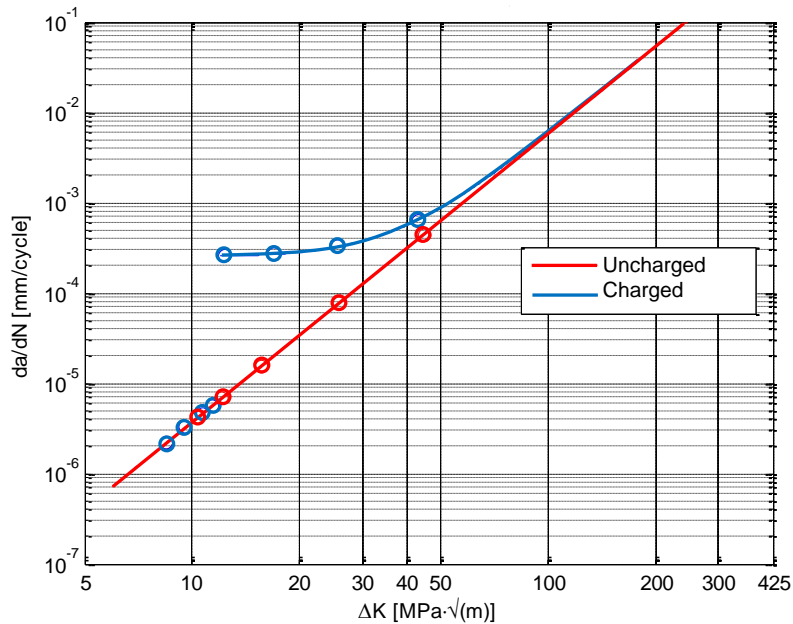


Figure 4.15. F22 pipeline: crack propagation diagram at $f=10\text{Hz}$ and $T=23^\circ\text{C}$

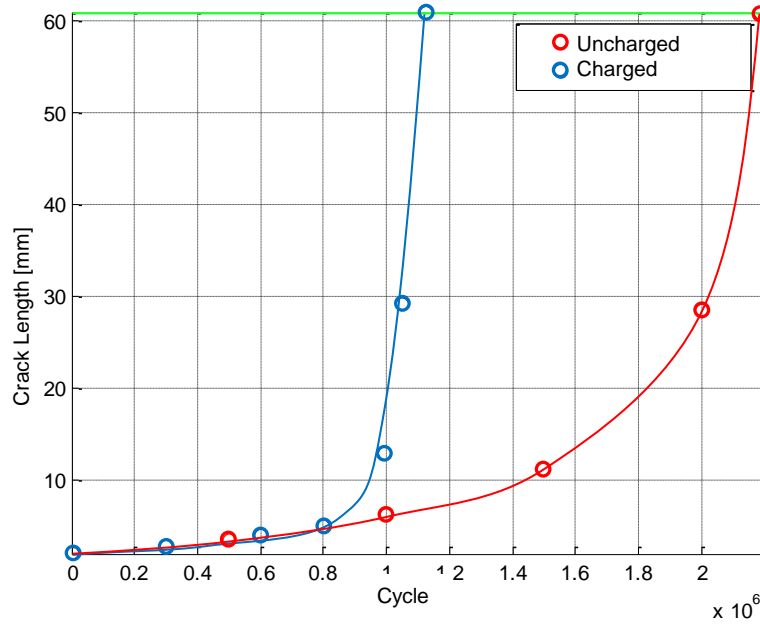


Figure 4.16. F22 pipeline: crack length as function of cycles at $f=10$ Hz and $T=23^{\circ}\text{C}$

It is also possible to vary the temperature and investigate, through the model, the number of cycles to failure in case of $T=-30^{\circ}\text{C}$ and $f=1\text{Hz}$; the number of cycles to failure are:

$$Cycles_{end_H_1Hz_-30^{\circ}\text{C}} = 1,042,985 \quad 4.22$$

In Figure 4.17 crack propagation diagram for the material with and without hydrogen is reported.

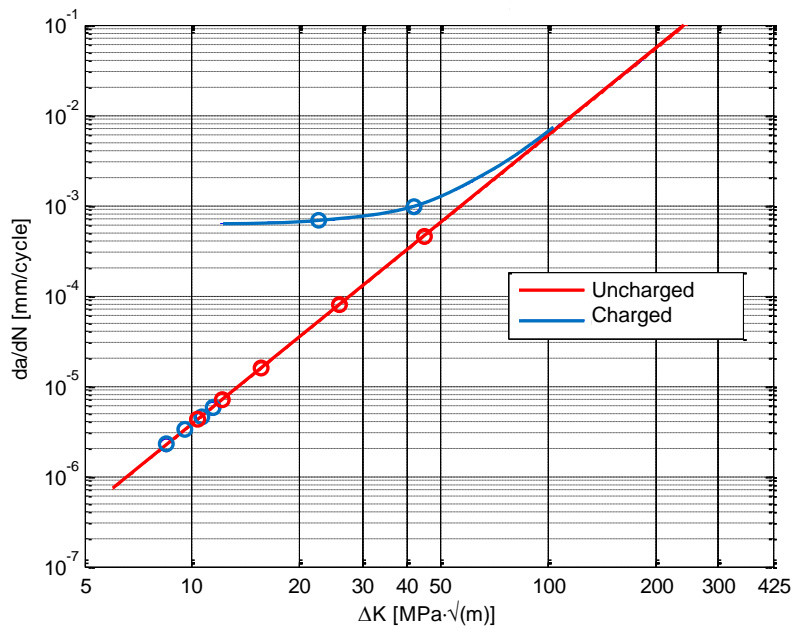


Figure 4.17. F22 pipeline: crack propagation diagram at $f=1\text{Hz}$ and $T=-30^{\circ}\text{C}$

4.4.2 Application of the model to a real case (X65 pipeline)

In this section the numerical analysis used for the F22 pipeline is carried out for X65 pipeline. Pressure ratio is kept constant with $P_{\max}=830\text{bar}$ and $P_{\min}=83\text{bar}$; outer diameter of the pipe is equal to $D_o=323\text{mm}$ and the thickness is equal to $t=46\text{mm}$. In these conditions circumferential stresses, maximum and minimum, are shown in Figure 4.18.

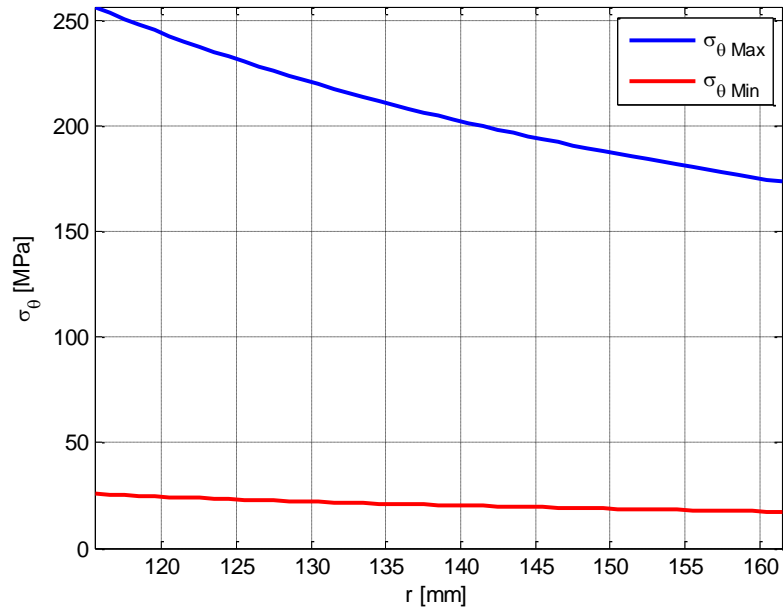


Figure 4.18. X65 pipeline: circumferential stress along thickness

Also in this case the average circumferential stress is taken for the analysis:

$$\begin{cases} \sigma_{\theta}^{\max_media} = 215.3 \text{ MPa} \\ \sigma_{\theta}^{\min_media} = 21.5 \text{ MPa} \end{cases} \quad 4.23$$

At $\varphi = 90^\circ$ ΔK is equal to the following values:

$$\left. \begin{aligned} K_{I\max} &= 15.395 \text{ MPa}\sqrt{m} \\ K_{I\min} &= 1.539 \text{ MPa}\sqrt{m} \end{aligned} \right\} \Delta K = 13.856 \text{ MPa}\sqrt{m} \quad 4.24$$

From test data it is possible to obtain J_c for X65 steel either with hydrogen and without.

$$\begin{aligned} J_{c_NoH_X65} &= 900 \text{ kJ} / \text{m}^2 \\ J_{c_H_X65} &= 90 \text{ kJ} / \text{m}^2 \end{aligned} \quad 4.25$$

J_c value is taken as the average value between data obtained at $T=-70^\circ\text{C}$.

From this values it is possible to obtain K_{Ic} through the following equation.

$$\begin{aligned} K_{Ic_NoH_X65} &= 452 \text{ MPa}\sqrt{m} \\ K_{Ic_H_X65} &= 143 \text{ MPa}\sqrt{m} \end{aligned} \quad 4.26$$

Critical crack lengths are equal to:

$$\begin{aligned} a_{c_NoH} &= 1724 \text{ mm} \\ a_{c_H} &= 173 \text{ mm} \end{aligned} \quad 4.27$$

Results are really high and larger than the thickness of the pipeline that is equal to $t=46\text{mm}$; in this case there will be a leakage before break.

On the other hand, considering the ductility of the material, plastic collapse should be taken into account. As P_m value, upper average circumferential stress is taken, that is equal to 215.3MPa. Assuming that the critical value is reached, it is imposed that $\sigma_{ref} = \sigma_f$ where σ_f can be obtain as it follows:

$$\sigma_f = \frac{\sigma_{YS} + \sigma_{UT}}{2} = 489.5 \text{ MPa} \quad 4.28$$

With $\sigma_{YS}=448\text{MPa}$ and $\sigma_{UT}=531\text{MPa}$ calculated through API 5L [54]. Rearranging equation 4.16 and imposing $2c=6a$ it was estimated that plastic collapse occurs for a crack length equal to:

$$a_{c_pl} = 39 \text{ mm} \quad 4.29$$

Hence before the end of the thickness equal to 46mm. It is also possible to estimate the number of cycles to failure for the pipeline under this loading condition and with a crack geometry defined in Figure 4.8.

In Figure 4.19 the diagram of crack propagation is shown for a load frequency of $f=1\text{Hz}$.

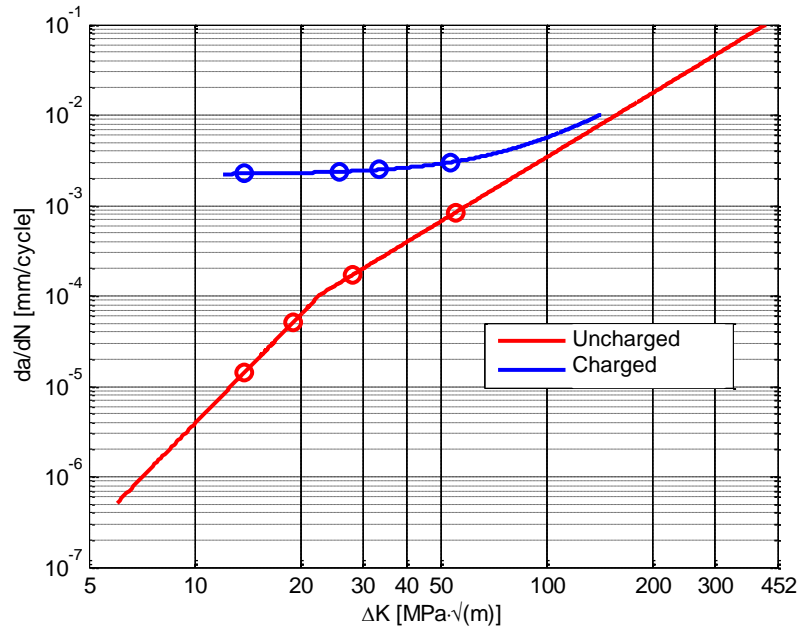


Figure 4.19. X65 pipeline: crack propagation diagram at $f=1\text{Hz}$ and $T=23^\circ\text{C}$

When the crack length has reached a value of 39mm plastic collapse occurs; Failure crack lengths in charged and uncharged cases are reached after the following cycles:

$$\begin{aligned} \text{Cycles}_{\text{end_NoH_X65}} &= 267,743 \\ \text{Cycles}_{\text{end_H_1Hz_23}^\circ\text{C_X65}} &= 14,269 \end{aligned} \quad 4.30$$

In Figure 4.20 crack length as a function of number of cycles is shown for X65 pipeline.

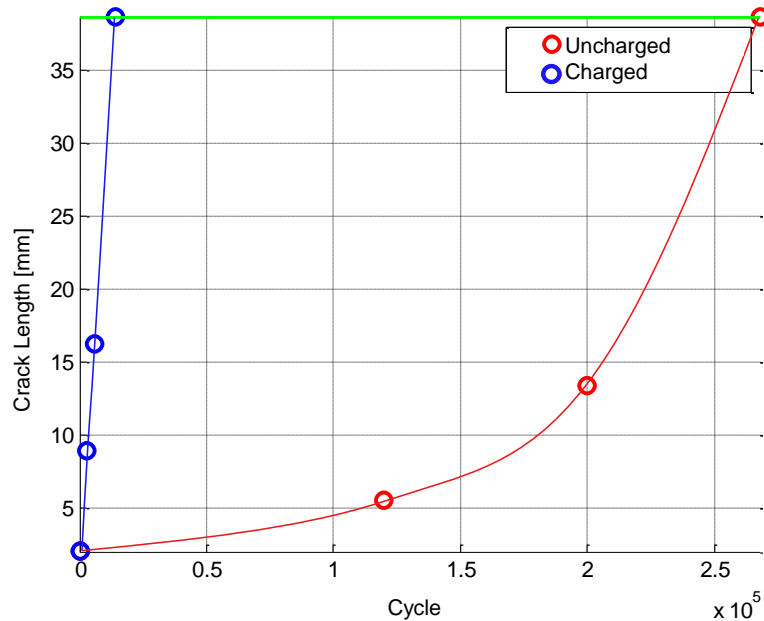


Figure 4.20. X65 pipeline: crack length as function of cycles at $f=1\text{Hz}$ and $T=23^\circ\text{C}$

It is also possible to estimate graphically the crack growth shape as a function of the number of cycles, as shown in Figure 4.21 and Figure 4.22.

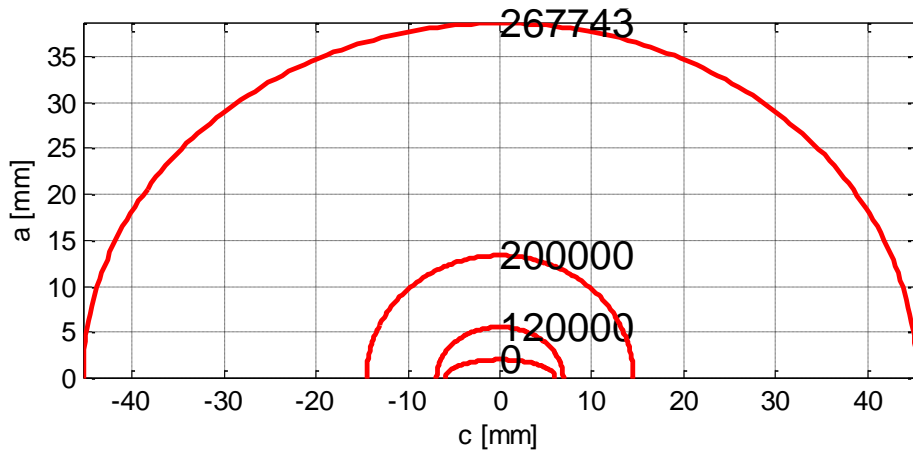


Figure 4.21. X65 pipeline: crack growth as function of cycles for uncharged material at $f=1\text{Hz}$ and $T=23^\circ\text{C}$

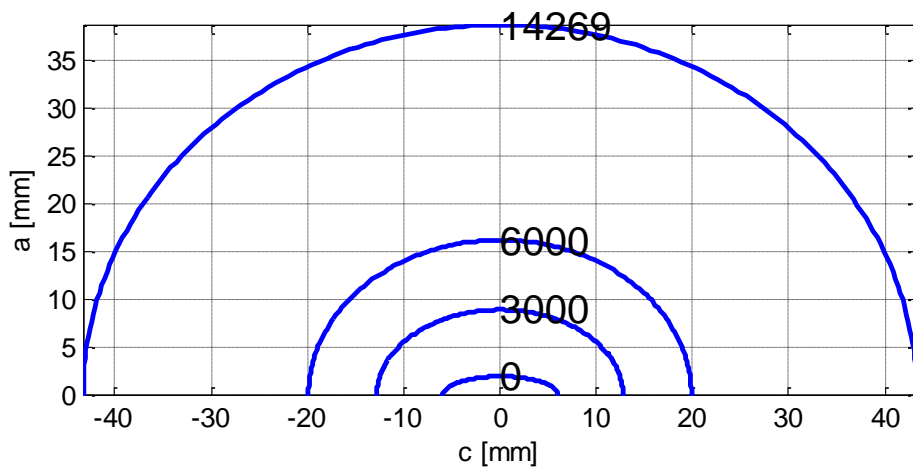


Figure 4.22. X65 pipeline: crack growth as function of cycles for charged material at $f=1\text{Hz}$ and $T=23^\circ\text{C}$

For higher frequency, $f=10\text{Hz}$, cycles to failure are evaluated and equal to:

$$Cycles_{end_H_10\text{Hz}_23^\circ\text{C}} = 74,389 \quad 4.31$$

The number of cycles to failure for the material without hydrogen remains constant while varying frequency. In Figure 4.23 crack propagation diagram for X65 pipeline at $f=10\text{Hz}$ and $T=23^\circ\text{C}$ is shown while in Figure 4.24 the crack length as a function of the number of cycles either for hydrogen charged and uncharged is shown.

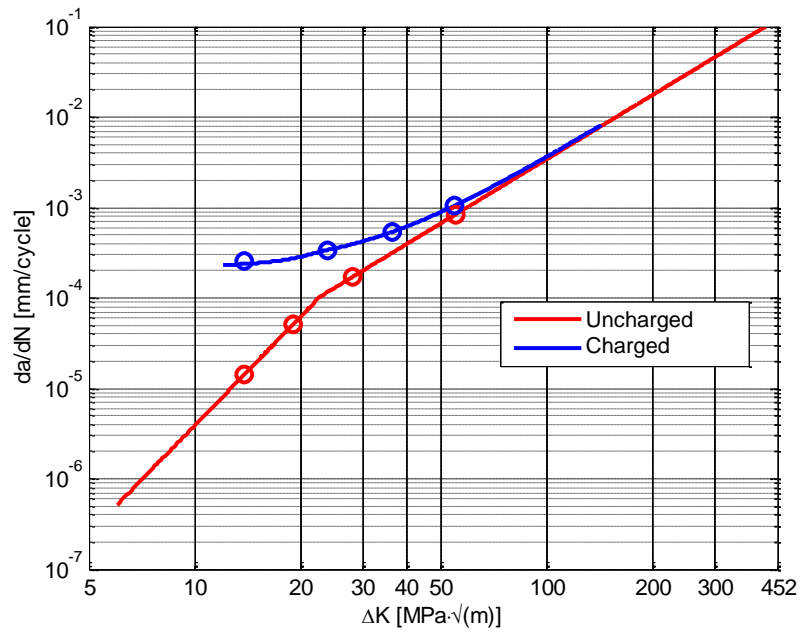


Figure 4.23. X65 pipeline: crack propagation diagram at $f=10\text{Hz}$ and $T=23^\circ\text{C}$

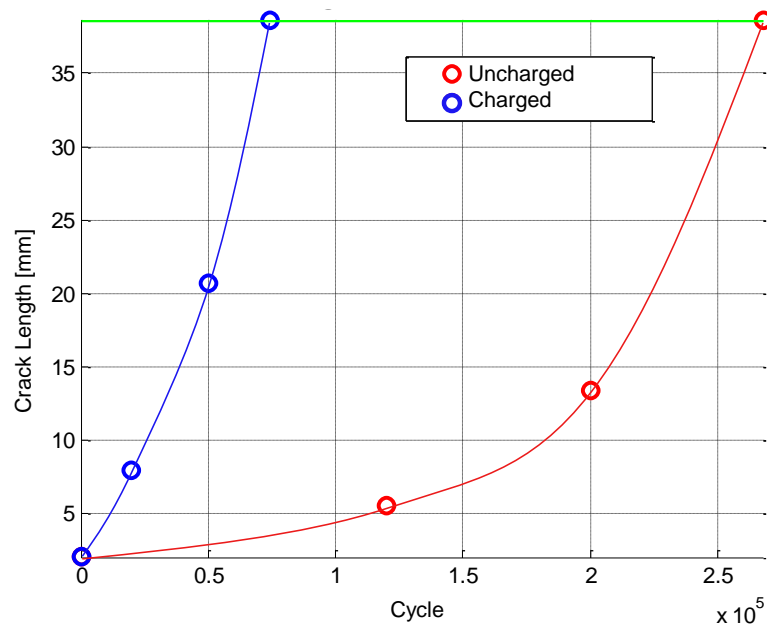


Figure 4.24. X65 pipeline: crack length as function of cycles at $f=10\text{Hz}$ and $T=23^\circ\text{C}$

It is also possible to vary the temperature and investigate, through the model, the number of cycles to failure in case of a temperature equal to $T=-30^\circ\text{C}$ and a loading frequency of $f=1\text{Hz}$; the number of cycles to failure are equal to:

$$Cycles_{end_H_1Hz_ -30^\circ C} = 42,620$$

4.32

In Figure 4.25 the variation of crack propagation rate at $T=-30^{\circ}\text{C}$ is shown.

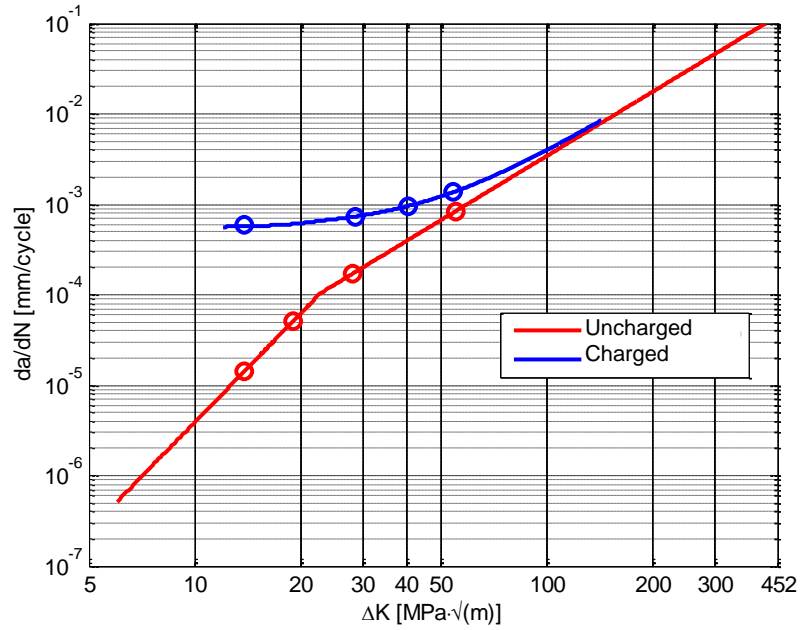


Figure 4.25. X65 pipeline: crack propagation diagram at $f=1\text{Hz}$ and $T=-30^{\circ}\text{C}$

For this situation the respective crack length versus number of cycles is depicted in Figure 4.26.

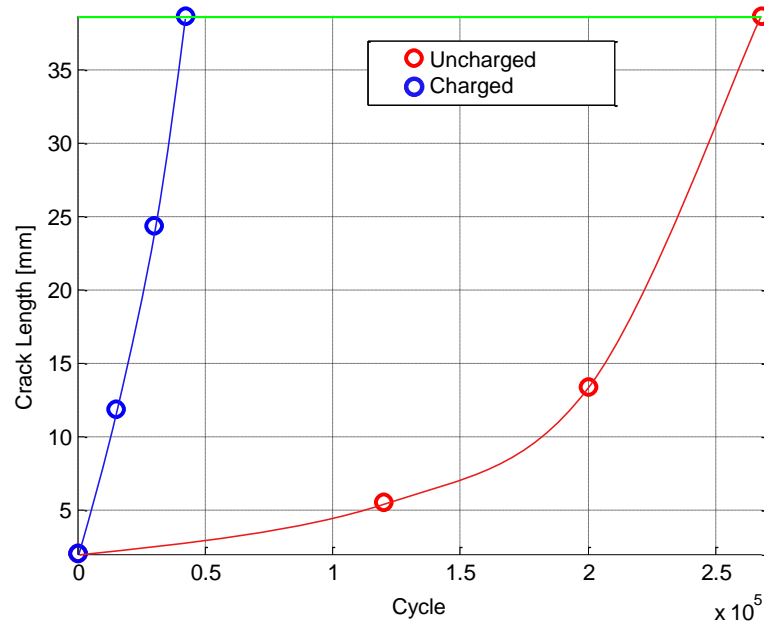


Figure 4.26. X65 pipeline: crack length as function of cycles at $f=1\text{Hz}$ and $T=-30^{\circ}\text{C}$

4.5 Remarks on models and its application

The superposition model and the thermal model proposed to reproduce the materials behaviour, seem to fit reasonably the test data respect all the dependences between environmental conditions and material behaviour and agree with previous investigations found in bibliography. Test data at low frequency and room temperature are better in order to develop the model, in fact, good agreement between experimental data and the modelled behaviour are observed. This fact can be owed to the enhanced hydrogen effect at low frequencies and higher temperatures; on the other hand at lower temperatures and higher frequencies, parameters that were not taken into account can influence more the behaviour. Another important fact that should be taken into account as a parameter, but for lack of tests was not possible to estimate, is the hydrogen content inside the lattice; from literature [20] it was found that, by varying hydrogen content, it is possible to have a better view of the embrittlement phenomenon. It was also shown that, the model is easy to implement in real cases and can be applied to service life estimations. The lack of the knowledge of ΔK_{th} can be a limit when short cracks are considered (short-crack mechanics need a different approach), nevertheless the model is a powerful and relatively simple tool in order to evaluate crack growth rates at different conditions without a large number of tests.

5 Fractographic Analysis

Special acknowledgement goes to Chemistry, Material and Chemical Engineering Department CMIC “Giulio Natta” of Politecnico di Milano where SEM fractographic observation on tested specimens are performed.

5.1 Charpy impact test (fractographic analysis)

5.1.1 Macro and micrographic examination: F22 steel

Figure 5.1 shows fracture surfaces of F22 specimens tested at different temperatures without hydrogen. Under every image test temperature, absorbed energy and portion of brittle area are reported.

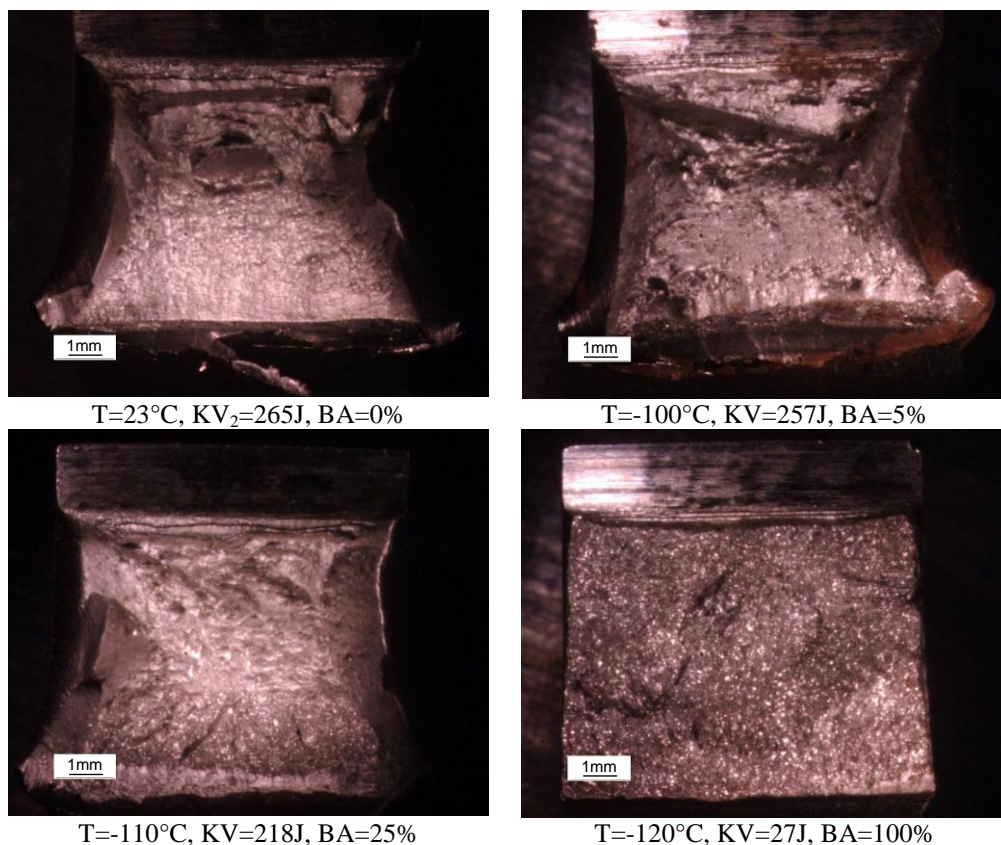


Figure 5.1. F22 steel: fracture surfaces for uncharged specimen at different temperatures

It can be observed that, until T=-100°C, the percentage of brittle area is very small, around 5%, and the whole surface seems to be plastically deformed, indicating a ductile fracture.

Furthermore, no shining pattern, typical of fragile separation, can be seen, demonstrating the ductile behaviour. Dislocations in the lattice are able to follow deformation forced to the specimen by the hammer and to cause a ductile rupture with clear plasticization areas. Microscopically, fracture surfaces show typical ductile rupture features: large plastic deformations, tearing and side expansion. Around temperature of about $T=-120^{\circ}\text{C}$ the lattice tends to become more stiff and dislocations are partially blocked by low temperature, that affects mobility. At this point brittle behaviour occurs.

This change can be observed by looking at the fracture surface of the specimen tested at $T=-110^{\circ}\text{C}$, and even more in the specimen tested at $T=-120^{\circ}\text{C}$. It can be seen that surface is less buckled, more regular and flatter; plastic deformation is drastically reduced, side expansion is actually inexistent, almost 100% of the fracture surface is brittle. Fracture surface appears crystalline, rough and bright. In Figure 5.2 fracture surfaces of F22 hydrogen charged specimens are shown.

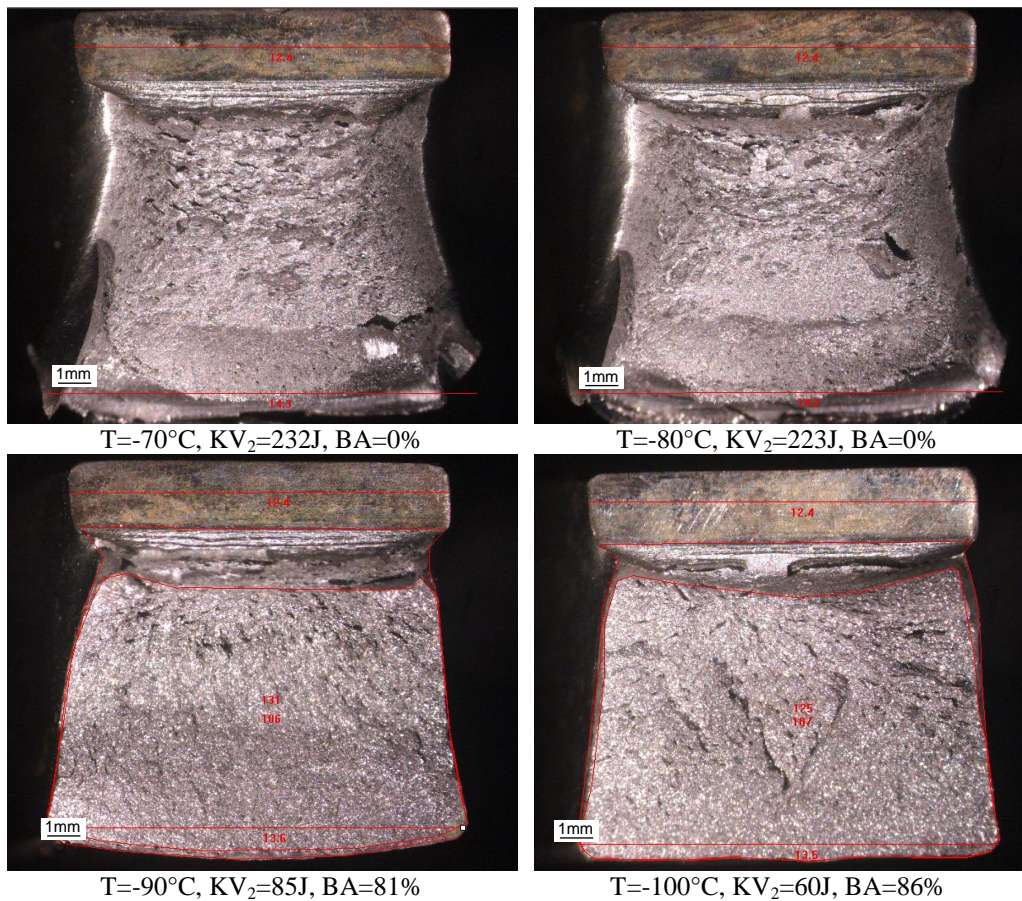
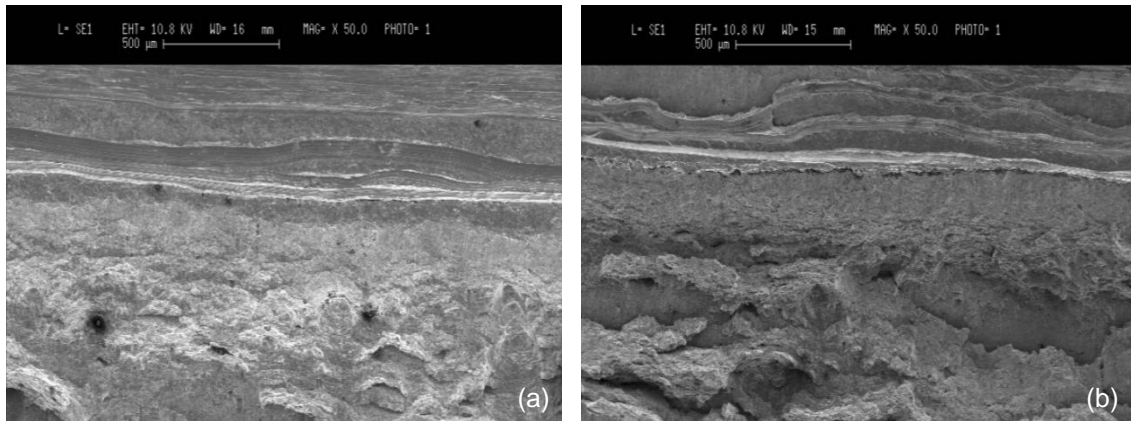


Figure 5.2. F22 steel: fracture surfaces for charged specimen at different temperatures

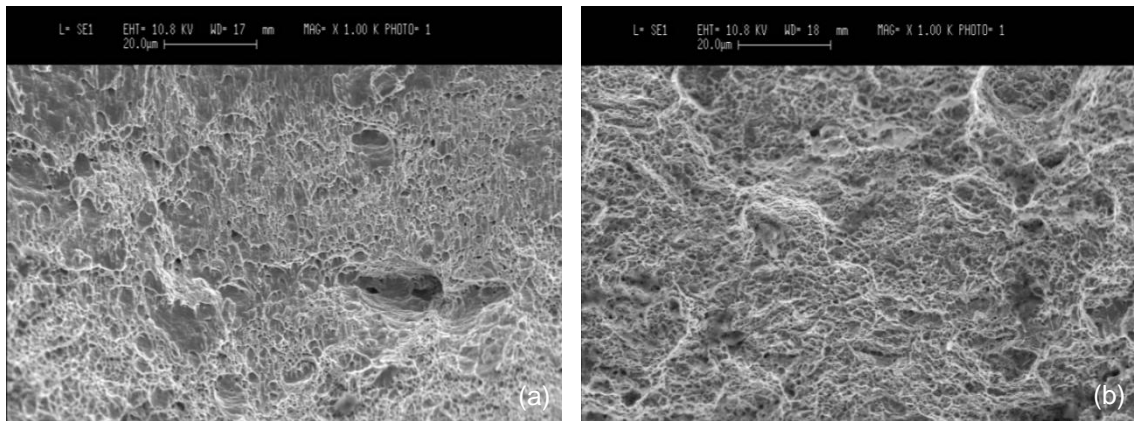
As it can be noticed from the width of the brittle area at temperature around $T=-90^{\circ}\text{C}$, there has been a remarkable change in the material response to the Charpy test after the charging. Around $T=-100^{\circ}\text{C}$ the material shows a complete brittle behaviour.

The micrographic examination of F22 is reported forwards. In Figure 5.3 cracks starts, occurred at the machined notches, are shown for charged and uncharged specimen.



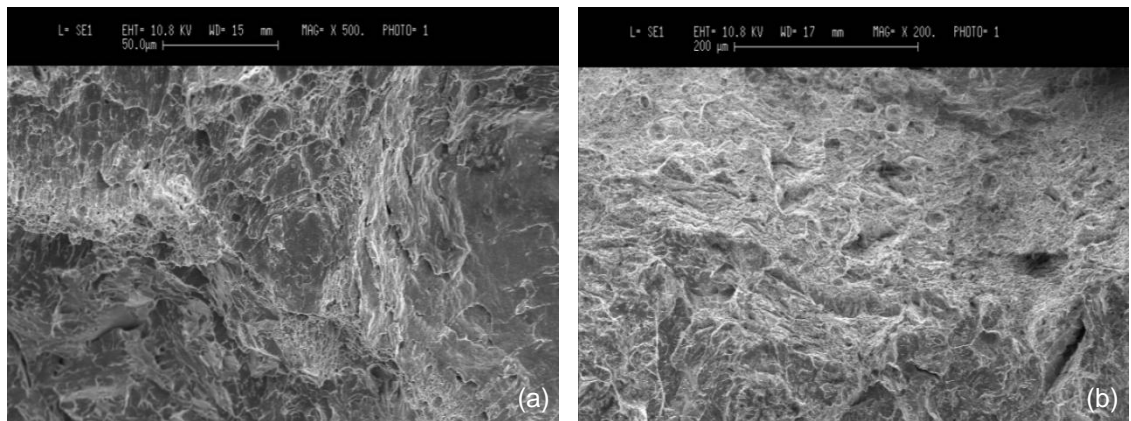
T=-110°C, KV₂=218J, BA=25% T=-100°C, KV₂=121J, BA=70%
Figure 5.3. F22 steel: fracture surface near notch for (a) uncharged and (b) charged specimen

Ductile crack propagation is similar in both specimens, charged and uncharged, and reported in Figure 5.4.



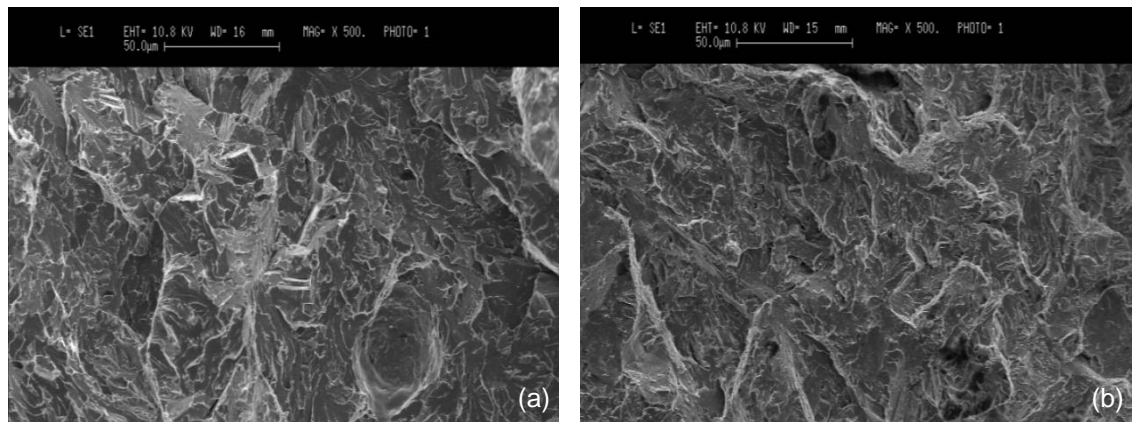
T=-80°C, KV₂=252J, BA=5% T=-80°C, KV₂=66J, BA=87%
Figure 5.4. F22 steel: ductile fracture for (a) uncharged and (b) charged specimen

Figure 5.5 shows the ductile-to-brittle transition for charged and uncharged material.



T=-110°C, KV₂=218J, BA=25% T=-80°C, KV₂=66J, BA=87%
Figure 5.5. F22 steel: ductile-to-brittle transition for (a) uncharged and (b) charged specimen

Figure 5.6 shows a region characterized by brittle behaviour.

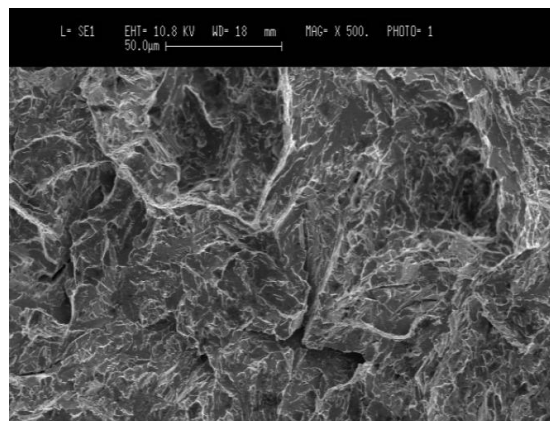


T=-120°C, KV₂=27J, BA=100%

T=-95°C, KV₂=140J, BA=47%

Figure 5.6. F22 steel: brittle fracture for (a) uncharged and (b) charged specimen

Another examples, showing a quasi-cleavage fracture surface, is reported in Figure 5.7.

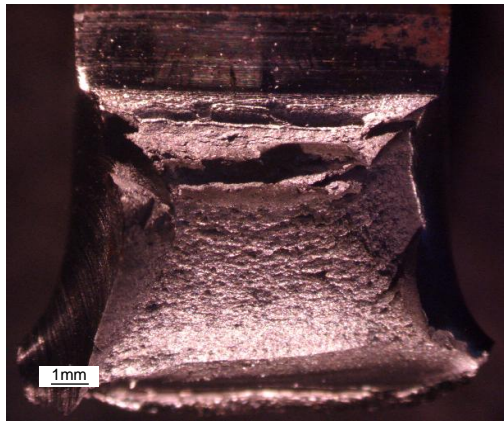


T=-110°C, KV₂=18J, BA=100%

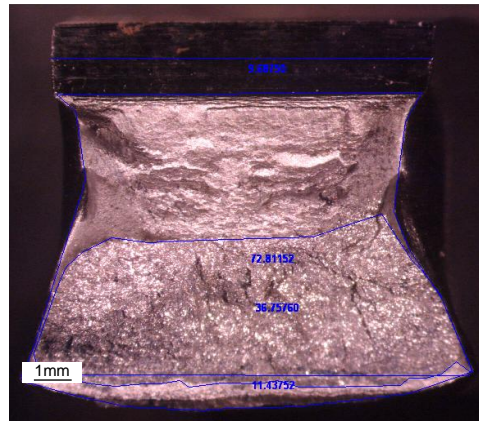
Figure 5.7. F22 steel: brittle fracture reporting some aspect of quasi-cleavage separations

5.1.2 Macro and micrographic examination: X65 steel

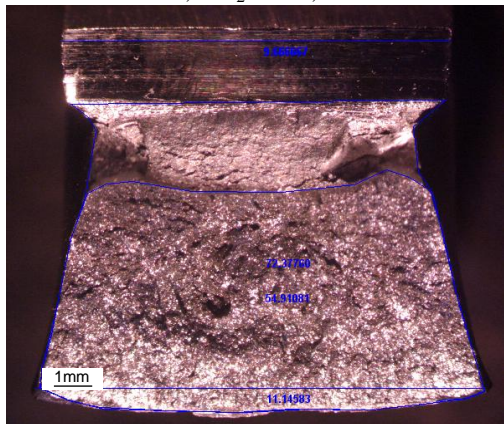
Also X65 steel shows similar changes in Charpy test response when charged, nevertheless the temperature shift, in ductile-brittle transition, is less pronounced compared to F22 steel. Figure 5.8 shows fracture surfaces of X65 uncharged specimens.



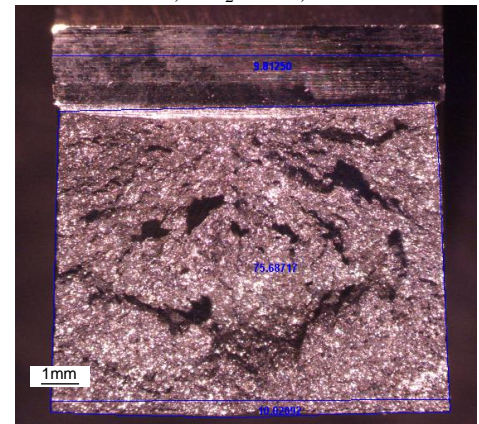
T=-20°C, KV₂=245J, BA=0%



T=-60°C, KV₂=156J, BA=50%



T=-90°C, KV₂=116J, BA=76%



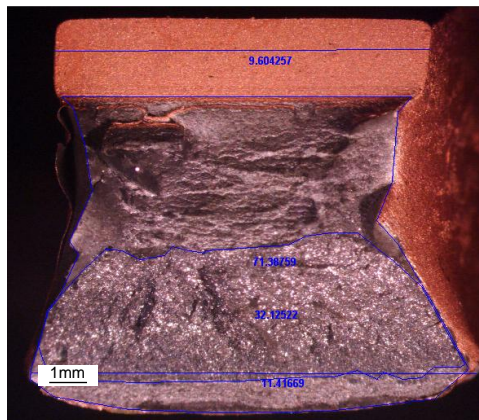
T=-100°C, KV₂=17.5J, BA=100%

Figure 5.8. X65 steel: fracture surfaces for uncharged specimen at different temperatures

Figure 5.9 shows fracture surfaces of X65 hydrogen charged specimens.



T=-20°C, KV₂=222J, BA=0%



T=-60°C, KV₂=172J, BA=45%

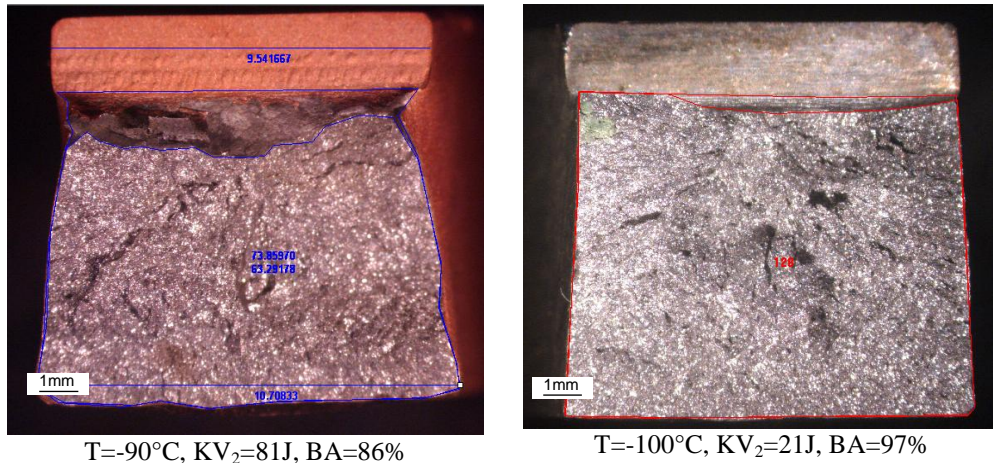


Figure 5.9. X65 steel: fracture surfaces for charged specimen at different temperatures

Comparing fracture surfaces of X65 charged and uncharged specimens, at same temperatures, it can be observed that there are no apparent differences between them. By observing, anyway, Charpy impact energy versus temperature, Figure 3.13, there is a small, though slight, change in transition temperature. Micrographic examinations of X65 specimens are reported forward. The ductile behaviour for hydrogen charged and uncharged specimens is shown in Figure 5.10.

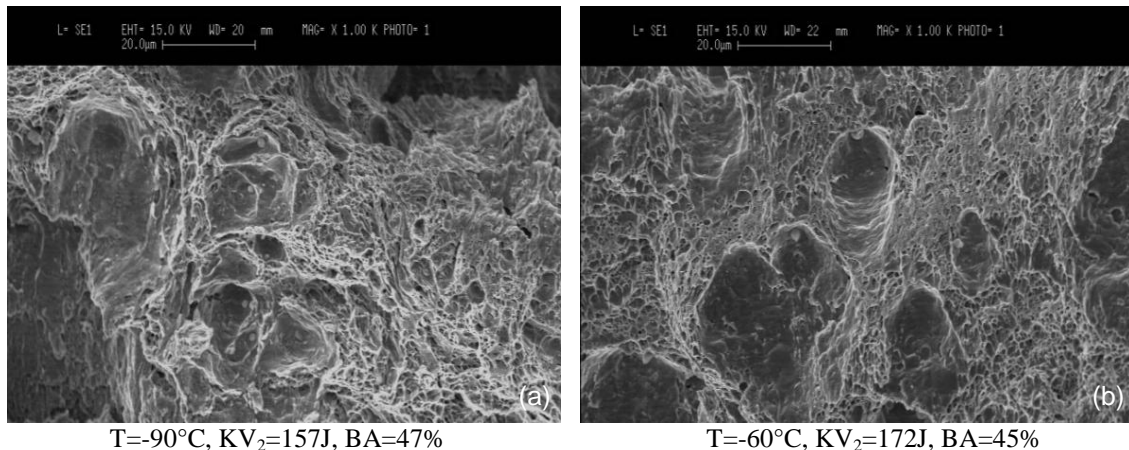


Figure 5.10. X65 steel: ductile fracture for (a) uncharged and (b) charged specimen

Dimples appearance seems the same in hydrogen charged and uncharged material, both generated around inclusions and with similar surface features. Ductile-to-brittle fracture for charged and uncharged material is shown in Figure 5.11.

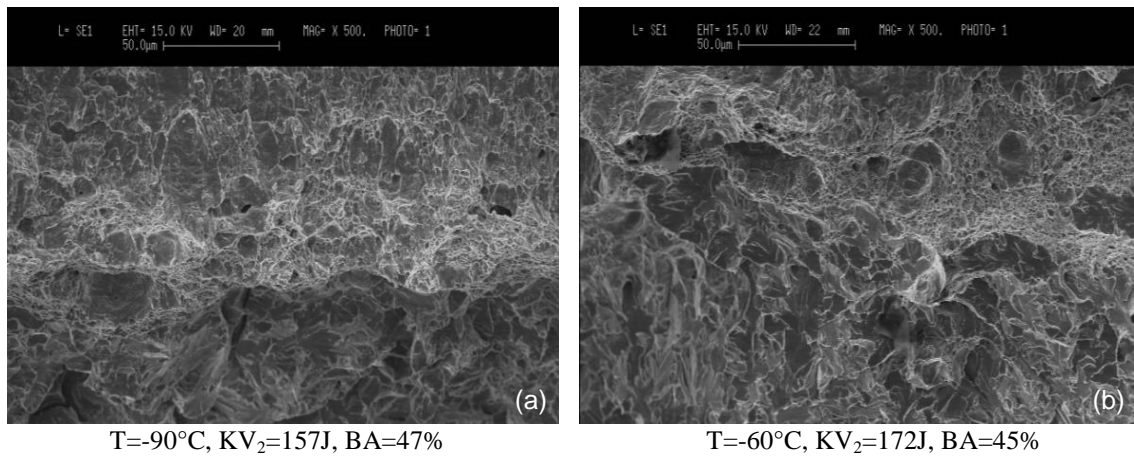


Figure 5.11. X65 steel: ductile-to-brittle fracture for (a) uncharged and (b) charged specimen

Also in this case no significant differences are observable. Finally, the brittle fracture behaviour is reported in Figure 5.12.

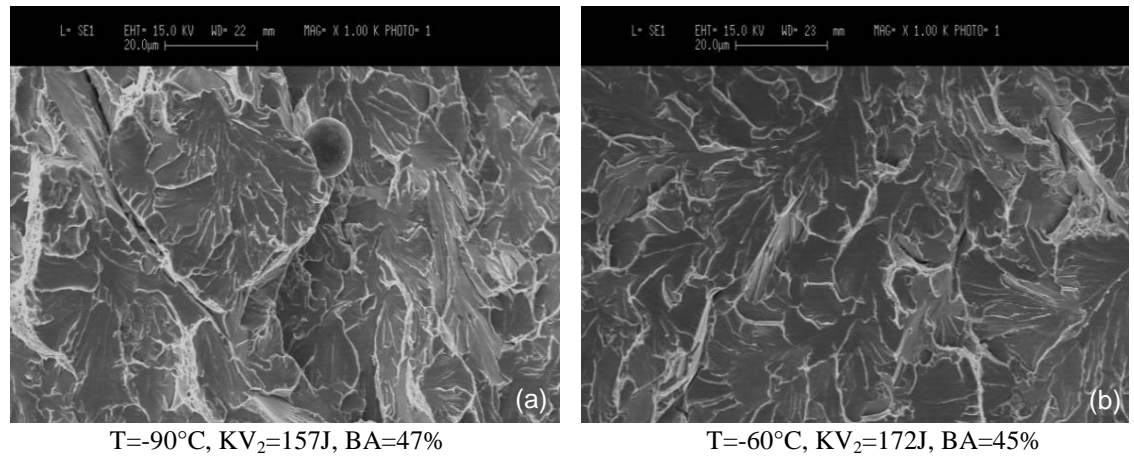


Figure 5.12. X65 steel: brittle fracture for (a) uncharged and (b) charged specimen

5.2 Toughness test (fractographic analysis)

5.2.1 Macro and micrographic examination: F22 steel

Both for F22 and X65 steels, macro and micrographic appearance, is similar. Obviously there is a fatigue crack growth in the precrack region, a crack tip blunting in the first part of the test propagation, a ductile crack extension and, when temperature is low enough and crack sufficiently long, a brittle propagation. A usual fracture appearance, of an F22 uncharged specimens, is reported in Figure 5.13.

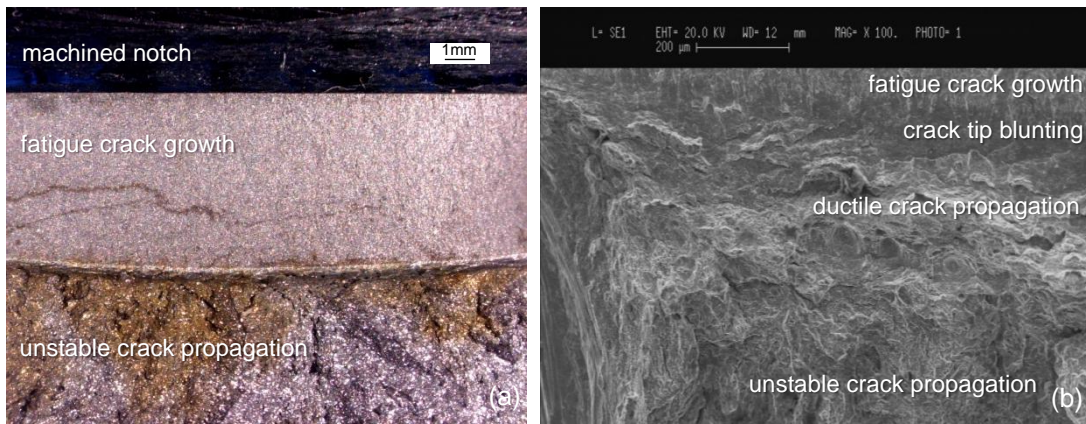


Figure 5.13. F22 steel: fracture surface morphology after toughness test at $T=-110^{\circ}\text{C}$ of uncharged specimens in (a) macro and (b) micrographic observation

From the macrographic image of Figure 5.13a it is possible to clearly distinguish the fatigue crack growth and the unstable propagation, whereas from the micrographic image of Figure 5.13b also blunting and little ductile propagation are observable. The presence of oxide is due to the slow drying phase after the unstable propagation. In order to avoid oxidation a quick drying of the fracture surfaces is needed.

The test was conducted at $T=-110^{\circ}\text{C}$ and the specimen reached an unstable propagation at a load of $P=46450\text{N}$ as shown in Figure 5.14 where the load versus displacement test history is reported.

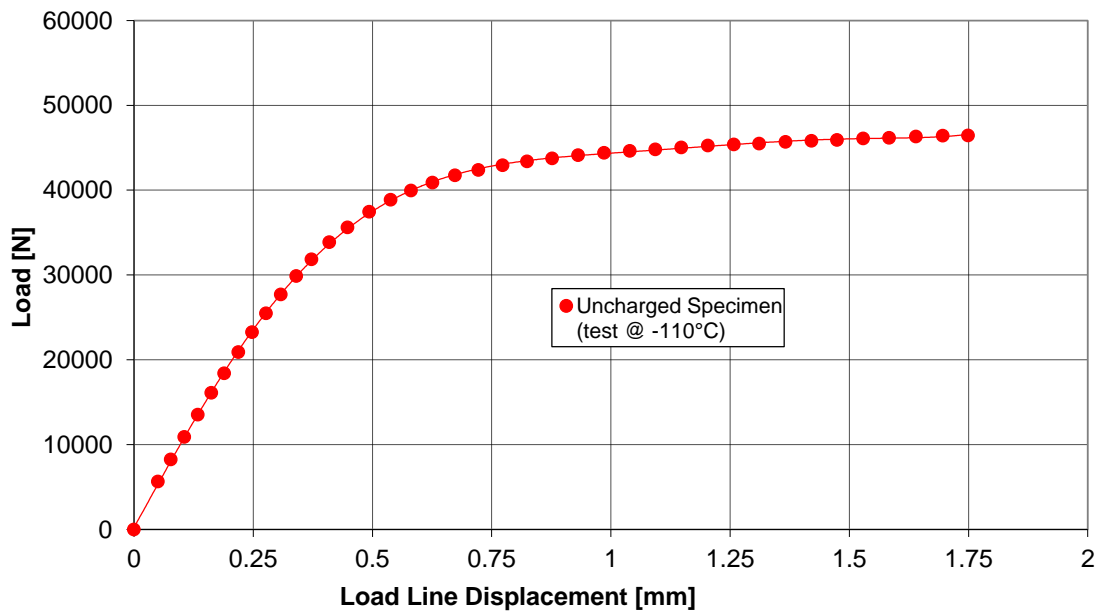


Figure 5.14. F22 steel: Load vs. LLD for uncharged specimen at $T=-110^{\circ}\text{C}$

A detail for each principal fracture areas is shown in Figure 5.15.

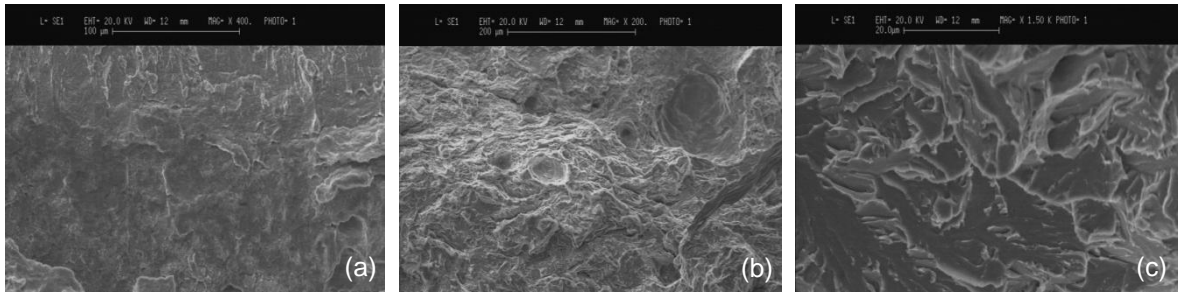


Figure 5.15. F22 steel: detail of (a) blunting zone, (b) ductile propagation and (c) unstable propagation

Figure 5.15b shows very flat dimples different in dimension; neither inclusions nor their imprints are visible at the dimples centre. The fracture surfaces of charged specimens change significantly and it is possible to observe a particular fracture typology called “cellular” [68]. Figure 5.16 shows the fracture morphology of a charged specimen tested at $T=-40^{\circ}\text{C}$. The toughness parameter is still high, of $J_q=379\text{kJ/m}^2$, but a remarkable decrease occurs and it is possible to observe a large stable propagation (Figure 5.16a).

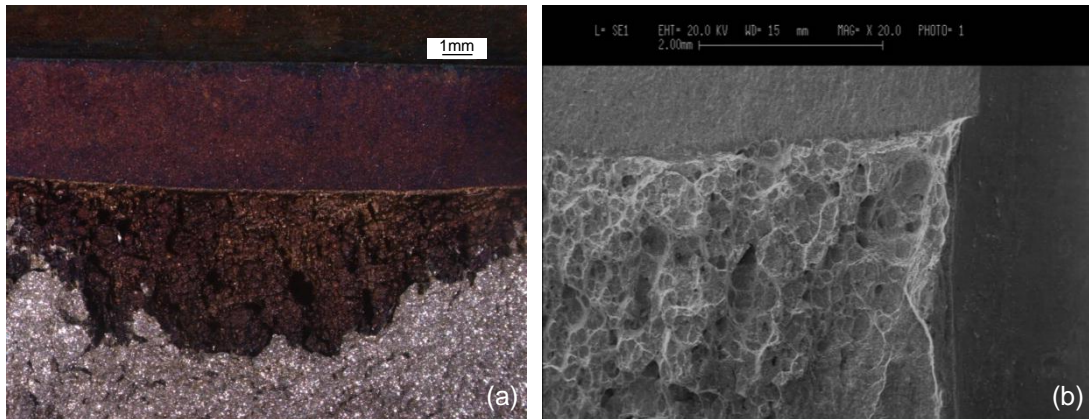


Figure 5.16. F22 steel: fracture surface morphology after toughness test at $T=-40^{\circ}\text{C}$ of charged specimens in (a) macro and (b) micrographic observation

The “cellular” pattern is clearly visible in Figure 5.16b. Cells are better visible in Figure 5.17 where details of Figure 5.16b are shown.

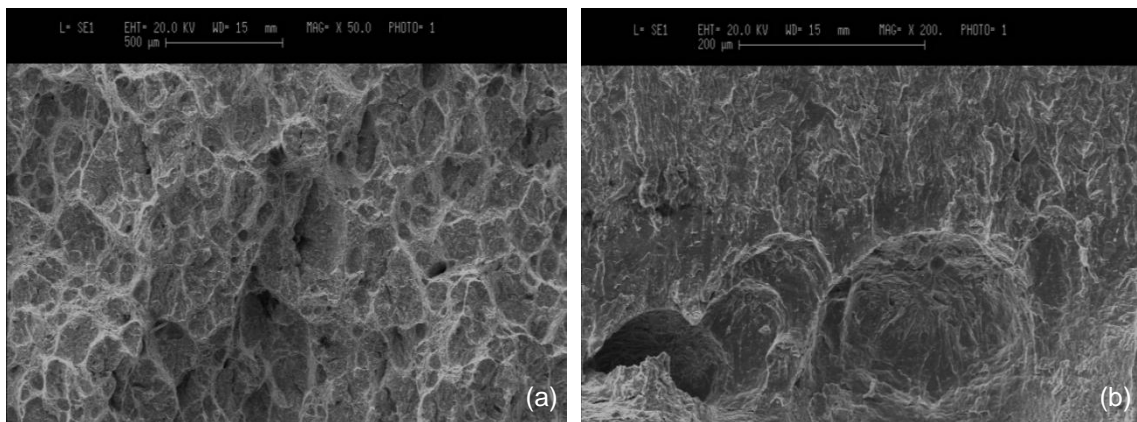


Figure 5.17. F22 steel: (a) “cellular” pattern and (b) a detail of a “cell”

Every “cell” is usually characterized by quasi-cleavage internal fracture morphology and a ductile edge that delimits every cell from another. An inclusion, or its imprint, is usually present in every cell.

5.2.2 Macro and micrographic examination: X65 steel

Also for uncharged X65 specimens the fractographic analysis reveals four different fracture areas, already mentioned for F22 steel. Macro and micrographic observations, of an uncharged specimen, are shown in Figure 5.18. The test was carried out at $T=-100^{\circ}\text{C}$.

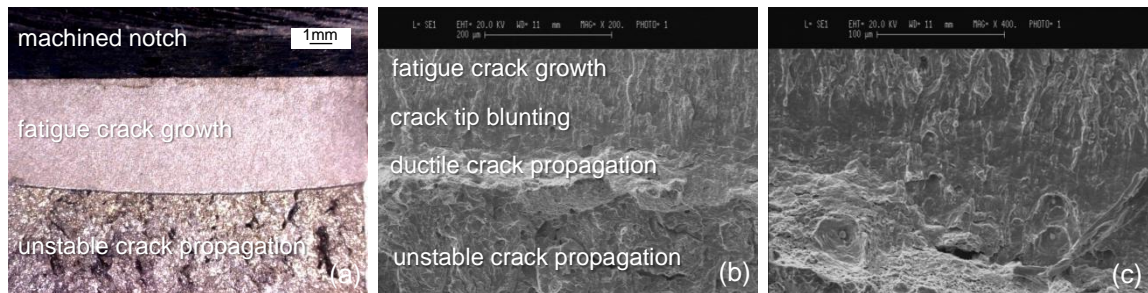


Figure 5.18. X65 steel: fracture surface morphology after toughness test at $T=-100^{\circ}\text{C}$ of uncharged specimens in (a) macro, and (b, c) micrographic observation

Figure 5.18 shows a short stable propagation and a wide unstable fracture surface. This is due to the high toughness value of the hydrogen-free material. Dimples are present (Figure 5.18c) both in ductile crack zone and in blunting area. Dimples are particularly flat. The fracture morphology of another uncharged specimen, tested at $T=-70^{\circ}\text{C}$, is shown in Figure 5.19. At this temperature, unstable propagation didn't occur during toughness test but it was provided by embrittling the specimen with liquid nitrogen. This permit to perform an heat-tinting in order to highlight the different fracture zones.

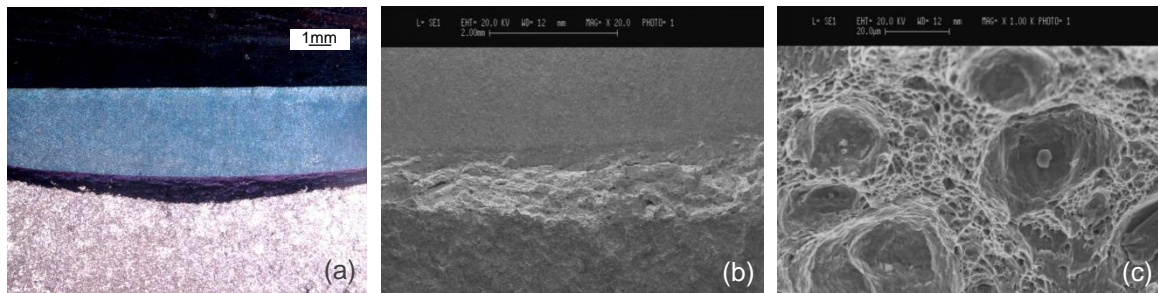


Figure 5.19. X65 steel: fracture surface morphology after toughness test at $T=-70^{\circ}\text{C}$ of uncharged specimens in (a) macro, and (b, c) micrographic observation

The ductile propagation is clearly visible both in macro observation, (Figure 5.19a), and in micrographic image (Figure 5.19b). Dimples are also in this case present and a relatively wide ductile zone divides them from each other. For hydrogen charged specimens fracture appearance changes considerably. Fracture morphologies, of hydrogen charged specimen, tested at $T=-60^{\circ}\text{C}$, are shown in Figure 5.20.

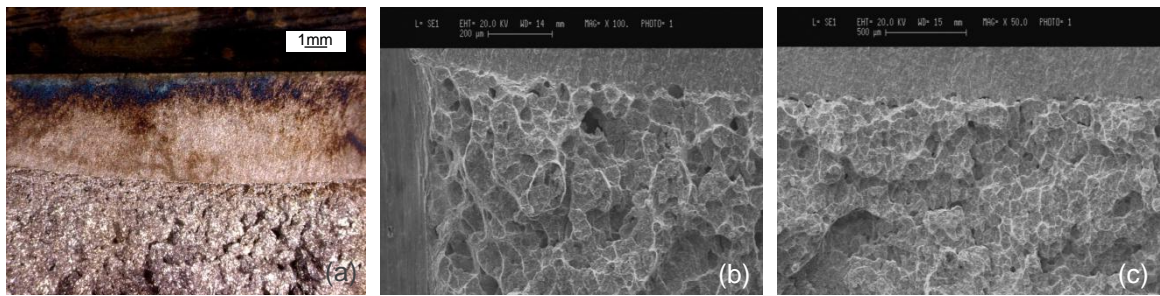


Figure 5.20. X65 steel: fracture surface morphology after toughness test at $T=-60^{\circ}\text{C}$ of charged specimens in (a) macro, and (b, c) micrographic observation

From macrographic image (Figure 5.20a) is difficult to distinguish stable from unstable propagation, due to the absence of heat-tinting. From mechanical data it is possible to estimate the ductile crack propagation of about one millimetre. After this value, instable crack propagation occurs. Crack tip blunting is practically absent. A wide area, in ductile propagation zone, both near the specimen edge (Figure 5.20b) and in the middle (Figure 5.20c), is characterized by “cellular” fracture morphology. A detail of “cellular” region is shown in Figure 5.21.

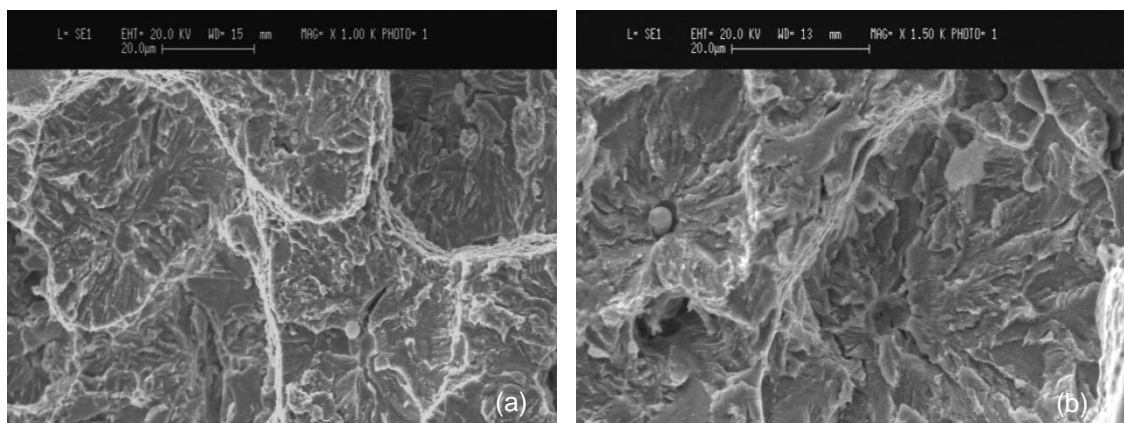


Figure 5.21. X65 steel: “cells” on fracture surface of specimen tested at (a) $T = -80^{\circ}\text{C}$ and (b) at $T = -70^{\circ}\text{C}$

It is possible to observe the decrease in ductile area on every “cell” edge and the quasi-cleavage fracture morphology in every “cell”.

5.3 Fatigue crack growth test (fractographic analysis)

5.3.1 Macro and micrographic examination: F22 steel

An overview of mechanical tests and the corresponding macrographic observations, is shown in Figure 5.22; every specimen is marked by a proper code.

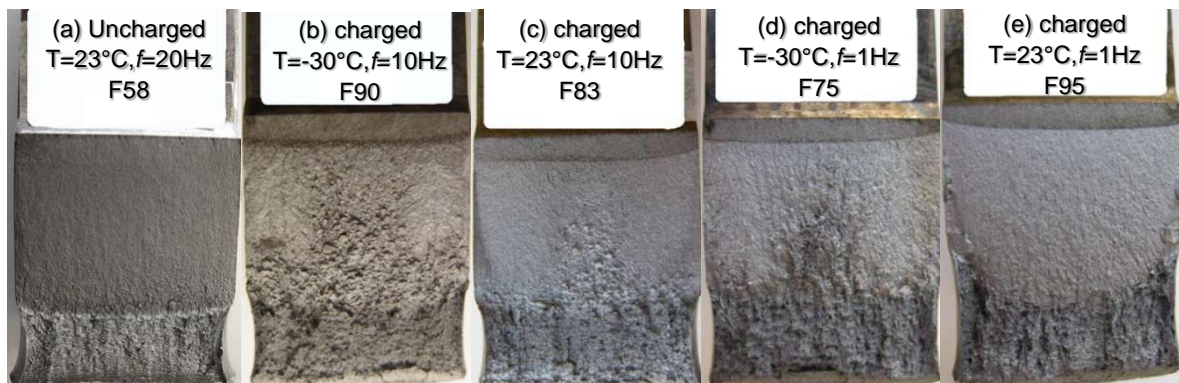
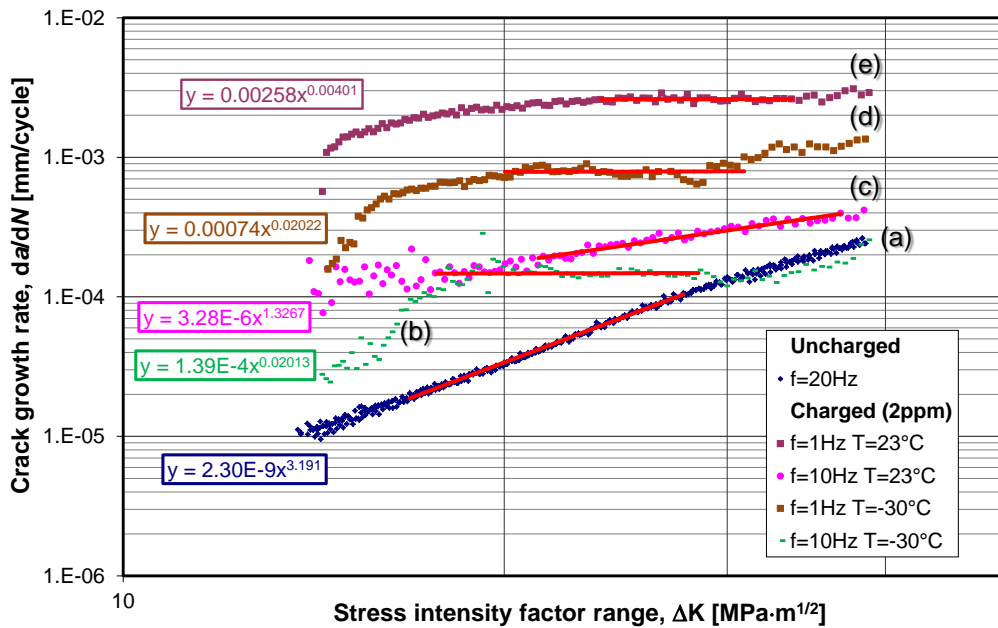


Figure 5.22. F22 steel: fatigue crack growth test and corresponding macrographic observation

Uncharged specimen shows the typical flat fracture surface up to the unstable propagation, when the critical J value is reached. Only one charged specimen, the F95, tested at $T=23^{\circ}\text{C}$ and $f=1\text{Hz}$, shows a macroscopic fracture surface similar to the uncharged ones, whereas the other charged specimens exhibit coarse area and also apparently flat zones. Anyway, by better observing specimen F95 it is possible to see rugged edges, absent in uncharged specimen. F90, F83 and F75 show two different fracture features: the first zone, smaller, is close to the machined notch and the second one, wider, extends up to the unstable propagation area; at this border an increase in crack growth velocity is observed from the mechanical tests. Typical fracture surfaces of uncharged specimen is reported in Figure 5.23.

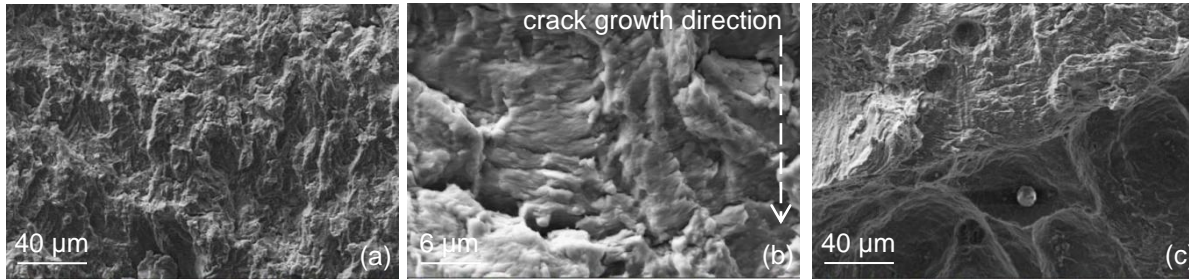


Figure 5.23. F22 steel: fracture surface morphology after fatigue test at $T=23^{\circ}\text{C}$ and $f=20\text{Hz}$ of uncharged specimen in mid-thickness at (a) $a_0+9\text{mm}$, (b) a detail of the area and (c) in the transition zone

The fracture surface, of uncharged specimen, is flat and shows striations mainly perpendicular to the crack growth direction (Figure 5.23a and Figure 5.23b). A detail of an inclusion, observed in the final test area, is reported in Figure 5.23c.

The first fracture surface part of F83 specimen is shown in Figure 5.24. The observation is carried out in the mid-thickness, at a distance of 2mm from the precrack tip, whereas in Figure 5.25 the specimen edge is investigated.

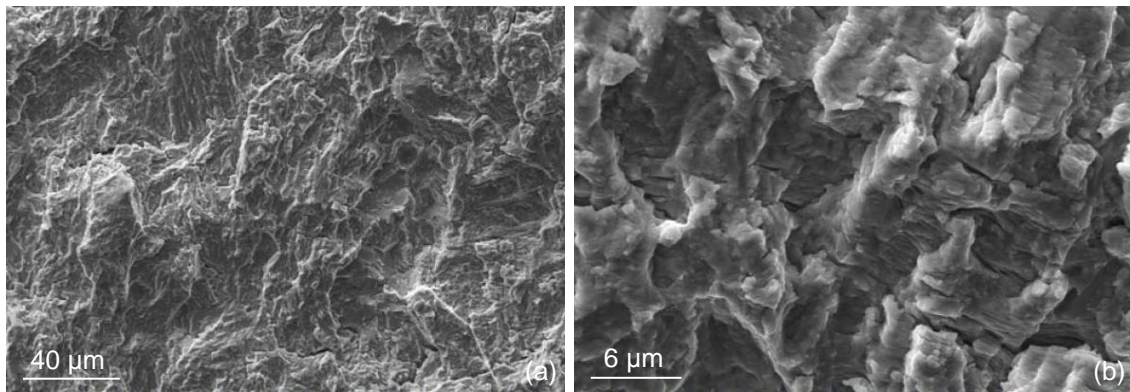


Figure 5.24. F22 steel: (a) fracture surface morphology after fatigue test at $T=23^{\circ}\text{C}$ and $f=10\text{Hz}$ of charged specimen in mid-thickness at $a_0+2\text{mm}$ and (b) a detail of the area

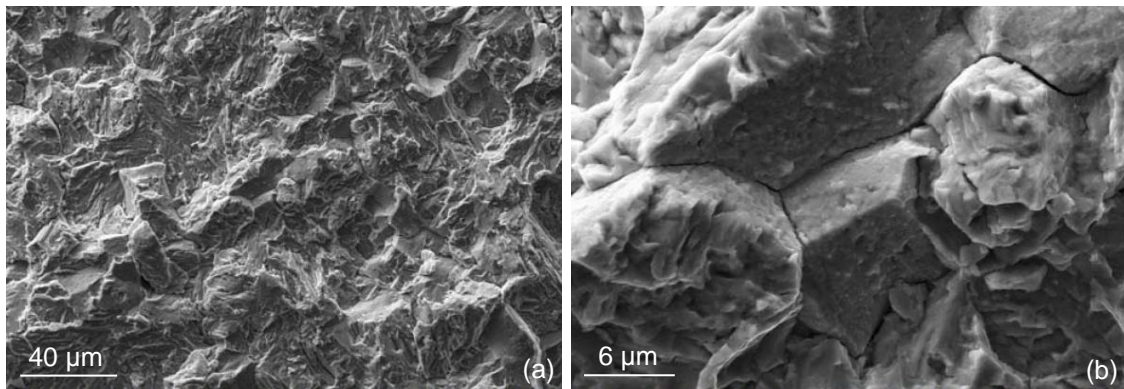


Figure 5.25. F22 steel: (a) fracture surface morphology after fatigue test at $T=23^{\circ}\text{C}$ and $f=10\text{Hz}$ of charged specimen at 1/4 of the thickness and $a_0+2\text{mm}$ and (b) a detail of the area

Clear brittle intergranular fracture is shown in Figure 5.25a and Figure 5.25b.

It is possible to observe that the embrittlement effect is predominant on the edge of the specimen; this is noticeable from the macrographic image also. With the crack progress, embrittling effect becomes more pronounced and “cellular” fracture appear both in the middle and at the edges of the specimen. Details of the fracture surface, in correspondence of a crack length equal to $a_0+8\text{mm}$, is shown in Figure 5.26.

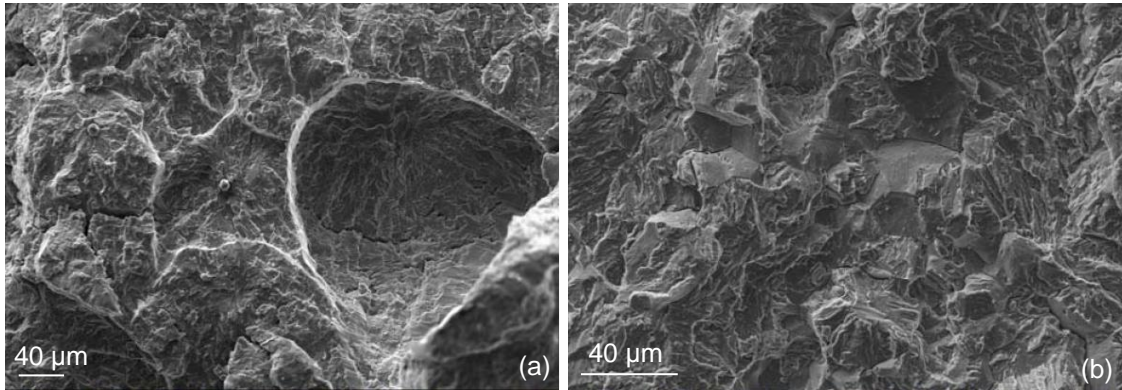


Figure 5.26. F22 steel: fracture surface morphology after fatigue test at $T=23^\circ\text{C}$ and $f=10\text{Hz}$ of charged specimen at $a_0+8\text{mm}$ in (a) mid-thickness and (b) at $1/4$ of the thickness

It is observable the presence of “cells” at half-thickness (Figure 5.26a) and partially intergranular separations near the edges (Figure 5.26b).

Reducing the frequency from $f=10\text{Hz}$ to $f=1\text{Hz}$ an increase of brittle areas, and consequently an increase in crack growth rate, occurs. A detail of the fracture surface near the notch, for a charged specimen tested at $T=23^\circ\text{C}$ and $f=1\text{Hz}$, is shown in Figure 5.27.

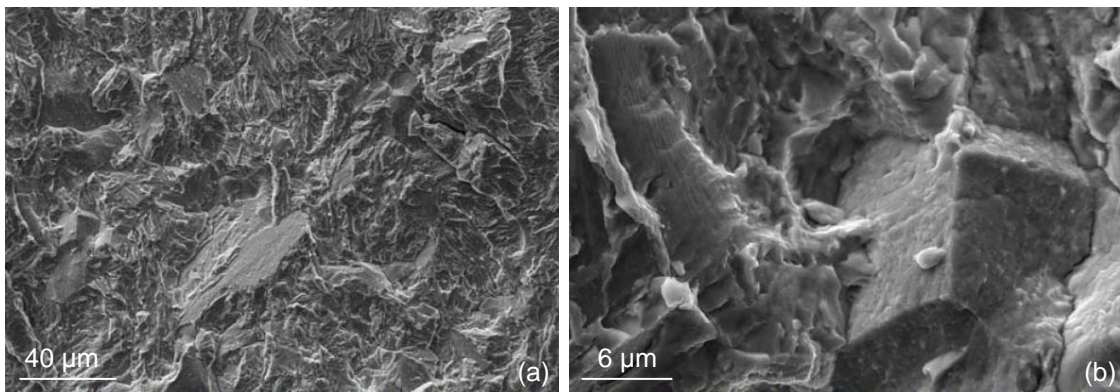


Figure 5.27. F22 steel: (a) fracture surface morphology after fatigue test at $T=23^\circ\text{C}$ and $f=1\text{Hz}$ of charged specimen at $a_0+2\text{mm}$ in mid-thickness and (b) a detail of the area

In correspondence of the most severe test conditions, the brittle zones and the intergranular fractures are increasing. In the final part of the fracture propagation it is possible to observe “cells” as shown in Figure 5.28.

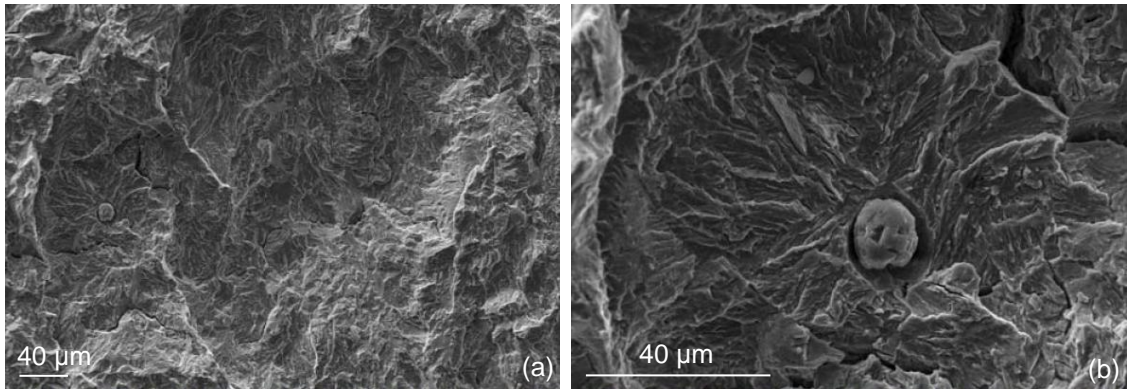


Figure 5.28. F22 steel: (a) fracture surface morphology after fatigue test at $T=23^{\circ}\text{C}$ and $f=1\text{Hz}$ of charged specimen at $a_0+13\text{mm}$ in mid-thickness and (b) a detail of the area

The inclusion and the quasi-cleavage fracture morphology, characteristic of the embrittled area close to the inclusions are evident in Figure 5.28b. The observation of specimens tested at lower temperature ($T=-30^{\circ}\text{C}$) gives the same results but less pronounced; this is due to the less amount of atomic hydrogen that reach the crack tip; due to the lower temperature, in fact, hydrogen diffusion in the material structure is lower.

It is still possible find evidence of brittle zones that occur like intergranular fracture or “cells”. In some area the embrittlement effect is pronounced. An example of heavily embrittled areas is shown in Figure 5.29.

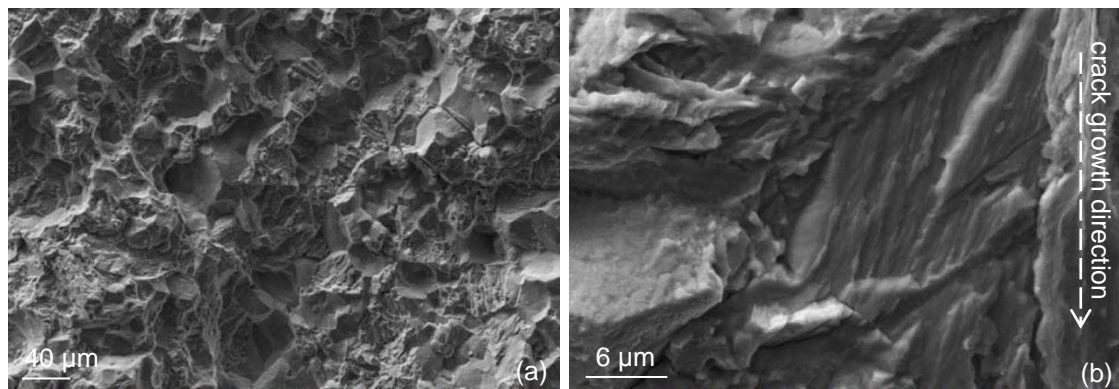


Figure 5.29. F22 steel: (a) fracture surface morphology after fatigue test at $T=-30^{\circ}\text{C}$ and $f=10\text{Hz}$ of charged specimen at $a_0+1\text{mm}$ in mid-thickness and (b) a detail of the area

Intergranular fractures (Figure 5.29a) occur during the first propagation phase and brittle striations (Figure 5.29b) take place parallel to the crack growth direction that is always from the top to the bottom of the image. Also “cellular” fracture morphologies occur; the fracture surface of a charged specimen tested at $T=-30^{\circ}\text{C}$ and $f=1\text{Hz}$ is reported in Figure 5.30. The morphology is full of different features but, in particular, it is possible to see the different planes where “cells” arise (Figure 5.30a and Figure 5.30b).

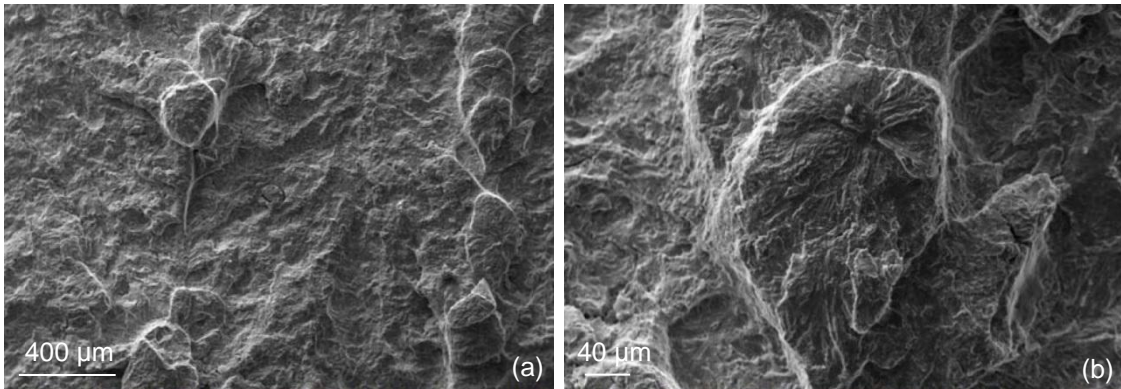


Figure 5.30. F22 steel: (a) fracture surface morphology after fatigue test at $T=-30^{\circ}\text{C}$ and $f=1\text{Hz}$ of charged specimen at $a_0+4\text{mm}$ in mid-thickness and (b) a detail of the area

5.3.2 Macro and micrographic examination: X65 steel

Figure 5.31 shows an overview of mechanical tests and the corresponding macrographic observations of X65 specimens.

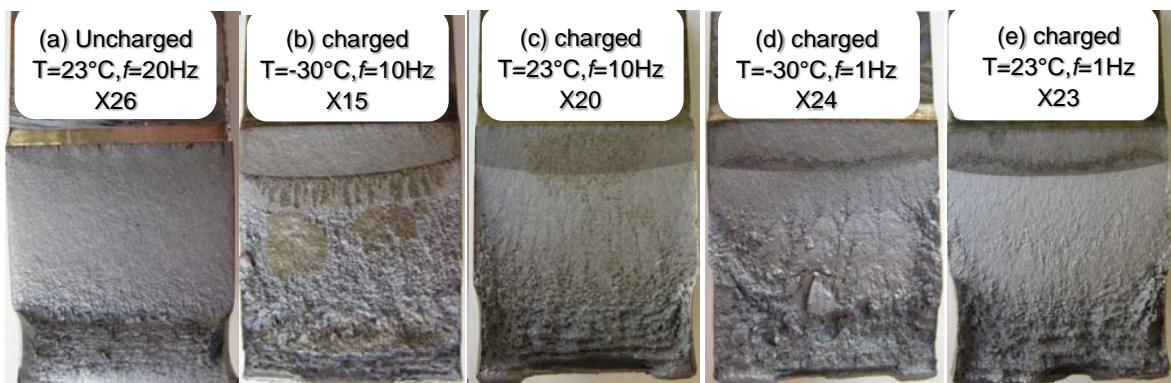
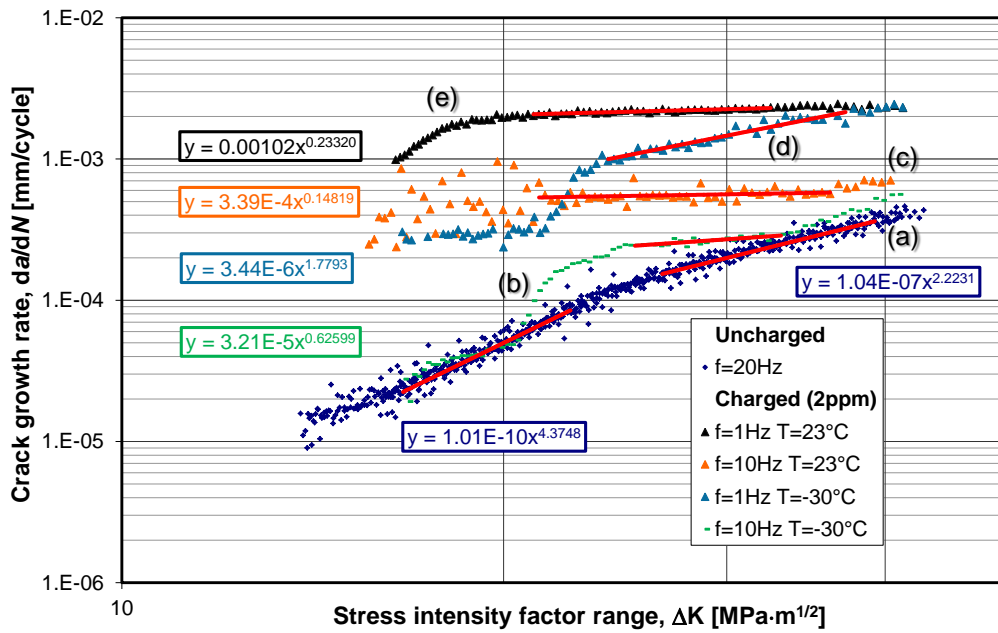


Figure 5.31. X65 steel: fatigue crack growth test and corresponding macrographic observation

The uncharged specimen, tested at $T=23^{\circ}\text{C}$ and $f=20\text{Hz}$, shows a typical flat fracture surface equal in morphology, both at the centre and at the edge, till the unstable crack propagation, when the J critical value is reached. Since created at the same frequency, it is difficult to distinguish between pre-crack and test-crack.

Hydrogen charged specimens, tested at room temperature, show a flat surface in the centre and a rougher zone at the edges. Specimens charged and tested at $T=-30^{\circ}\text{C}$ show two distinct fracture zones. The first is almost flat but the second, wider, present a very ruined surface. The boundary between these areas correspond to an increase in crack growth velocity, observed by mechanical tests in proximity of a suddenly increase of the slope in the fatigue crack growth diagram (Figure 5.31).

A micrographic observation of the uncharged specimen is shown in Figure 5.32.

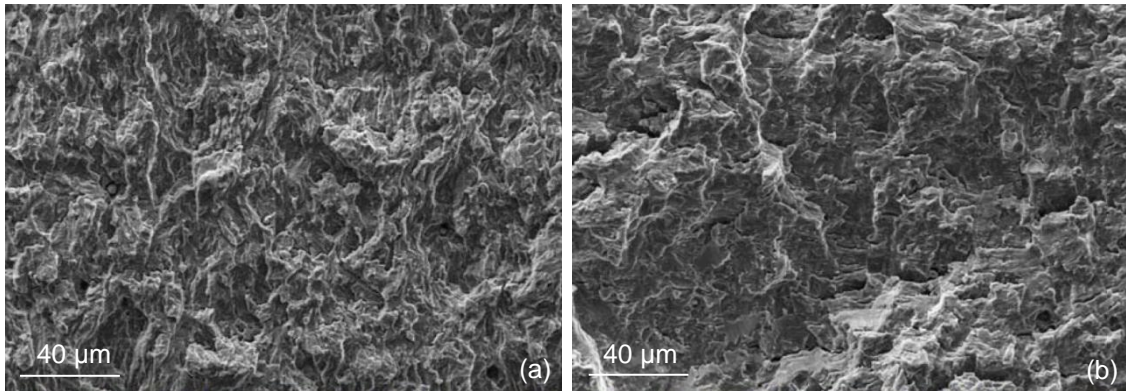


Figure 5.32. X65 steel: fracture surface morphology after fatigue test at $T=23^{\circ}\text{C}$ and $f=20\text{Hz}$ of uncharged specimen in mid-thickness at (a) $a_0+1.5\text{mm}$ and (b) $a_0+11.5\text{mm}$

The fracture surface is more irregular at lower ΔK and more flat near higher ΔK values. An inclusion is shown in Figure 5.32a; the fracture propagation is not affected by the inclusion presence. A detail of the previous area is shown in Figure 5.33.

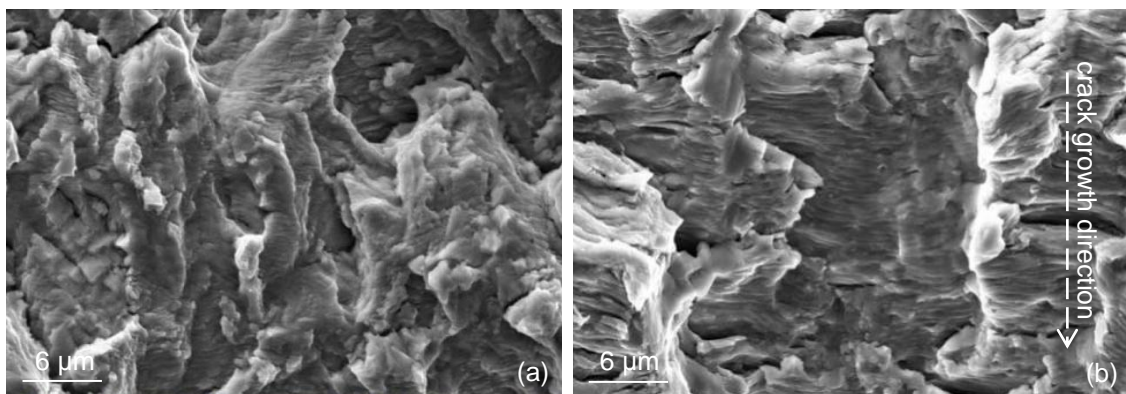


Figure 5.33. X65 steel: fracture surface morphology after fatigue test at $T=23^{\circ}\text{C}$ and $f=20\text{Hz}$ of uncharged specimen in mid-thickness; presence of striations at (a) $a_0+1.5\text{mm}$ and (b) $a_0+11.5\text{mm}$

In correspondence of low ΔK values and small crack propagation rates, striations are close to each other (Figure 5.33a), whereas, for long crack, high ΔK values, distance between them increases (Figure 5.33b). Striations are always created in the macroscopic crack growth direction.

Good similarity was found between crack growth velocity, assessed by mechanical test, and that obtained by knowing the distance between striations. Typical inclusions, found in uncharged specimens, are shown in Figure 5.34.

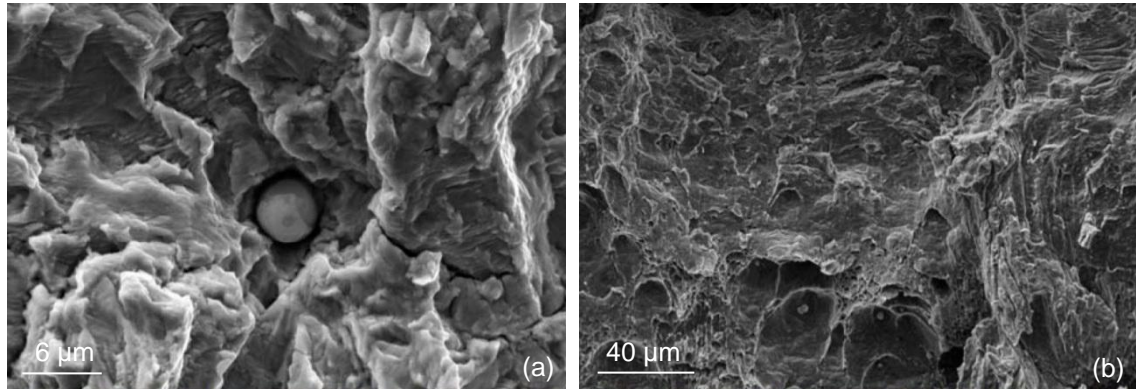


Figure 5.34. X65 steel: fracture surface morphology after fatigue test at $T=23^{\circ}\text{C}$ and $f=20\text{Hz}$ of uncharged specimen in mid-thickness; presence of inclusions at (a) $a_0+2\text{mm}$ and (b) $a_0+12.5\text{mm}$

In uncharged specimens, propagation crosses inclusions without generating particular fracture zones around them (Figure 5.34a); striations are present and perpendicular to the crack growth direction and they are still visible close to the inclusions. At very high ΔK values, just before the unstable propagation, dimples are generated around every inclusion (Figure 5.34b).

Fracture surfaces of hydrogen charged specimens are very different from those of uncharged specimens.

Fracture morphology of a charged specimen, tested at $T=23^{\circ}\text{C}$ and $f=10\text{Hz}$, is shown in Figure 5.35.

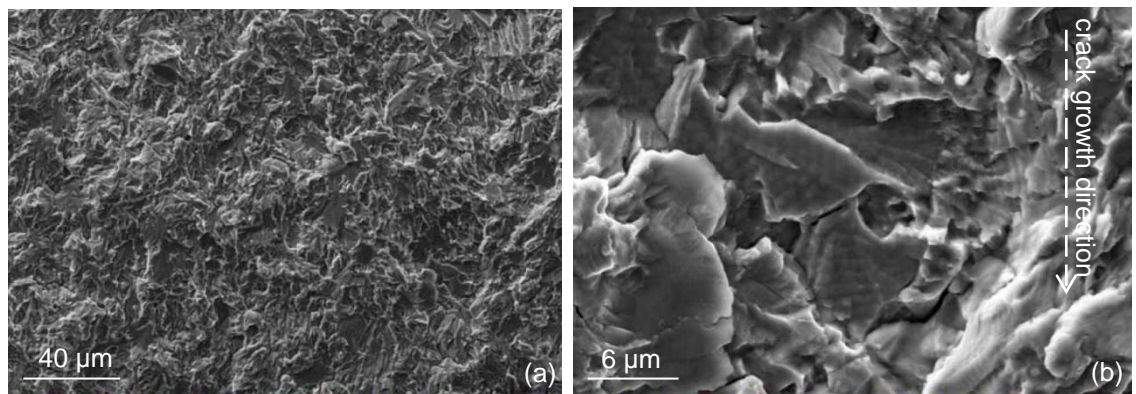


Figure 5.35. X65 steel: (a) fracture surface morphology after fatigue test at $T=23^{\circ}\text{C}$ and $f=10\text{Hz}$ of charged specimen in mid-thickness at $a_0+2\text{mm}$ and (b) a detail of the area

The surface, in this first zone, is very flat but shows brittle fracture features (Figure 5.35a). From a detail of this area (Figure 5.35b) it is possible to observe brittle fracture planes and striations over these flat zones. Striations, in particular, are oriented in different directions and smooth respect those observed in uncharged specimens. Similar evaluations are presented by Murakami [20]. As an example, differences between striations occurred in charged and uncharged specimen, are shown in Figure 5.36.

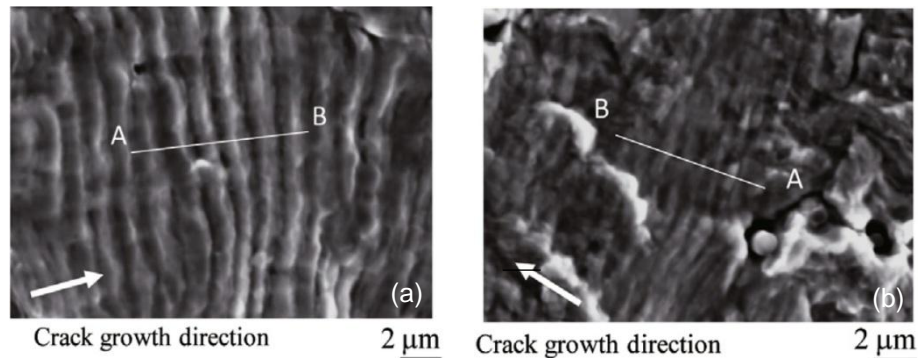


Figure 5.36. Difference in striation morphology between a hydrogen charged specimens and uncharged specimens: (a) uncharged and (b) charged [20]

Around the end of the propagation, fracture becomes partially “cellular”, as reported in Figure 5.37.

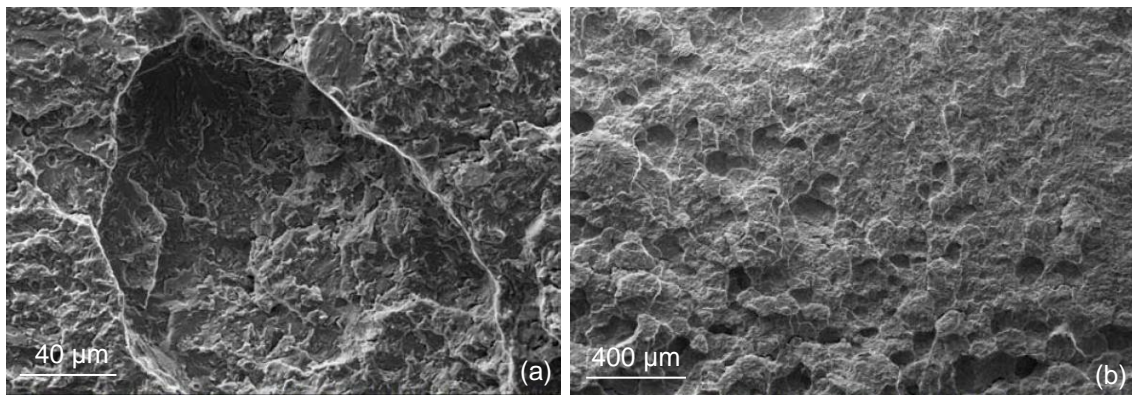


Figure 5.37. X65 steel: fracture surface morphology after fatigue test at $T=23^{\circ}\text{C}$ and $f=10\text{Hz}$ of charged specimen in mid-thickness at (a) $a_0+7.5\text{mm}$ and (b) at $a_0+9.5\text{mm}$

A typical “cell” is shown in Figure 5.37a; it is possible to observe the inclusion imprint at the top and the “cell” extension downward. In Figure 5.37b a “cells” cluster, taken at higher magnification, is shown. On the specimen edge, fracture morphology is the same but starts closer to the precrack tip. Charged specimen, tested at $T=23^{\circ}\text{C}$ and $f=1\text{Hz}$, presents similar macrographic (Figure 5.31) and micrographic morphology of the specimen tested at same temperature and $f=10\text{Hz}$, then, flat surface, brittle fracture plane in the first part, “cellular” fracture at the edge and toward the fatigue crack end. Anyway, striations are less or completely absent, identifying the more brittle behaviour also observed by mechanical tests.

Due to the more embrittling behaviour, inclusions don't play a particular part in the fracture propagation morphology. In Figure 5.38 the micrographic morphology of the charged specimen tested at $T=23^{\circ}\text{C}$ and $f=1\text{Hz}$ is shown.

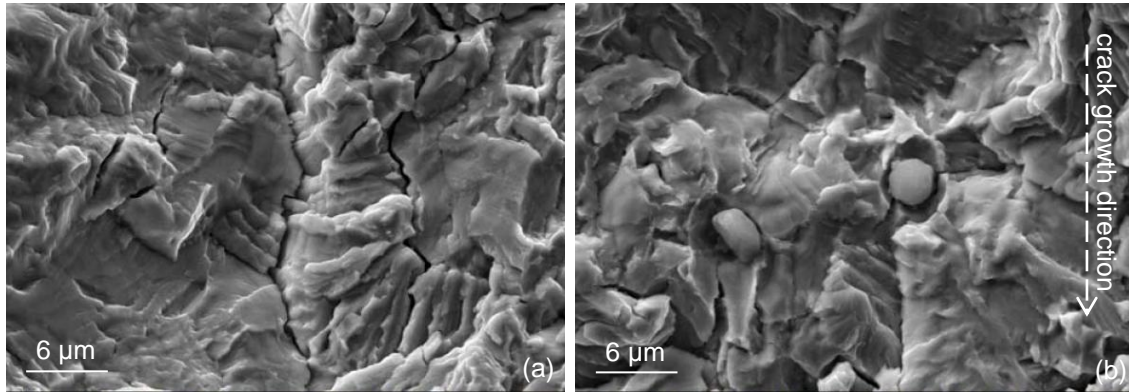


Figure 5.38. X65 steel: fracture surface morphology after fatigue test at $T=23^{\circ}\text{C}$ and $f=1\text{Hz}$ of charged specimen in mid-thickness at (a) $a_0+4\text{mm}$ and (b) an inclusion at $a_0+4\text{mm}$

Secondary cracks, perpendicular to the main propagation, are observed (Figure 5.38a). Propagation goes straight without taking into account inclusions presence; striations are not always oriented to the main propagation trend (Figure 5.38b). “Cellular” morphology and also secondary perpendicular cracks, are present close to the end of the fatigue propagation (Figure 5.39).

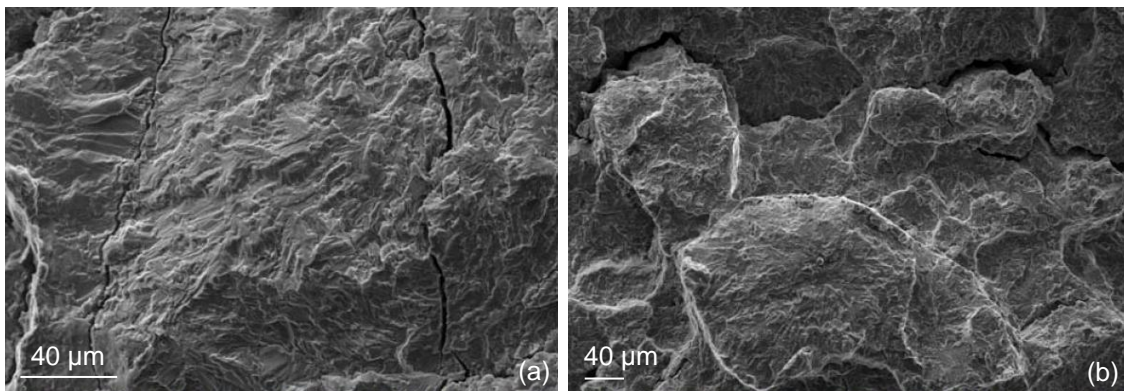


Figure 5.39. X65 steel: fracture surface morphology after fatigue test at $T=23^{\circ}\text{C}$ and $f=1\text{Hz}$ of charged specimen in mid-thickness at $a_0+7\text{mm}$

Fracture surfaces of the specimen tested at $T=-30^{\circ}\text{C}$ present a completely different macrographic (Figure 5.31) and micrographic morphology from those tested at room temperature. The first band, where propagation velocity is lower as evaluated from mechanical tests, is of about 3mm wide and presents flat morphology; after this zone, velocity increases rapidly and a coarser area appears. This behaviour is similar both for X15 and for X24. X24 presents a wider flat zone.

Micrographic observation of X15 reveals a first flat zone shown in Figure 5.40.

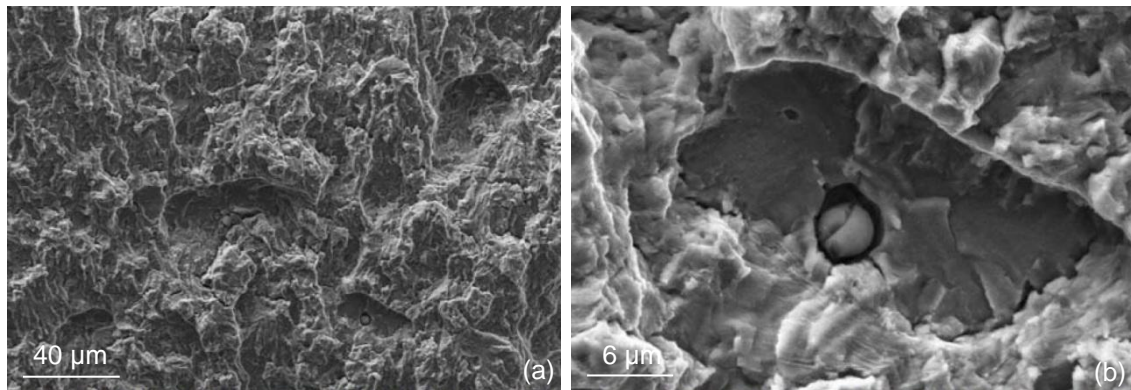


Figure 5.40. X65 steel: (a) fracture surface morphology after fatigue test at $T=-30^{\circ}\text{C}$ and $f=10\text{Hz}$ of charged specimen in mid-thickness at $a_0+1\text{mm}$ and (b) a detail of the area

The lower amount of “cells” denotes the lower brittle behaviour noticed by mechanical data. At higher ΔK , when the acceleration occurred, “cellular” fracture appears. In Figure 5.41 the fracture surface of X15 specimen is reported.

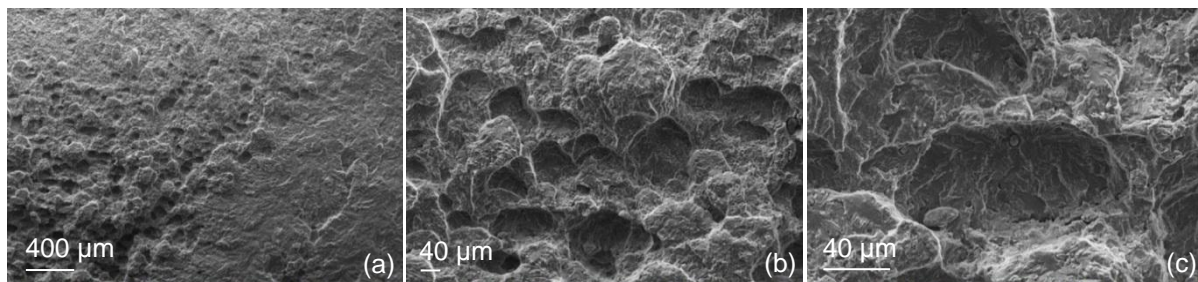


Figure 5.41. X65 steel: (a) fracture surface morphology after fatigue test at $T=-30^{\circ}\text{C}$ and $f=10\text{Hz}$ of charged specimen in mid-thickness at $a_0+4\text{mm}$ and (b, c) details of the area

Figure 5.41a shows a part of the brittle zone also seen in macrographic image (Figure 5.31).

5.4 Considerations on fracture surfaces and predicting model

Fractographic observations, conducted on CT specimen for J-integral and fatigue crack growth tests, give interesting results. It appears that one of the main difference between hydrogen charged and uncharged specimens is the presence of facet-like features, indicating reduced plasticity at low stress level. Cell-like features are observable at high stress level and present both a quasi-cleavage morphology and a plastic response around the cell, showing that the material has still some plastic reserve available. Hence, both brittle and plastic features are present in H-charged material fracture surface indicating that the superposition model has a physical justification. Indeed, it appeared that fatigue crack growth ratio is enhanced by hydrogen but there is always a constrain owing to plastic reserve in the material.

An interesting comparison in void nucleation and growth is given by Murakami [20] and depicted in Figure 5.42. Referring to hydrogen embrittle models, given in chapter 2, hydrogen interacts with void nucleation and growth by segregating around the inclusion, where both stresses and dislocations concentration are higher, affecting the material behaviour and reducing its ability to flow. Feature in Figure 5.42 resembles cell morphology and can be a good explanation of the phenomenon. Figure 5.43 shows a schematization of striations formation in hydrogen charged and uncharged material. Firstly, it can be observed that hydrogen is segregated at crack tip where hydrostatic stresses are high (as explained in chapter 2), concentration ahead of the crack is then increased respect to the bulk material. Secondly, hydrogen effect lies in reducing plasticity by reducing crack blunting, as it can be seen by comparing the two cases. In this way, hydrogen enhances the crack growth since Δa is larger in hydrogen presence than in uncharged material. Hydrogen, by lowering plasticity of the material, reduces also striations formation: indeed, if Figure 5.33b is compared with Figure 5.35b, it can be observed that striations, in presence of hydrogen, are less clear and crests are less marked.

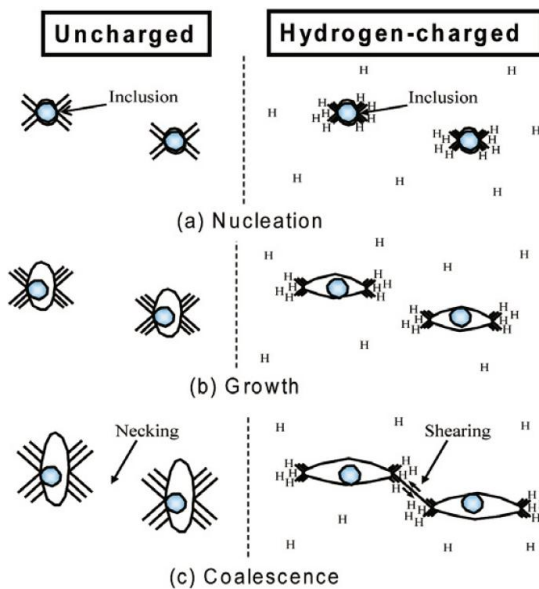


Figure 5.42. Schematic illustration of nucleation, growth and coalescence of voids with and without hydrogen in metals [20]

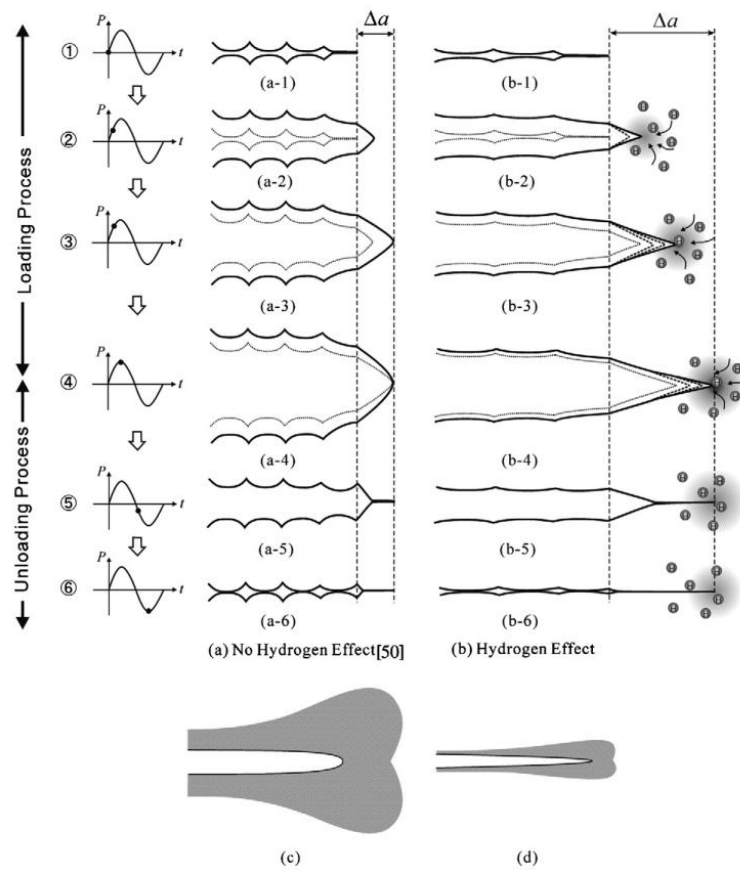


Figure 5.43. Crack tip opening and striation formation mechanism in fatigue: (a) no hydrogen effect, (b) hydrogen effect, (c) schematic effect of thick plastic zone wake produced at crack tip under no hydrogen and (d) schematic image of shallow plastic zone wake produced at a crack under hydrogen effect [20]

Another feature, observed clearly in FCG tests is the facet-like morphology in charged material fracture surfaces; in this case and according to $da/dN-\Delta K$ plot a large scatter of data was observed, indeed, it is not easy to assess the reason of this scattering but of course the jump-like growth is probable to be responsible.

In conclusion, it is not easy to assess surely by fractographic analysis the mechanism governing the cracking, nevertheless a main feature emerges: cracking in presence of hydrogen proceeds both by brittle and ductile mode and propagation occurs by jumps of brittle material that are constrained by plastic reserve. This fact underlines the diffusion dependence of the phenomenon and justifies the plateau rate.

The predicting model, shown in chapter 4, appears to be in accordance with micro observations. Nevertheless it should always be kept in mind that too daring conclusions are far to be drawn from few fractographic investigation and this chapter is useful for a first insight on IHAC micromechanics.

Conclusions

In this thesis work the fracture-mechanical properties of two steels widely used in oil pipeline have been investigated in a wide temperature range and with and without the presence of hydrogen in the material lattice.

From first two chapters, powerful tools and literature data were reported in order to clarify the phenomenon:

- “Sour” environments enhances the penetration of atomic hydrogen in the metal lattice.
- Hydrogen in the lattice is able to worsen mechanical and fatigue properties of steel, in particular in presence of sustained loads and fatigue crack growth, by reducing plasticity.
- A practical definition of HE was given and all its features (diffusion, kinetics and stress state) have been quantified and showed.
- Micromechanical models of hydrogen embrittlement were given.

In third chapter, experimental procedures and results from mechanical tests were given:

- Mechanical testing procedures were shown, for hydrogen charged and uncharged specimens, in order to obtain mechanical parameters regarding tensile, impact, toughness and fatigue behaviour, varying test temperature from room temperature until a value of about $T=-128^{\circ}\text{C}$.
- Hydrogen charged material showed a drastic change in the mechanical behaviour respect to the uncharged one.
- Hydrogen effect, as expected, is remarkably enhanced in those tests that require a long time to be performed, such as toughness tests, while it is lower in quick Charpy impact tests.
- In toughness tests a reduction in mechanical characteristics, up to 8 times bigger if compared to the uncharged one, has been observed. In particular the material loses the ability to plasticize under high loads and stresses, and its behaviour shifts to those of medium tough steels.
- In toughness tests, hydrogen effect, is not temperature dependent, maybe due to the absence of a pumping mechanism as in fatigue crack growth tests, in fact, also varying the test temperature, J_q values, experimentally obtained from charged specimens, are very similar: for F22 charged specimens $J_q \approx 150 \text{kJ/m}^2$ and for X65 $J_q \approx 90 \text{kJ/m}^2$.

- Toughness tests were carried out on charged specimens left at room temperature and open environment for 24 hours, in order to allow the hydrogen diffusion from the specimen. In this case, only diffusible hydrogen at room temperature can leave the lattice, whereas some hydrogen atoms remain still trapped in the material. It was observed, in fact, that also in this case, an embrittling effect, although lower, is present.
- Even though mechanical characteristics of the investigated steels are decreased in hydrogen presence, toughness properties remain relatively high thanks to the high quality of the materials.
- Fatigue crack propagation tests were performed on uncharged specimens to establish Paris law parameters: F22 shows a typical fatigue behaviour of steels with an exponent $m \approx 3.2$; changes in test temperature do not influence fatigue behaviour; X65 shows a different behaviour with a slope change in the II region around $\Delta K \approx 25 \text{ MPa}\sqrt{\text{m}}$. For $\Delta K < 25 \text{ MPa}\sqrt{\text{m}}$, $m \approx 4.4$, and for $\Delta K > 25 \text{ MPa}\sqrt{\text{m}}$, $m \approx 2.2$; changes in load frequency do not influence fatigue behaviour.
- Fatigue crack propagation tests were carried out on hydrogen charged specimens. Hydrogen effect was clearly observed and influenced by load frequency and temperature. The most important parameters are the hydrogen time permanence around the crack tip and the amount of hydrogen incoming from closer areas; low frequencies allow to a bigger hydrogen atoms quantity to migrate at the crack tip; as consequence, hydrogen embrittlement effect and crack growth rate, are enhanced. Low temperature affects the hydrogen diffusion in the steel reducing the mobility of hydrogen in the lattice, and, therefore, the embrittling effect.
- The crack growth rate curve is less dependent (lower m value) or even independent on ΔK , as a matter of fact most of the fatigue curves of hydrogen charged materials have a well-defined horizontal plateau;

A model, that takes into account experimental variables, able to predict the fatigue behaviour of steels in hydrogen presence, have been proposed:

- Crack growth rate, in hydrogen charged material, is the sum of two contributions: one named “mechanical”, that depends on applied loads, and a second one due to hydrogen effect. When crack growth rate increases, the “mechanical” contribution prevails because hydrogen atoms do not have enough time to accumulate at the crack tip: as a consequence crack growth rate is no longer hydrogen dependent.
- The model gives good results and complies satisfactorily the experimental data. Model is applied to real fatigue cases in pipeline, showing the simplicity in application and the usefulness.

Finally, macro and micrographic analyses are carried out onto fracture surfaces of C(T) specimens used for toughness and fatigue tests and CV specimens for impact tests.

In several cases, observations, show that in presence of hydrogen there is a clear change in fracture morphology and that plasticity is reduced in different manners. Moreover, experimental evidences regarding notions shown in chapter 2 were found.

- Fracture morphology, in hydrogen absence, is typical for steels. Fracture is ductile and characterized by the presence of striations which distance is well related to crack velocity measured during mechanical tests. Striations are perpendicular to the propagation direction. Dimples are present in the stable propagation areas and cleavage or quasi-cleavage morphology in unstable propagation zones.
- In hydrogen presence, fracture morphology presents facets and cell-like structure indicating a reduction of plasticity due to hydrogen effect; nevertheless, a partial plastic reserve is available for the material, in fact, around facets and "cells", plasticized areas were observed.
- Cellular fracture is considered a "less brittle" failure mode if compared with intergranular and brittle facets modes; this fracture behaviour is always present on the edges of the specimen, where stress triaxiality is lower, and in the transition area between fatigue and unstable propagation, where crack growth rate is higher. Moreover, it is present in some specimen on the fracture axis, maybe due to the fact that in this area a lower hydrogen concentration is expected due to the migration of the charged hydrogen to the specimen edges.
- Fracture micro-mechanisms have been proposed according to bibliography and they seem to correctly interpret the phenomenon.

ACKNOWLEDGEMENTS

I would like to thank ENI Exploration & Production Division, for having supported the research, Tenaris and Ringmill for the supplied materials and Centro Sviluppo Materiali S.p.A. for the cooperation in experimental tests (hydrogen measurements).

Bibliography

- [1] S.P. Lynch, Progress towards understanding mechanisms of hydrogen embrittlement and stress corrosion cracking. *Proceedings of the NACE Corrosion 2007 Conference & Expo*, Nashville, Tennessee, March 2007, paper 07493.
- [2] R.P. Gangloff, Hydrogen assisted cracking of high strength alloys, in: I. Milne, R.O. Ritchie and B. Karahaloo (Ed.), *Comprehensive Structural Integrity (Vol. 6)*, Elsevier Science, New York, 2003, pp. 31-101.
- [3] W.C. Lyons, *Standard handbook of petroleum and natural gas engineering (Vol. 1)*, Gulf Professional Publishing, Houston, 1996.
- [4] National Association of Corrosion Engineers NACE MR0175, Petroleum and natural gas industries - Materials for use in H₂S - containing environments in oil and gas production, Parts 1, 2 and 3 (Identical to ISO 15156-1:2009, 15156-2:2009 and 15156-3:2009), 2009.
- [5] M.W. Braestrup, J.B. Andersen, *Design and Installation of Marine Pipelines*, Wiley-Blackwell, Oxford, 2005.
- [6] S. Eliassen, L. Smith, *Guidelines on Materials Requirements for Carbon and Low Alloy Steels for H₂S-Containing Environments in Oil and Gas Production (3rd Edition)*, Maney Publishing, Leeds, 2009.
- [7] T.K. Govind, Hydrogen Damage of Metallic Materials: Introduction, Importance of hydrogen damage, Classification of hydrogen damage, Control of hydrogen damage, References. <http://knol.google.com/k/hydrogen-damage-of-metallic-materials#>
- [8] W.T. Becker, R.J. Shipley, *Failure Analysis and Prevention - Hydrogen Damage and Embrittlement*, Vol 11, ASM Handbook, ASM International, 2002.
- [9] R.D. Kane, M.S. Cayard, *Roles of H₂S in the Behaviour of Engineering Alloys: a Review of Literature and Experience*. CORROSION, 1998, Paper 274.
- [10] R.D. Kane, *Corrosion in Petroleum Refining and Petrochemical Operations, Corrosion: Environments and Industries*, Vol 13C, ASM Handbook, ASM International, 2006, pp. 967-1014.
- [11] K. Kowano, Recent Activities on High Temperature Hydrogen Attack. *Paper to be published*.
<http://www.nde.com/Recent%20Activities%20HTHA%20by%20Kawano.pdf>
- [12] R. Heidersbach, B. Heidersbach, *Metallurgy and Corrosion Control in Oil and Gas Production*, John Wiley & Sons Inc, New Jersey, 2011.
- [13] R. Mostert, Low Temperature Hydrogen Damage Assessment in the Gas and Refining Industries. *Proceedings of the Middle East Nondestructive Testing Conference & Exhibition*, Bahrain, Manama, November 2005.
- [14] BP International Limited GS 136-1, Materials for Sour Service, 1997.
- [15] A.L. Kohl, R.B. Nielsen, *Gas Purification (5th ed.)*, Gulf Publishing Company, Houston, 1997.

- [16] G.A. Antaki, *Piping and Pipeline Engineering: Design, Construction, Maintenance, Integrity and Repair*, Marcel Dekker, New York, 2003.
- [17] H.H. Jonhson, Keynote Lecture: Overview on Hydrogen Degradation Phenomena, in: R. Gibala, R.F. Hehemann (Ed.), *Hydrogen Embrittlement and Stress Corrosion Cracking*, American Society for Metals, Ohio, 1980, pp. 3-24.
- [18] J. Capelle, J. Gilgert, G. Pluinage, Hydrogen effect on fatigue and fracture of pipelines. *Proceeding of the thirteenth International Colloquium Mechanical Fatigue of Metals ICMFM XIII*, Ternopil, September 2006.
- [19] C.F. Dong, Z.Y. Liu, X.G. Li, Y.F. Cheng, Effects of hydrogen-charging on the susceptibility of X100 pipeline steel to hydrogen-induced cracking. *International Journal of Hydrogen Energy*, 34 (2009), pp. 9879-9884.
- [20] Y. Murakami, S. Matsuoka, Effect of hydrogen on fatigue crack growth of metals. *Engineering Fracture Mechanics*, 77 (2010), pp. 1926-1940.
- [21] H.J. Grabke, E. Riecke, Absorption and diffusion of hydrogen in steels. *Materiali in tehnologije*, 34 (2000), pp. 331-341.
- [22] J. Woodtli, R. Kieselbach, Damage due to Hydrogen Embrittlement and Stress Corrosion Cracking. *Engineering Failure Analysis*, 7 (2000), pp. 427-450.
- [23] D.V. Ragone, *Thermodynamics of Materials (Vol. II)*, John Wiley and Sons, New York, 1995.
- [24] L.S. Darken, R.P. Smith, *Behavior of hydrogen in steel during and after immersion in acid*. CORROSION, 1949, pp. 1-16.
- [25] R.D. McCright, Effects of environmental species and metallurgical structure on the hydrogen entry into steel, in: R.W. Staehle (Ed.), *Stress corrosion cracking and hydrogen embrittlement of iron base alloys*, NACE, Houston, 1977, pp. 306-325.
- [26] A.J. Kumnick, H.H. Jonhson, Deep trapping state for hydrogen in deformed iron. *Acta Metallurgica*, 28 (1980), pp. 33-39.
- [27] A. McNabb, P.K. Foster, *Trans. TMS-AIME*, 227 (1963), p. 618.
- [28] R.A. Oriani, The diffusion and trapping of hydrogen in steel. *Acta Metallurgica*, 18 (1970), pp. 147-157.
- [29] R. Kirchheim, Revisiting hydrogen embrittlement models and hydrogen-induced homogeneous nucleation of dislocations. *Scripta materialia*, 62 (2010), pp. 67-70.
- [30] M. Dadfarnia, B.P. Somerday, P. Sofronis, I. M. Robertson, D. Stalheim, Interaction of Hydrogen Transport and Material Elastoplasticity in Pipeline Steels. *Journal of Pressure Vessel and Technology*, 131 (2009), pp. 1-13.
- [31] R.A. Oriani, P.H. Josephic, Equilibrium aspects of hydrogen-induced cracking of steels. *Acta Metallurgica*, 22 (1974), pp. 1065-1074.
- [32] J.C. Sobotka, R.H. Dodds Jr., P. Sofronis, Effects of hydrogen on steady, ductile crack growth: Computational studies, *International Journal of Solids and Structures*, 46 (2009), pp. 4095-4106.

- [33] F. Bolzoni, P. Fassina, G. Fumagalli, L. Lazzari, G. Re, Hydrogen charging of carbon and low alloy steel by electrochemical methods, *Proceedings of the European Corrosion Congress EUROCORN*, Moscow, September 2010.
- [34] R.A. Oriani, J.P. Hirth, M. Smialowski, *Hydrogen Degradation of Ferrous Alloys*, Park Ridge, New Jersey, 1985.
- [35] X.Q. Wu, I.S. Kim, Effects of Strain Rate and Temperature on Tensile Behaviour of Hydrogen-Charged SA508 Cl.3 Pressure Vessel Steel, *Materials Science and Engineering*, 348 (2003), pp. 309-318.
- [36] T. Zhang, W.Y. Chu, K.W. Gao, L.J. Qiao, Study on Correlation between Hydrogen-Induced Stress and Hydrogen Embrittlement, *Materials Science and Engineering*, 347 (2003), pp. 291-299.
- [37] Y. Murakami, *Metal Fatigue: Effects of Small Defects and Nonmetallic Inclusions*, Elsevier, Oxford, 2002.
- [38] F. Iacoviello, V. Di Cocco, Sintered stainless steels: Fatigue crack propagation resistance under hydrogen charging condition, *Corrosion Science*, 49 (2007), pp. 2099-2117.
- [39] V. Di Cocco, E. Franzese, F. Iacoviello, S. Natali, 22 Cr 5 Ni duplex and 25 Cr 7 Ni superduplex stainless steel: Hydrogen influence on fatigue crack propagation resistance, *Engineering Fracture Mechanics*, 75 (2008), pp. 705-714.
- [40] M.G. Hay, *Fit-for-Purpose Materials Testing for Sour Gas Service*. CORROSION 2000, Paper 139.
- [41] S. Serna, J.L. Albarran, R. Perez, *Effect of Hydrogen Sulfide Environments on the Cracking Susceptibility of Medium-Strength Microalloyed Pipeline Steels for Oil and Gas Transport*. CORROSION, 2003, Paper 530.
- [42] J.L. Albarran et al, *Corrosion and Cracking Behaviour of an API X80 Steel Exposed to Sour Gas Environments*. CORROSION, 2002, Paper 9.
- [43] S. Serna, A. Fragieli, *Effect of Different Microstructures and Strengths on the Cracking resistance of Microalloyed Pipeline Steels in Sour Environments*. CORROSION, 2006, Paper 654.
- [44] N. Hagiwara, N. Oguchi, *Fracture Toughness (CTOD) of Linepipe Materials under Cathodic Protection*. CORROSION, 1997, Paper 200.
- [45] P. Andrews, M. McQueen, N. Millwood, *Variation of the Fracture Toughness of a High-Strength Pipeline Steel under Cathodic Protection*. CORROSION, 2001, Paper 8.
- [46] M.F. Stevens, I.M. Bernstein, Microstructural Trapping Effects on Hydrogen Induced Cracking of a Microalloyed Steel, *Metallurgical Transactions*, 20A (1989), pp. 909-919.
- [47] K.E. Szklarz, J. Bowker, R. Orr, *Burst Test of a Vessel under Wet Sour Gas Conditions*. CORROSION, 1997, Paper 517.

- [48] H.I. McHenry, D.T. Read, T.R. Shives. Failure Analysis of an Amine-Absorber Pressure Vessel, *Materials Performance* 26 (1987), pp.18-24.
- [49] D. Hendrix et al., *Brittle Fracture of an Underground Gas Gathering Pipeline at ERW Weld Groove Defects under Hydrogen Charging Conditions and Wet CO₂/H₂S Corrosion*. CORROSION, 2002, Paper 101.
- [50] H.I. McHenry, D.T. Read, T.R. Shives, Failure Analysis of an Amine-Absorber Pressure Vessel, *Materials Performance*, 26 (1987), pp.18-24.
- [51] H. Nykyforchyn et al., Environmentally assisted “in-bulk” steel degradation of long term service gas trunkline, *Engineering Failure Analysis*, 17 (2010), pp. 624-632.
- [52] R. Wang, Effects of hydrogen on the fracture toughness of a X70 pipeline steel. *Corrosion science*, 51 (2009), pp. 2803-2810.
- [53] American Society of Mechanical Engineers ASME BPVC Section II SA-182, Specification for forged or rolled alloy-steel, pipe flanges, forged fittings and valves and parts for high-temperature service, 2004.
- [54] American Petroleum Institute API Specification 5L, Specification for Line Pipe, 2004.
- [55] American Society for Testing and Materials ASTM E 8/E 8M-08, Standard test methods for tension testing of metallic materials, 2008.
- [56] International Organization for Standardization ISO 148, Metallic materials - Charpy pendulum - impact test, 2009.
- [57] American Society for Testing and Materials ASTM E 23-07, Standard test methods for notched bar Impact testing of metallic materials, 2007.
- [58] American Society for Testing and Materials ASTM E 1820-09, Standard Test Method for Measurement of Fracture Toughness, 2009.
- [59] International Organization for Standardization ISO 3183, Petroleum and natural gas industries - Steel pipe for pipeline transportation systems - Second Edition, 2007.
- [60] J.F Newman, L.L. Shreir, Role of Hydrides in Hydrogen Entry into Steel from Solutions Containing Promoters, *Corrosion Science*, 9 (1977), pp. 631-641.
- [61] T. Ohtsubo, S. Goto, M. Amano, Development of Apparatus for Determination of Diffusible Hydrogen in Steel, *Transaction JISI*, 25 (1985), pp.21-29.
- [62] G. Green, F.J. Knott, Effects of Side Grooves on Initiation and Propagation of Ductile Fracture, *Met. Technol.* 2, 9 (1975), pp. 422-427.
- [63] A. Sciuccati, L'importanza dei side-grooves per lo stato di sforzo in provini per meccanica della frattura, *Proceedings of the 39th National Congress AIAS*, Maratea, Italy, September 2010.
- [64] L. Vergani, *Meccanica dei materiali (2nd ed.)*, McGraw-Hill, Milano, 2006.

- [65] P. Fassina, R. Morana, L. Alleva, G. Mortali, L. Vergani, A. Sciuccati, Materials behavior in extreme conditions: influence of large amounts of H₂S on steel toughness in low temperature environments. *Proceedings of the European Corrosion Congress EUROCORR*, Moscow, September 2010.
- [66] P. Fassina, A. Sciuccati, L. Vergani, L'effetto dell'idrogeno e della bassa temperatura sul comportamento meccanico di acciai ad alta resistenza. *Proceedings of the 39th National Congress AIAS*, Maratea, Italy, September 2010.
- [67] P. Fassina, F. Bolzoni, G. Fumagalli, L. Lazzari, L. Vergani, A. Sciuccati, Comportamento di acciai per tubazioni in condizioni estreme: presenza di H₂S e bassa temperatura. *Proceedings of the 33rd National Congress AIM*, Brescia, Italy, November 2010.
- [68] P. Fassina, F. Bolzoni, G. Fumagalli, L. Lazzari, L. Vergani, A. Sciuccati, Influence of hydrogen and low temperature on mechanical behaviour of two pipeline steels, *Engineering Fracture Mechanics*, 81 (2012), pp. 43-55.
- [69] T.L. Anderson, *Fracture mechanics: fundamentals and applications (3th ed.)*, Taylor & Francis, Boca Raton, 2005.
- [70] American Society for Testing and Materials ASTM E 647-08, Standard Test Method for Measurement of Fatigue Crack Growth Rates, 2008.
- [71] P. Fassina, F. Brunella, L. Lazzari, G. Re, L. Vergani, A. Sciuccati, Fatigue behavior of pipeline steel under hydrogen environment and low temperature, *Procedia Engineering*, 10 (2011), pp. 3353-3360.
- [72] P. Fassina, L. Vergani, L. Lazzari, F. Bolzoni, A. Sciuccati, Comportamento a fatica di acciai per pipeline soggetti ad infragilimento da idrogeno e basse temperature. *Proceedings of the 40th National Congress AIAS*, Palermo, Italy, September 2011.
- [73] T. Kanazaki, C. Narazaki, Y. Mine, S. Matsuoka, Y. Murakami, Effects of hydrogen on fatigue crack growth behavior of austenitic stainless steels, *International Journal of Hydrogen Energy*, 33 (2008), pp. 2604-2619.
- [74] M. Janssen, J. Zuidema, R.J.H. Wanhill, *Fracture mechanics (2nd ed.)*, VSSD, Delft, 2006.
- [75] R.P. Wei, Ming Gao, Reconsideration of the superposition model for environmentally assisted fatigue crack growth, *Scripta Metallurgica*, 17 (1983), pp. 959-962.
- [76] M. Knop, J. Heath, Z. Sterjovski, S.p. Lynch, Effects of cycle frequency on corrosion-fatigue crack growth in cathodically protected high-strength steels, *Procedia Engineering*, 2 (2010), PP. 1243-1252.
- [77] H.P. Van Leeuwen, Plateau velocity of SCC in high strength steels A quantitative treatment, *NACE Corrosion*, 31 (1975), pp. 42-50.
- [78] H.G. Nelson, D.P. Williams, Quantitative Observations of Hydrogen-Induced, SlowCrack Growth in a Low Alloy Steel, in: R.V. Staehle (Ed.), *Stress Corrosion Cracking and Hydrogen Embrittlement of Iron Base Alloys*, NACE, Houston TX, 1977, pp. 390-404.

- [79] A.J. Kunnick, H.H. Johnson, Deep trapping states for hydrogen in deformed iron, *Acta Metallurgica*, 28 (1980), pp. 33-39.
- [80] British Standard BS 7910, Guide to methods for assessing the acceptability of flaws in metallic structures, 1999.